

FRIEDRICH SCHILLER UNIVERSITY JENA

DOCTORAL THESIS

---

**Optimization of multicore optical  
fibers with fiber Bragg gratings  
towards bend and shape sensing**

---

*Author:*

Ravil IDRISOV

*Supervisor:*

Prof. Dr. Hartmut BARTELT

*A thesis submitted in fulfillment of the requirements  
for the degree of Doctor rerum naturalium*

Faculty of Physics and Astronomy



FRIEDRICH-SCHILLER-  
UNIVERSITÄT  
JENA

1. Gutachter: Professor Dr. Hartmut Bartelt,  
Leibniz Institut für Photonische Technologien,  
Albert-Einstein-Straße 9,  
07745 Jena, Deutschland

2. Gutachter: Professor Dr. Stefan Nolte,  
Institut für Angewandte Physik,  
Albert-Einstein-Straße 15,  
Jena 07745, Deutschland

3. Gutachter: Professor Dr. Salvador Sales  
ITEAM-Universitat Politècnica de València,  
Camino de Vera S/N,  
Edificio 8G Acceso D piso 5,  
46022 Valencia, Spanien

Tag der Disputation: 12.05.2022

# Contents

|          |   |           |
|----------|---|-----------|
| <b>1</b> | <b>Introduction</b>   | <b>3</b>  |
| <b>2</b> | <b>State of the art and used methods and equipment</b>                | <b>7</b>  |
| 2.1      | Curvature, bend and shape sensing . . . . .                           | 7         |
| 2.1.1    | Calculation for curvature and shape . . . . .                         | 10        |
| 2.1.2    | Torsion sensitivity and measurement . . . . .                         | 12        |
| 2.1.3    | Interrogation methods in distributed shape sensing . . . . .          | 13        |
| 2.1.4    | Current trends in shape sensing . . . . .                             | 15        |
| 2.2      | Fiber Bragg gratings . . . . .  | 16        |
| 2.2.1    | History of fiber Bragg gratings . . . . .                             | 18        |
| 2.2.2    | FBGs fabrication methods . . . . .                                    | 20        |
| 2.2.3    | Laser sources for FBG inscription . . . . .                           | 21        |
| 2.2.4    | Talbot interferometer . . . . .                                       | 23        |
| 2.3      | Multicore optical fiber . . . . .                                     | 25        |
| 2.3.1    | Multicore fibers fabrication . . . . .                                | 26        |
| 2.3.2    | Fanouts, splicing and channels management . . . . .                   | 28        |
| <b>3</b> | <b>Angular properties characterization of multicore fibers</b>        | <b>35</b> |
| 3.1      | Measurement concept . . . . .   | 35        |
| 3.1.1    | Optical scheme . . . . .  | 36        |
| 3.1.2    | Experimental setup . . . . .  | 37        |
| 3.1.3    | Cross-correlation . . . . .   | 38        |
| 3.1.4    | Alternative methods . . . . .   | 39        |
| 3.2      | Measurement for orientation and twist in various complex fibers . . . | 39        |
| 3.2.1    | Scattering patterns of the tested fibers . . . . .                    | 40        |
| 3.2.2    | Orientation measurement based on cross-correlation . . . . .          | 40        |
| 3.2.3    | Using simulated reference pattern stacks . . . . .                    | 43        |
| 3.2.4    | Optical fiber twist measurement . . . . .                             | 45        |
| 3.3      | Summary . . . . .   | 48        |
| <b>4</b> | <b>Optimizing FBG inscription in multicore fibers</b>                 | <b>49</b> |
| 4.1      | Ray tracing simulation of multicore fiber illumination . . . . .      | 51        |

|          |  |            |
|----------|--|------------|
| 4.2      | Experimental setup for FBG inscription . . . . .                                   | 54         |
| 4.3      | Results and discussion . . . . .   | 55         |
| 4.4      | Summary . . . . .  | 58         |
| <b>5</b> | <b>Multicore fibers calibration for curvature sensing</b>                          | <b>59</b>  |
| 5.1      | Shape sensor calibration in steps . . . . .  | 59         |
| 5.1.1    | Fiber geometry . . . . .   | 62         |
| 5.1.2    | Photo-elastic coefficient . . . . .  | 63         |
| 5.1.3    | Initial fiber Bragg gratings reflection peak wavelengths . . . . .                 | 64         |
| 5.1.4    | Intrinsic twist measurement . . . . .  | 65         |
| 5.2      | Evaluation of calibration corrections with a test object . . . . .                 | 68         |
| 5.3      | Summary . . . . .  | 70         |
| <b>6</b> | <b>Multiplexing of FBGs in multicore fibers using the inverse bend sensitivity</b> | <b>73</b>  |
| 6.1      | Concept of the inverse bend sensitivity . . . . .                                  | 74         |
| 6.1.1    | Comparison of the FBG inscription in a linear and curved fiber                     | 75         |
| 6.2      | Method for the multiplexed FBGs inscription . . . . .                              | 78         |
| 6.3      | Experimental proof of principle . . . . .  | 79         |
| 6.4      | Summary . . . . .  | 81         |
| <b>7</b> | <b>Space division multiplexing with FBGs in a multicore fiber</b>                  | <b>83</b>  |
| 7.1      | Multicore fiber component concept . . . . .  | 84         |
| 7.2      | Multicore fiber component fabrication procedure . . . . .                          | 86         |
| 7.3      | Proof of principle with two connected elements . . . . .                           | 88         |
| 7.4      | Summary . . . . .  | 90         |
| <b>8</b> | <b>Conclusions and outlook for future work</b>                                     | <b>93</b>  |
|          | <b>Bibliography</b>  | <b>95</b>  |
|          | <b>Zusammenfassung</b>   | <b>115</b> |
|          | <b>Curriculum vitae</b>  | <b>119</b> |
|          | <b>List of publications</b>  | <b>121</b> |
|          | <b>Ehrenwörtliche Erklärung</b>  | <b>123</b> |

# Chapter 1

## Introduction

Optical fiber sensors have been developing as a field for decades, sometimes hiding in the shadow of a big motion of the telecom companies. The infrastructure developed for the use of fiber optic cables, as well as instrumentation for fibers handling, were all used in the sensing field. Fiber sensors benefited from the fibers of high purity and cutting edge technology devices, such as splicers, reflectometers, wavelength division light sources becoming cheaper as technology grew. The very fiber cable network can even serve as a gigantic distributed sensor for seismic activity [1].

The research subject of this dissertation refers to the field of curvature and shape sensing, which is achieved by measuring strain conditions in individual cores of a multicore fiber. Strain measurement in multicore fibers can be performed using various techniques. The examples given in this dissertation mainly utilize fiber Bragg gratings (FBGs), as this is the most visual and straightforward shape sensing principle for demonstration. The scope for applications of this thesis is broader and can apply to other interrogation and sensing methods beyond FBGs and even beyond the application in shape measurement.

There is no recipe for making a perfect shape sensor covering every possible application in a single configuration. From measuring a tunnel or bridge deformation to blood vessels condition, each task will require a tailored solution. Hence, there is space for a family of shape sensors based on various multicore fibers and interrogation solutions. Multiple aspects define the applicability of each particular solution for a given task. These aspects must be studied to set boundaries defining where a particular shape sensor can be used. Few technologies are available for position resolved interrogation of optical fibers. These are based on time-of-flight measurement - optical time domain reflectometers (OTDR), optical spectrum analysis devices - spectrometers, tunable wavelength interrogators, and a combination of both, more sophisticated systems - optical frequency domain reflectometers (OFDR) and code division multiplexing systems (CDM). When used with multicore fibers, the sensing length of these systems is decreased compared to conventional strain sensors based on single-core optical fibers. An interrogation of multicore fibers is

analogous to the multiple fibers measurement with a position synchronization.

The topic of shape sensors in multicore fibers has been addressed for more than two decades now [2, 3]. The shape measurement based on multicore fiber exploiting Rayleigh backscattering and FBGs conjugated with optical frequency domain reflectometer being the most successful among others [4, 5]. In 2012, Jason Moore and Matthew Rogge published a comprehensive description of how to calculate the shape of an object using multicore fiber and parametric curve solutions [6]. In their paper, they give a detailed description of extracting strain data from an optical fiber and using it for shape reconstruction. The authors have performed simplifications of Frenet-Serret equations to use them for a limited amount of data achieved from fiber Bragg gratings in a multicore fiber. They also comprehensively covered the shape reconstruction process along with the measurement errors evaluation.

In Chapter 2, several aspects have to be considered for optical fiber-based shape sensing. Curvature measurement in multiple points and combination of these measurements (shape measurement per se), calculation and reconstruction of shape is one of them. The second aspect is using a fiber Bragg grating - optional for shape measurement but a widespread instrument in fiber sensors. The third aspect is the multicore fibers. They exist in various designs and are made of different materials using several technologies. Additionally, multiplexing in optical fibers is discussed from the perspective of shape sensors. The setups used for FBGs inscription in multicore fiber, including Master Oscillator Power Amplifier (MOPA) excimer laser and Talbot interferometer, are shown and explained. Fabrication methods of multicore fibers, including preform manufacturing methods and fiber drawing tower, are elaborated upon.

The research part in the following chapters is split into four parts, each covering a specific aspect of shape sensors based on FBGs in multicore fibers (Figure 1.1). Topics include characterization of multicore fiber from the perspective of angular orientation, FBG inscription in multicore fibers, optical waveguides characterization and calibration for curvature and shape sensing, and special multiplexing concepts utilizing multiple cores.

Chapter 3 is dedicated to the measurement of the angular orientation of anisotropic complex optical fibers such as multicore, photonic crystal, or ribbon fibers. Along with the orientation measurement, this chapter describes the issue of detecting twists occurring during the fiber drawing procedure. The measurement of these unwanted twists is used for further reconstructed shape correction, which otherwise suffers from errors in the curvature direction detection. Several complex fibers were studied in order to develop a procedure for orientation and twist measurement. So it is essential to have a method that will provide us with the respective

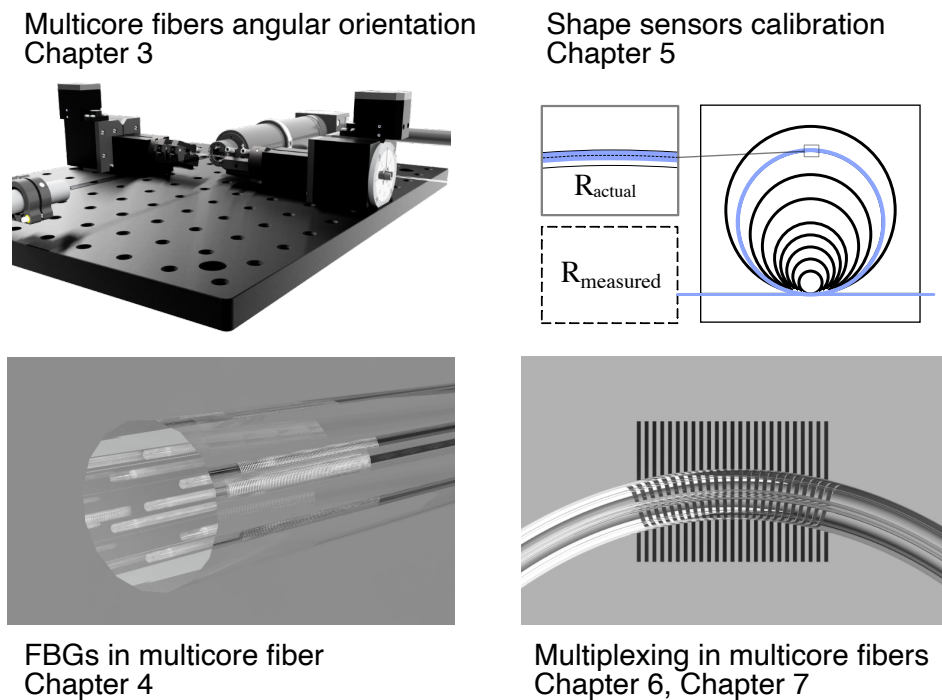


FIGURE 1.1: Main research topics of this dissertation.

location of the cores without cleaving the optical fiber, ideally fast enough to analyze as the fiber is drawn. Since the fibers are drawn from the preforms, they replicate the preform structure in a down-scaled size, and the angle measurement will reveal the complete fiber core arrangement at the measured location.

In Chapter 4, the FBG inscription efficiency is discussed for a multicore fiber. For the interrogation of an FBG array in a multicore fiber in the spectral domain, it is essential to have reflection peaks with similar amplitude and spectral width to avoid overlapping reflection peaks. In order to achieve such similar reflectivities, attention should be paid to the angular orientation of the fiber during FBG inscription. At a particular range of angles, even rare type II FBGs can be produced, which could cause an overlap with neighboring peaks and create defects in cores. Therefore, such critical orientations must be avoided for FBG inscription.

Another procedure that benefits from orientation measurement of optical fibers is the calibration for curvature sensing, as described in Chapter 5. Orientation measurement performed along the fiber length allows for detecting intrinsic twist and reducing false helical shape reconstruction errors. Besides the calibration for the twist, a protocol for accuracy enhancement is established. A step-by-step protocol allows to eliminate errors coming from geometrical and material non-uniformities, resulting in an uneven response of different cores and parts of the fiber to bending.

The last part of my research lies in the field of multiplexing. Within this dissertation, two new multiplexing methods based on multicore fibers are presented. These

methods have different purposes.

In Chapter 6, one method directed towards simplifying the optical equipment required for employing multicore fiber-based sensors is presented. The FBGs inscribed in a bent fiber will have different reflection peak shifts in a linear state, which will allow discriminating the reflection from gratings in different cores without a fan-out device. This, in turn, will allow using a simple curvature or even shape sensor with a single channel system. To utilize this principle with high efficiency, the direction of bending performed for FBG inscription is crucial. The fiber must be bent in a way that allows for achieving maximal distance between the cores projection onto a plane parallel to the bending plane. It can be done, e.g., using a fiber angular orientation system, as described in Chapter 3.

In Chapter 7, the multiplexing concept based on a patented design of a composed multicore fiber component is introduced. The concept addresses a problem of a limited shape sensor length based on arrays of FBGs. It is suggested to use cores with different photosensitivity to combine sensing and signal transmitting cores in a single cladding. The design allows for inscribing gratings during the fiber drawing process in one specific set of cores only, while another set will be used to deliver the signal from light source to FBGs and from FBGs to the interrogator undisturbed. Examples of a specific design and choice of materials are given in this chapter.

Finally, in Chapter 8, the achieved results and their impact are summarized, and an outlook for future work is given.



## Chapter 2

# State of the art and used methods and equipment

This chapter consists of three main parts related to state-of-the-art shape sensing using multicore fibers.

The first part is dedicated to the concept of curvature and bending measurement, explaining shape sensing from the perspective of the optical fiber structure and methods to measure curvature and shape. Shape sensing calculation from local strain measurements is given and discussed. Torsion as a possible event happening in extended fibers and its effect on the measurement accuracy is covered. Multiplexing systems that can potentially be used for shape sensing in multicore fibers are described.

Fiber Bragg gratings are enabling elements for many fiber sensors. They can also be well used in shape sensing applications. Fiber Bragg grating technology is described especially from the perspective of multicore optical fibers. Also, the methods for fiber Bragg gratings fabrication are given. The MOPA (Master Oscillator Power Amplifier) excimer laser system provides coherent radiation for high-reflectivity FBGs. The Talbot interferometer as a successful tool for inscribing gratings with different periods is also described.

Multicore fibers in different designs, their fabrication methods from preform to fiber drawing are discussed in the last part of the chapter. Multicore fibers require special instruments and devices for splicing, interrogation, fan-ins and fan-outs and these are therefore also described.

### 2.1 Curvature, bend and shape sensing

Optical fibers are well known as strain gauges - tools to measure and display relative elongation. Fibers even have the property to measure their own layout in space [7–10] (Figure 2.1). However, this property is not limited to optical fibers. Multiple technologies have been reported with the ability to measure the curvature, which is

the shape of a uniformly curved object, or to measure bending, which is a dynamic change of curvature. Among technologies providing information about shape are: electrical gauges [11, 12], optoelectronic devices [13, 14], machine vision [15, 16] and others [17–21].

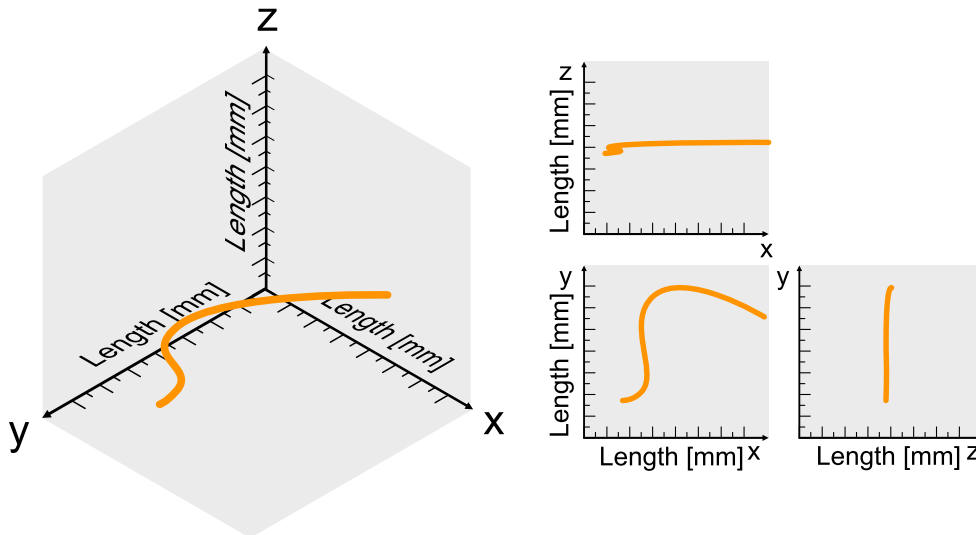


FIGURE 2.1: Layout of a multicore fiber in 3D space to be reconstructed from fiber bending.

Optical fibers are sensitive to shape because curvature or bending causes gradient of strain and refractive index modulation in the fiber's cross-section. However, due to the centralized location of the core in the bending gradient, the layout of a standard single-core fiber cannot be measured directly. The gradient of the strain and refractive index modulation changes along the bending direction and equals zero in the neutral axis - an axis perpendicular to the bending direction and crossing the center of the fiber (Figure 2.2a). The core can be shifted from the center to induce curvature sensitivity in a single-core fiber, as shown in Figure 2.2b. Such sensor is uni-directional since the core will experience strain and refractive index change with maximum sensitivity only in one direction. In the case when a fiber can be bent in different directions, a single-core measurement is insufficient since the change of bending direction will modulate the sensitivity and, thus, create ambiguity. An additional core would allow for extending the bending direction range. However, the curvature direction as shown in Figure 2.2c is still ambiguous. Both cores will have identical measurements, which can be confused with the stretching of fiber. Therefore, an omnidirectional curvature sensor requires at least three cores (Figure 2.2d). When ambiguity of torsion and stretching is of risk, an additional central core is desirable (Figure 2.2e).

Shape sensing is the reconstruction of a structure curvature distribution and its dynamic change using discrete strain measurements giving information about

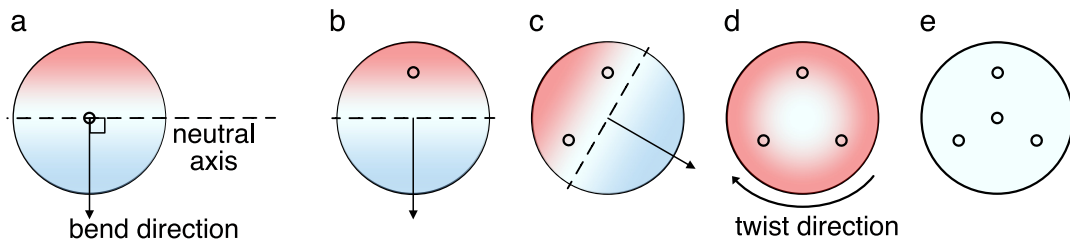


FIGURE 2.2: Different curvature and twist conditions for fibers with different designs. a) - Single-core fiber is insensitive to curvature as the core is located in the middle of the stress gradient created by bending resulting in zero strain on the neutral axis. b) Offset-core single-core fiber can be a uni-directional bending sensor with a fixed bending direction. c) - Two-core fiber can measure bending in a range of directions except for the shown direction. d) - Three-core fiber can be an omnidirectional bending sensor, but it cannot distinguish between strain and torsion. e) - Typical four-core fiber used for shape measurement being able to measure omnidirectional and to discriminate strain and torsion effects.

local stress conditions. Shape sensing in a multicore optical fiber is performed by combining multiple curvature measurements distributed over a length of the fiber.

The shape measurement can be performed using discrete measurements of strain from individual deformation sensors fixed on a test object. The accuracy of the measurement and ability to distinguish between various types of deformation will require multiple sensing points in the same plane and distributed sensing points along the test object length. This is why optical fibers, having different options for efficient multiplexing and evenly distributed sensing points, would be a good choice for shape measurement [7]. Multicore fibers, which share the multiplexing methods with conventional optical fiber sensors, can play an essential role in the shape sensing field by confining cross-sections in a unified cladding (Figure 2.3).

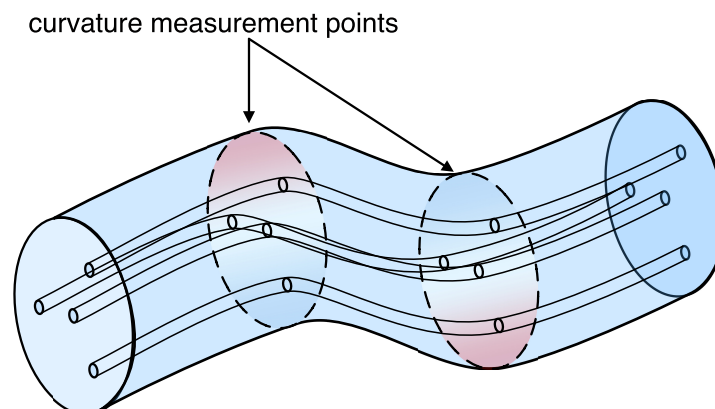


FIGURE 2.3: Distributed shape sensing using four-core fiber.

Compact and lightweight, multicore fibers can fit into small channels, can be glued to objects' surfaces without changing their mechanical response to stress. The operation of multicore fibers is similar to multiple fibers fixed together. Optical

splicers, cleavers, and fiber strippers can be shared with single-core fibers. The combination of cores sharing one cladding allows fabricating such fibers with the standard size as in the telecommunication fibers - (125 $\mu$ m). However, demultiplexing remains an issue. Fanout devices, which allow to split fiber channels with multiple cores and connect them to individual single-core fibers, often have to be custom made. A method to overcome this problem and to avoid a fanout device for FBG based sensors is addressed with a special approach for wavelength multiplexed gratings in Chapter 6.

### 2.1.1 Calculation for curvature and shape

Multicore fiber calculations are performed via discrete strain measurements in the cores located in a single fiber cladding. These cores have to be at a different distance from the neutral axis of bending to provide information about the curvature direction. That is why the most common designs of a multicore fiber for shape sensing consist of at least three cores forming a triangle.

To understand the shape calculation, it is necessary to see how the strain is measured. Strain in optical fibers is routinely calculated from frequency (in the case of measurement with an OFDR), or from wavelength shift (in the case of FBGs interrogation). For the case of FBGs, the reflection peak center shift  $\Delta\lambda$  is shown in the Equation 2.1 [22].

$$\Delta\lambda = \lambda_{\text{Bragg}}((1 - \rho_e)\epsilon + (\alpha_\lambda + \alpha_n)\Delta T) \quad (2.1)$$

Here,  $\lambda_{\text{Bragg}}$  represents the wavelength peak center measured at the starting condition, with no external force applied, and at the known, registered temperature. The photo-elastic or stress-elastic coefficient  $\rho_e$  characterizes the change of refractive index caused by stretching or compression. Measurement of this coefficient in multicore fiber is discussed in Chapter 5. Strain  $\epsilon$  is the elongation parameter measured in microstrains ( $\Delta L/L \times 10^{-6}$ ).

Coefficients  $\alpha_\lambda$  and  $\alpha_n$  represent thermal expansion and thermo-optical effects per temperature increment  $\Delta T$ .

In this work, the experiments are carried out in a temperature-controlled environment. Hence, the temperature is considered to be constant. The temperature cross-sensitivity of FBG based strain sensors is a well-known problem that applies not only to shape sensors. The subject is therefore often covered in the literature [23–25].

Now we consider a sensing fiber layer out in 3D space. A curve in 3D space can be described by a set of Frenet-Serret formulas independently derived by Jean

Frenet in 1847 and Joseph Serret in 1851 [26]. The formulas are given in the Equation 2.2, 2.3 and 2.2. In all three formulas, derivations are with respect to the position on the curve,  $s$ .

$$\frac{dT}{ds} = \kappa N \quad (2.2)$$

$T$  is the vector directed tangent to the curve,  $\kappa$  is a scalar value of curvature,  $N$  is the orthogonal vector to  $T$  directed toward the center of curvature.

$$\frac{dN}{ds} = -\kappa T + \tau B \quad (2.3)$$

The scalar value of torsion is represented by  $\tau$ .  $B$  is the binormal vector, orthogonal to both  $T$  and  $N$ .

$$\frac{dB}{ds} = -\tau N \quad (2.4)$$

In the paper published by Moore and Rogge [6], the authors elaborate the Frenet-Serret formulas for general strain expression at discrete points for a particular case of an optical fiber with any number of cores:

$$\epsilon_i = -\kappa r_i \cos(\theta_b - \frac{3\pi}{2} - \theta_i) \quad (2.5)$$

Here,  $\epsilon_i$  is the strain experienced at the  $i^{\text{th}}$  core,  $\kappa$  is curvature,  $\theta_b$  is the angle between an axis of a global coordinate system and the curvature direction, and  $\theta_i$  is an angle between the axis and the radius  $r_i$ , which is drawn from the center to the core number  $i$  (all parameters shown in Figure 2.4). For calculation convenience, the accepted axis can be aligned with one of the fiber cores.

Further elaboration gives us the calculated curvature:

$$\kappa_c = \frac{2 \times \sqrt{\left(\sum_{i=1}^N \frac{\epsilon_i}{r_i} \cos \theta_i\right)^2 + \left(\sum_{i=1}^N \frac{\epsilon_i}{r_i} \sin \theta_i\right)^2}}{N} \quad (2.6)$$

The final equation allows for calculating curvature and its direction from the measured strain. Torsion and general stretching are not considered in this formula. The calibration process allowing for a more accurate individual strain measurement, considering additional intrinsic twist for avoiding an inadequate helical shape instead of planar shape reconstruction, is discussed later in Chapter 5.

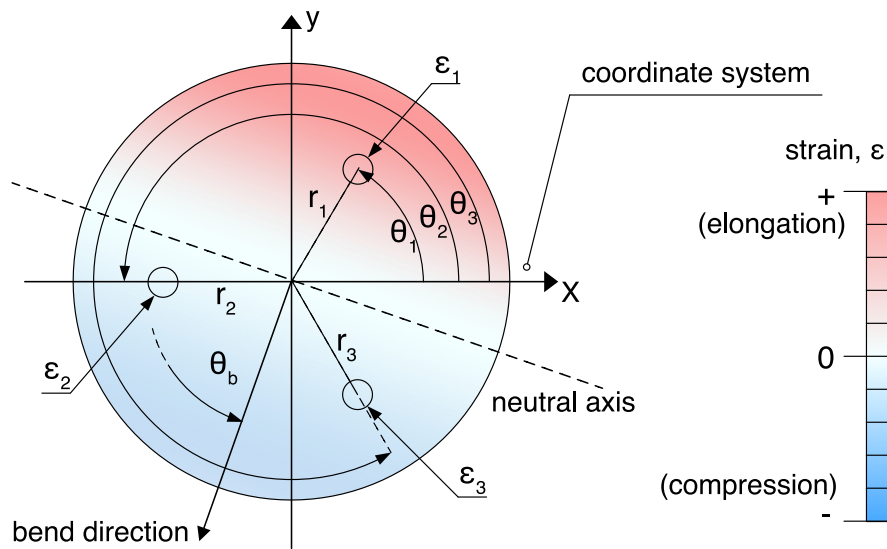


FIGURE 2.4: Cross-section of a multicore fiber at the measurement point.

### 2.1.2 Torsion sensitivity and measurement

A multicore fiber is naturally responsive to torsion, which makes it an attractive element of a torsion measurement device [27, 28]. In the context of a shape sensor, the torsion has to be also considered for an accurate measurement. The four-core fiber shown in Figure 2.2e, ordinarily used in shape sensors can measure the amount of torsion, but not the direction. From the mechanical point of view, torsion will cause stretching of the outer cores while the central core will not experience any strain. For clockwise and anti-clockwise torsion with the same strength it will cause identical measurement of strain in the fiber. To introduce a sensitivity to torsion direction, the multicore fiber can be twisted intentionally during the fiber drawing process. Here, the fiber preform is rotated in a holding mechanism at a constant speed while being drawn. This allows achieving a wide range of twist periods, with most of the papers reporting about 50 rotations per meter and more [29, 30]. However, the twisted multicore fiber also has some considerable limitations. Such small rotation periods, comparable to a typical FBG length, are used to increase the torsion sensitivity range. The range in which the fiber can still discriminate the torsion direction is limited by the intrinsic twist. When a fiber is twisted counter to the imprinted twist, the outer cores experience compression, while the central core remains undisturbed. This happens up to a state when the outer cores become straight. If the torsion is greater than the intrinsic twist, the cores stretch again after crossing the state of straightened cores.

The possible twist period is limited by spatial resolution or, in the case of FBG

based sensors, the length of an individual grating. When the minimal spatial resolution or a grating length size is comparable to the fiber twist period and the fiber has a large curvature (curvature radius  $>$  twist period), the single measurement point or a grating will be located on both sides from the neutral bending axis.

As shown in Figure 2.5a, points A and B are located in a blue twisted outer core with an inscribed FBG. The grating length is greater than a half of a twist period. When fiber is curved as shown in Figure 2.5b, the points A and B are located on different sides of the neutral axis. Both stretching and compression effects will be detected by the FBG in the blue core simultaneously. This affects the shape of the FBG reflection peak and might induce a peak detection algorithm failure (Figure 2.5c).

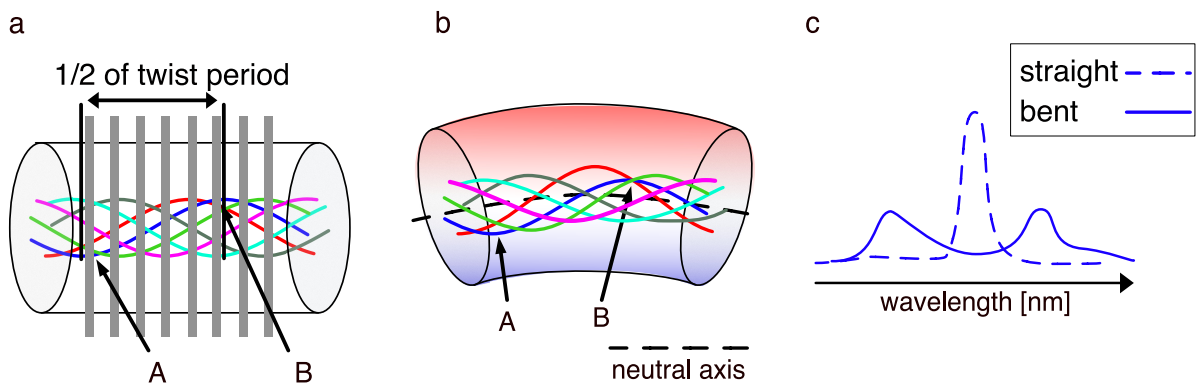


FIGURE 2.5: FBG inscription and curvature measurement in a twisted multicore fiber a) - An FBG inscribed in the blue core of a twisted fiber. The length of the grating is greater than a half of a twist period. b) - Bent multicore fiber. The points A and B are now located on different sides of the neutral axis. c) - The shape of the FBG reflection peak changes with bending.

### 2.1.3 Interrogation methods in distributed shape sensing

Shape is a fundamental parameter for the structural health management of critical components [31–36]. Shape sensing is also an essential part of robotics [37–39] and ambitious application for medical catheters [40–42] and aircrafts wing behavior study [43, 44]. Despite being involved in many fields, the demands and expectations from the shape detection devices are very different. There are explosive environments that cannot exploit electric-based gauges. Also, the spatial resolution needed for a surgical needle or a catheter will not work for a bridge. Nevertheless, an optical fiber-based sensing system can apply to both, even with an identical fiber.

What enables the applicability of a similar optical fiber for such different tasks? Several methods have become mature in the sensing field that change fiber capabilities depending on the interrogation technology. A quick overview of the standard

fiber measurement technologies will help understand the advantages and weaknesses and why choosing an appropriate interrogation system for a specific task is crucial.

### **Time resolved systems**

In this category, the first and most common method is optical time-domain reflectometry (OTDR)[45–49]. This kind of device launches a series of short pulses into the fiber and measures backscattering: Rayleigh, Raman, or Brillouin. A significant advantage of these systems is the long-distance measurement. Standard fibers are applicable and no specific fiber preparation is required. On the downside, poor spatial resolution, ‘blind zones’, and low SNR limit the use of OTDR for shorter fibers and for accuracy demanding tasks. The spatial resolution can be enhanced by the use of phase-sensitive OTDR ( $\phi$ -OTDR) via the use of coherent illumination source [50, 51] but the primary use of such reflectometers is in very long system networks (several hundred meters and more). To my best knowledge, multichannel OTDR systems are not yet commercialized. Low spatial resolution, frequency, and extended sensing distance would be more applicable to large curvatures. The available demonstration of the use of multicore fibers for large curvature measurements is limited. Shape sensing has been shown using BOTDA - Brillouin optical time-domain analysis [52], and BOTDR - Brillouin scattering OTDR in the form of sequential interrogation of multiple cores for a static shape with the latter having a significant advantage due to single end connection versus a pass-through scheme [53, 54].

### **Spectral domain interrogators, WDM devices**

Wavelength division multiplexing in optical fiber sensors is often associated with fiber Bragg gratings. Strain sensors based on FBGs are very mature and used for a few decades. They have become popular thanks to the simple, affordable interrogators, which can simultaneously measure 40-60 strain gauges depending on the spectral distance of bandwidth of the illumination source. There are typically two configurations used in the FBG interrogators. The first configuration relies on a tunable laser source synchronized with a photodetector plotting the signal change in time as a change of wavelength [55–59].

The second type of WDM interrogator relies on a spectrometer. The light reflected from a grating or an array of gratings is collimated and directed to a spectral grating and is read out by a linear pixels array (CCD line) or a camera. Wavelengths are spatially resolved, and peak centers are determined by the center of the gravity



of the signal. This type of interrogator is relatively cheap and can be very compact [60–62].

### **Frequency domain systems**

Frequency domain systems are represented by the Optical Frequency Domain Reflectometers (OFDR). This interrogator uses a fast photodiode and, similarly to phase-sensitive OTDR, takes advantage of a coherent illumination via a tunable laser source. In addition to the coherent time-coded signal, OFDR applies a Fourier transform algorithm to achieve frequency characteristics of the data. This advanced technique became popular thanks to high spatial resolution and the high number of sensing points possible to interrogate [63–66]. The presence of commercial multi-channel OFDR systems, along with high accuracy of measurement and good spatial resolution, made these interrogators popular for shape sensing with multicore fibers [5, 67–70]. OFDR can be used with regular fibers to analyze a Rayleigh backscattering signal and with arrays of FBGs, including quasi-continuous gratings. OFDR systems are very versatile and combine advantages of other popular interrogators. The major limitation for the general use of OFDR is the high price, especially for multichannel options, which can be explained by the complexity of the devices. The developers of OFDR systems promise chip integrated devices to increase accessibility in the future [71].

### **Code division multiplexing**

One of the most recent advancements in the field of fiber Bragg gratings is the interrogation method, which allows overcoming ambiguity when interrogating FBGs with identical spectra in the same channel. This new method employs code-division multiplexing [72–74]. This method substantially broadens the available length of FBG based sensing networks. Up to 4000 FBGs interrogated by a single device have been shown in publications [75, 76].

#### **2.1.4 Current trends in shape sensing**

Current trends in shape sensing using optical fibers includes temperature compensation, actual for the conventional strain sensors in optical fibers [77–79], adding force measurement and overall multifunctionality [37, 41, 80], expanding the range of measurements towards larger radii [81]. Another trending research direction is that of medical appliances, such as endoscopes and surgical catheters. Multiple studies are carried for flexible medical instrumentation [42, 82].

## 2.2 Fiber Bragg gratings

A fiber Bragg grating as a main element in many optical curvature and shape sensors is a periodical change of the refractive index in the core of an optical fiber (shown in Figure 2.6). A single fiber Bragg grating can be considered as a wavelength selective dielectric reflector. Bragg gratings are inscribed to induce narrow band back reflections in the fiber core.

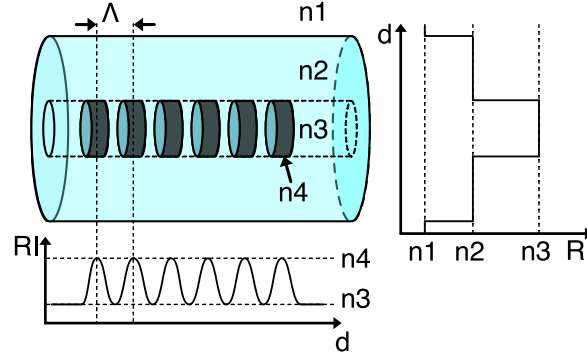


FIGURE 2.6: Schematic of a piece of an optical fiber with an FBG in the core. The FBG is forming multiple interfaces with typically a sine-like refractive index modulation.

Periodical refractive index changes in a fiber Bragg grating result in essentially multiple reflecting interfaces taking advantage of thousands of weak Fresnel reflections, creating a phase-matching condition with a counter-propagating mode (Equation (2.7)). Thus energy transfer is possible in agreement with the coupled-mode theory [83–85].

$$\beta_1 - \beta_2 = \frac{2\pi N}{\Lambda} \quad (2.7)$$

Here  $\beta_1$  and  $\beta_2$  are propagation constants of two modes interacting with a grating with a period  $\Lambda$ .  $N$  is an integer number corresponding to an order. The propagation constant  $\beta$  of a mode can be found through the effective refractive index  $n_{eff}$ , and the propagating light wavelength in vacuum,  $\lambda$ :

$$\beta = \frac{2\pi n_{eff}}{\lambda} \quad (2.8)$$

The main parameters characterizing an FBG are the reflection peak central wavelength  $\lambda_B$ , the reflectivity  $R$ , and the full spectral bandwidth  $\Delta\lambda_B$ . The Bragg reflection wavelength is:

$$\lambda_{Bragg} = 2n_{eff}\Lambda \quad (2.9)$$

Here,  $\lambda_B$  indicates the center of reflection peak for the fundamental mode with an effective refractive index of  $n_{\text{eff}}$ . If the fiber has more than one mode, it will result in multiple reflection peaks.

The following parameters apply to uniform FBGs - gratings with constant period and refractive index modulation amplitude. The strength of the grating or reflectivity,  $R$ , depends on the coupling constant  $\kappa_B$  and the grating length  $L$ :

$$R = \tanh^2(\kappa_B L) \quad (2.10)$$

The coupling constant  $\kappa_B$  can be found when the refractive index modulation amplitude  $\Delta n_{\text{mod}}$  and the mode power ratio  $\eta$  are known:

$$\kappa_B = \frac{\pi \Delta n_{\text{mod}} \eta}{\lambda_B} \quad (2.11)$$

The grating bandwidth, i.e., the spectral distance between minima of the strongest peak, can be calculated as in:

$$\Delta \lambda_B = 2\lambda_B \frac{\Lambda}{L} \sqrt{1 + \left[ \frac{\kappa_B L}{\pi} \right]^2} \quad (2.12)$$

For a weaker grating ( $\kappa_B L \ll \pi$ ) the reflection bandwidth merely depends on the number of fringes or periods  $\Lambda/L$ , whilst with  $\kappa_B L > \pi$  the coupling coefficient becomes dominant.

There are several different types of fiber Bragg gratings which are defined by the period and uniformity of refractive index modulation (main types are shown in Figure 2.7).

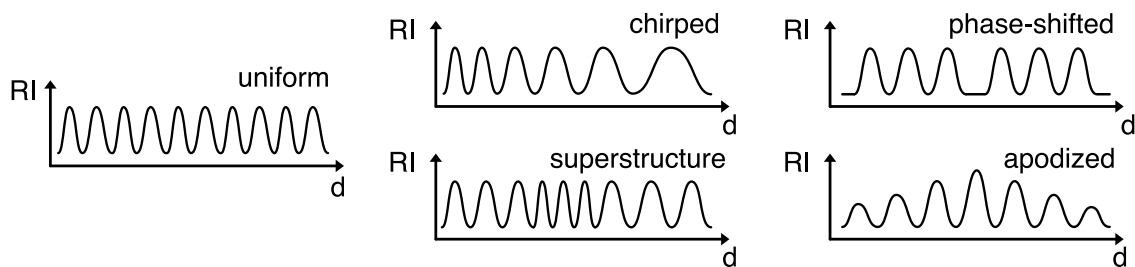


FIGURE 2.7: Refractive index modulation in different types of FBGs.

Chirped gratings are used to achieve a broader reflection spectrum. Broadening of the spectrum is achieved by variation of the period over the grating length. This can be beneficial for in-fiber filters, laser resonators, sensors, and others [86–89]. Another common application of chirped Bragg gratings is the chromatic dispersion compensation in the optical networks employing wide spectrum DWDM [90–92].

Phase shifted gratings are originally a pair of identical FBGs with a distance between two gratings corresponding to a phase shift of  $\pi/2$ . This kind of grating has a narrow notch in the reflection spectrum. Phase-shifted gratings are used for enhancing sensitivity of conventional FBGs [93–95].

Superstructured gratings are FBGs with a complex periodic change. They can be seen as a set of consecutive gratings with varying periodicity and length. The main applications of superstructured FBGs are the simultaneous measurement of temperature and strength and for achieving modes coupling [96–99].

Apodized gratings are specifically made for peak side lobes suppression [100–102]. This is achieved via a gradual increase of refractive index modulation from the edges to the center.

### 2.2.1 History of fiber Bragg gratings

The photosensitivity of doped silica fibers was first discovered and described in 1978 by Hill et al. [103]. The authors studied absorption in a few-mode fiber with a length of 62 cm through injecting an argon-ion laser beam in the core (Figure 2.8). As a result of the experiment, a reflection, now counter-propagating to incoming light was detected after a few minutes of exposure. This was explained as a periodic perturbation of the refractive index formed by a standing wave created by an interference of incoming light and Fresnel reflection from the second fiber end facet. The overall reflection from the created structure was narrowband and was detected at the wavelength of the laser source without affecting the transmission of the other parts of the spectrum. This proved that the new structure was periodic and did not increase the absorption properties of the fiber. The authors also reported the relation of the spectrum and strain and/or temperature.

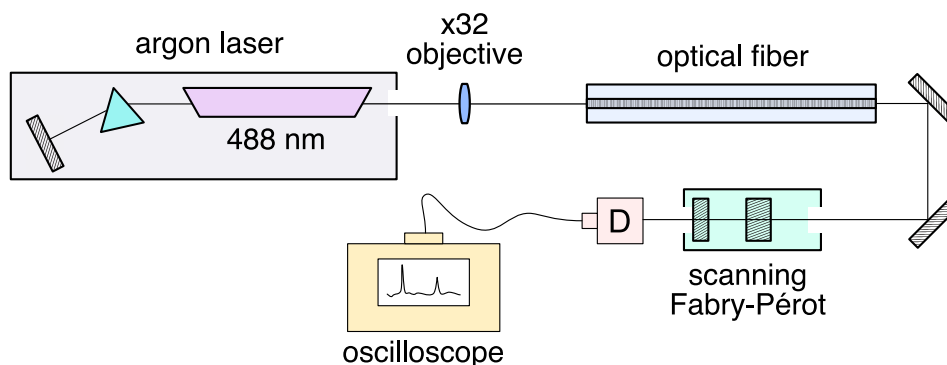


FIGURE 2.8: Standing wave inscription scheme

Later, in 1981, Lam and Garside replicated this experiment and studied a few dependencies in the gratings [104]. They built a theoretical model for the grating

formation and proved that the process responsible for the formation of the grating is a two-photon process, as was shown for the photorefractive effect in some crystals and in 1978 also with an argon-ion laser [105]. They studied the dependence of the induced refractive index change on the optical power of the illumination source and concluded that it is proportional to the square of optical power. Hence, double-photon absorption takes place in the experiment. This discovery made by Meltz, Morey and Glenn in 1989 showed that the photorefraction mechanism is related to the energy level of the germania oxygen-vacancy defect band [106].

The authors used a tunable dye laser combined with a frequency doubling crystal to achieve a source with a spectral band around 244 nm and appropriate coherence. This allowed for comparing the energy flux of lasers initially used for the grating inscription exploiting double-photon absorption with the laser emitting at the UV region and showing that single-photon absorption was nearly a million times more efficient. The first side-illumination inscription was successfully used and described in this paper (Figure 2.9). This was also the first interferometric scheme used for the grating fabrication. This method did not require accessing a facet of fiber and broadened capabilities of a single inscription setup since the interferometer could be tuned in order to achieve gratings in all transparent windows of silica optical fibers. The experiment proved that the silica cladding of the optical fibers was transparent enough to allow the laser light to reach the germanium-doped core.

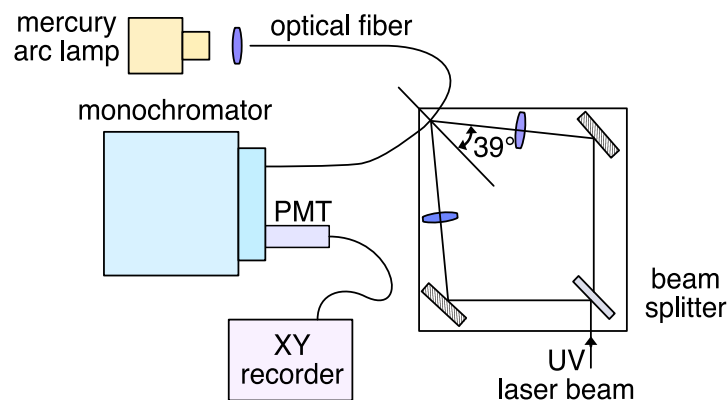


FIGURE 2.9: Side illumination FBG inscription scheme

The applications for new in-fiber structures as well as fabrication methods started to develop rapidly, e.g., in sensing and, as suggested in the first paper, as external reflectors for bulk lasers, FBGs found their way to fiber lasers, allowing a reduced size and increased handling comfort of these devices. One of the most critical milestones in the FBG history happened in 1993 and was associated with the first use of a phase mask for beam splitting [107].

### 2.2.2 FBGs fabrication methods

A phase mask is a grating, or a periodic structure on a transparent substrate. It effectively splits an incoming light into few diffraction orders. The grooves shape can be designed and manufactured so that most of the incoming energy is transferred to specific orders (e.g., +1 and -1). A phase mask as a beam splitter has many advantages. One is the direct inscription, allowing to place a stripped photosensitive fiber onto phase mask or very close to it and to achieve an interference pattern with good contrast even with laser sources with limited coherence (Figure 2.10). Another crucial advantage is in handling and adjustment convenience. A phase mask is often optimized for normal incidence. It creates a symmetric split and can be accurately placed. Such a symmetric setup allows precise overlap of the beams in the fiber core and represents an identical arms length in the interferometer.

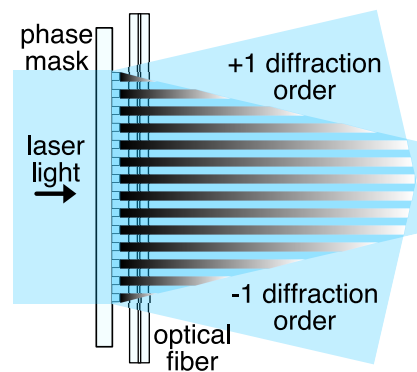


FIGURE 2.10: FBG inscription using phase mask (phase mask method)

The most common methods for Fiber Bragg gratings fabrication are phase mask or interferometric methods. Furthermore, when looking at the majority of the interferometric inscription schemes, it is usually the phase mask operating as a beam splitter due to simple adjustment and even energy distribution between the orders. Despite the domination of these two methods, alternative techniques have appeared in literature and have been reported throughout the last 30 years. Here I will discuss the primary methods for standard Bragg gratings inscription. Other types of fiber gratings, such as tilted, long-period, etc., can be fabricated using similar or identical techniques. The most common method for FBG inscription is a phase mask method shown in Figure 2.10. The method's main advantage is reliability, low requirements for the laser source, and minimum elements required. The period of the grating in the fiber is fixed to the half of the period mask according to the diffraction condition when the fiber is installed perpendicular to the pitches of a mask.

The principle relies on creating an interference pattern behind the mask from the overlapping diffraction orders of neighboring lines or grooves. For the best achievable performance, the fiber must be placed directly on the mask surface. This

position provides the highest contrast of the interference pattern. Although the interference pattern created by a single mask is fixed, it can be manipulated in a small range [108–110]. The optical fiber can be tilted or stretched, as shown in Figure 2.11 a, b. These tricks can shift the fiber’s grating reflection spectral peak towards longer (tilt) or shorter (stretching) wavelengths.

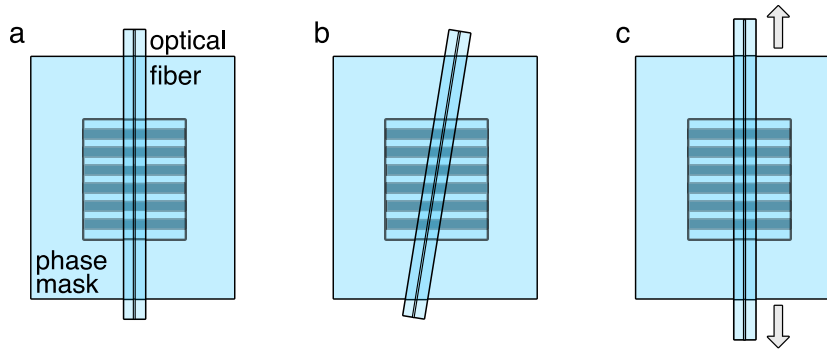


FIGURE 2.11: FBG inscription using phase mask. a) - Typical standard FBG inscription. b) - FBG reflection peak wavelength tuning using tilt of the fiber in regard to the phase mask. c) - FBG reflection peak wavelength tuning using fiber deformation.

When a fiber is placed at a distance from the phase mask, the interaction happens between different parts of the beam, leading to increased requirements for the laser source spatial coherence.

### 2.2.3 Laser sources for FBG inscription

For laser sources used with the phase mask and in some other methods, the most prominent ones are KrF and ArF excimer lasers and Ti:sapphire femtosecond lasers. These lasers exploit different mechanisms to modify the structure of glass. Excimer lasers, with their radiation wavelength of 193 nm (ArF) and 248 nm (KrF), are emitting at the absorption band of germania fibers. Therefore, the efficiency of the gratings inscription is highly dependent on the germanium doping of a fiber core. The principle of fs laser inscription is different and does not require a specific dopant [111]. The intensities achieved in the focus of a 100 fs long laser pulse induce non-linear absorption in the fiber and elevate the refractive index in a small region with the highest intensity [112, 113]. Both excimer and fs pulsed lasers are widely used nowadays and gradually replace CW Ar<sup>+</sup> used previously and reported in the first publications about FBGs. Both types of lasers are used in the commercial “Plug and Play” devices which allow inscribing gratings outside of a laboratory environment [114, 115]. Both excimer and fs lasers can be used in interferometric FBG inscription setups. The interferometric method is more sensitive to the source parameters. The main challenge for excimer lasers is the fiber placement and alignment within the

coherent region. Excimer lasers are known for poor temporal and spatial coherence, limiting their use in larger interferometric setups. To enhance the temporal and spatial coherence, excimer laser manufacturers suggest using MOPA systems (Master Oscillator - Power Amplifier).

AMOPA excimer laser system was used for all grating inscription experiments described in this thesis and therefore described here in details.

A MOPA excimer laser system consists of two laser modules with a connected axis and synchronized pulse generation (Figure 2.12). Laser modules can be identical or different depending on the required output pulse energy. Each module has a gas chamber filled with buffer, inert, and halogen gas. In the case of KrF laser, F acts as a halogen gas, Kr as an inert gas, Ne is usually used as a buffer (The same system can also be used with He with some adjustments in gas proportions and pressure). The gases' proportions are as follows: 65 mbar of 5% F, 95% He mixture, about 90-100 mbar of Kr, and 3500 mbar of Ne. Excimer stands for 'excited dimer', a common but misleading name applied to ArF and KrF lasers for the type of molecules created only from excited atoms. The more appropriate name for the ArF and KrF lasers would be 'exiplex' (excited complex) laser. Excitation of the Kr and F molecules is achieved with a short electric discharge of high power. A typical operational voltage of such commercial excimer lasers is in the kV region and 22-26 kV for the used laser. The rapid transfer of the high voltage to the electrodes is performed by another critical component of the laser - the thyatron. A thyatron is a gas-filled device (hydrogen in our case) operating a switch via exploiting Townsend discharge. The electrodes with a specific shape create a region inside the gas chamber with extremely high charge density, forcing exciplex molecules to create. These molecules are unstable and have a short lifetime (in the ns range), and fall apart, producing spontaneous emission in the process. The distance between electrodes, as well as their shape, will limit the beam size.

The Master Oscillator (MO) provides a narrow spectrum illumination of about 1-1,5 pm via spectral filtering. On one side of the MO, there is a module responsible for spectral filtering. It consists of a spatial filter (diaphragm), a prism telescope, and a reflection grating. The prism telescope expands the beam on the way to the grating to efficiently use the diffracting surface and reduce the energy density on the grating. The diffracted beam is collimated on a prism telescope. Only its' peak, the central part with a narrow spectrum, can pass through the diaphragm. Then the beam is amplified in the gas chamber and goes through a partially reflective mirror to the MO output. Here it enters a transportation module. In the given laser, enhanced spatial coherence is achieved via beam expansion in a magnifying telescope. Then the expanded beam with the narrowed spectrum and increased



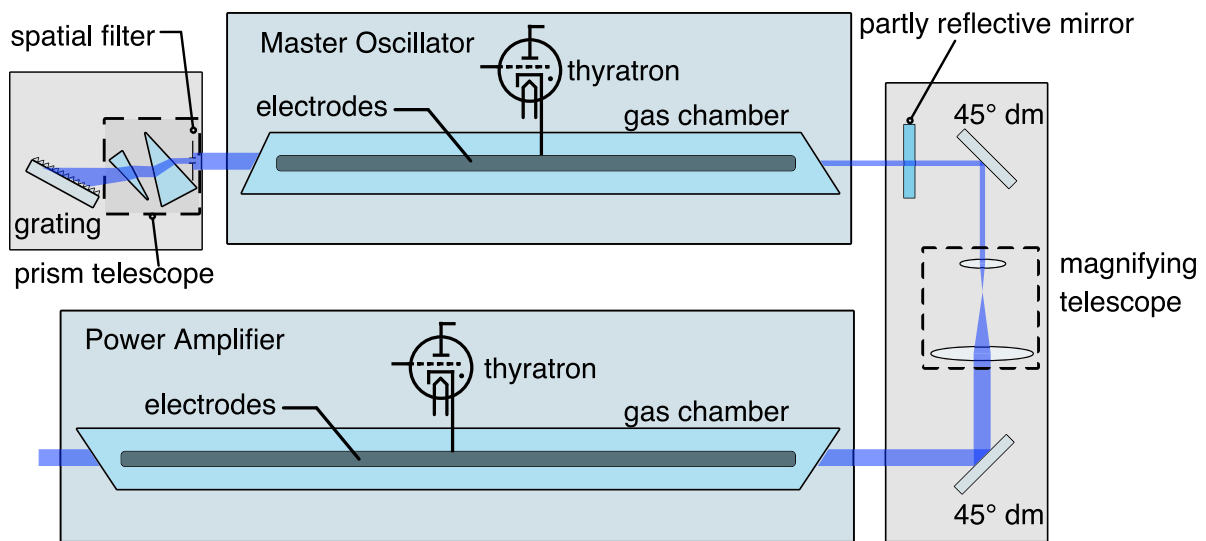


FIGURE 2.12: MOPA excimer laser principle scheme. 45° dm - dielectric mirror.

spatial coherence enters the Power Amplifier (PA). In the used setup, the PA does not have a resonator and provides a single-pass amplification. Alternatively, there might be a set of partly reflective mirrors installed. In this case, the output energy is expected to increase by using the population inversion with greater efficiency. There is also a possibility of replacing a telescope with an unstable resonator in the PA, which will also increase spatial coherence [116]. It is important to note that both laser modules are synchronized in time. The PA starts when the beam from MO enters the gas chamber with a slight delay added to ensure that the first part of the pulse consisting of spontaneous emission has left the PA.

The beam size of this laser is 8x10 mm, with output energy of about 200 mJ in a single pulse. The repetition rate can vary from 3 to 50 Hz. This allows inscribing gratings on the optical table with an interferometer. When installed on a fiber drawing tower, such operation frequency allows inscribing gratings with different spacing, including forming quasi-continuous gratings or all-grating fibers with identical or changing periods [117].

## 2.2.4 Talbot interferometer

Complex laser systems with high coherence have the advantage of being used in interferometric inscription setups. Interferometers are very responsive devices, and the schemes with symmetric designs are advantageous for simple alignment. One of the most used symmetric schemes is the Talbot or Phase mask interferometer (Figure 2.13). This interferometric scheme was used for all grating inscription experiments described in this thesis.

Along with the convenient alignment, Talbot interferometer allows for combining the diffracted beams in an identical way as in the region behind the phase mask, as shown in Figure 2.13, the edge A' of +1 diffraction order is combined with side A'' of -1 diffraction order, both emitted from edge A on phase mask. The focus of a cylindrical lens is located near the fiber and is distant from the phase mask, which reduces energy density passing through the mask. To inscribe a grating, reflecting a peak with a desired wavelength  $\lambda_{\text{Bragg}}$ , the knowledge about period  $\Lambda$  and effective refractive of a fundamental mode  $n_{\text{eff}}$  is required (Equation 2.9). The effective refractive index  $n_{\text{eff}}$  can be taken from the fiber datasheet for the fiber, or measured using different techniques [118, 119], including FBG inscription with a known period. This can be achieved by inscribing a weak grating (about 1%) in the fiber using a phase mask method as shown in Figure 2.11a. The period of the obtained FBG will be equal to a half of the phase mask period. Effective refractive index  $n_{\text{eff}}$  can be then calculated from the Bragg condition (Equation 2.9).

The in-fiber grating period  $\Lambda$  in case of interferometric method depends on the laser source wavelength  $\lambda_{\text{laser}}$  and the half-angle  $\theta$  (see Figure 2.13) between the combined beams:

$$\Lambda = \lambda_{\text{laser}} / (2 \sin \theta * n) \quad (2.13)$$

The angle  $\theta$  depends on the half of diffraction angle  $\alpha$  and the tilt of the mirrors  $\beta$ . It is important to note that a change of a tilt of, e.g.,  $1^\circ$  will change  $\theta$  by  $2^\circ$ :

$$\theta = \alpha + 2 * (90 - \beta) \quad (2.14)$$

The angle  $\alpha$  is calculated from the diffraction condition shown in Equation 2.15 for the diffraction order  $k = (+/-)1$  in this case.

$$\alpha = \arcsin(\lambda_{\text{laser}} * k / d) \quad (2.15)$$

The period change of the interference pattern is performed via tilt of the dielectric mirrors with the rotation axis crossing the Pivot point as shown in Figure 2.13.

The Talbot interferometer allows for inscribing gratings in a wide range without re-calibration for the accurate fiber position when aligned and centered well. This is especially an essential requirement for inscribing arrays of gratings during the fiber drawing procedure since calibration is done for a short range of reflection wavelengths  $\lambda_{\text{Bragg}}$  and a re-calibration for a different wavelengths is not possible in ongoing process.

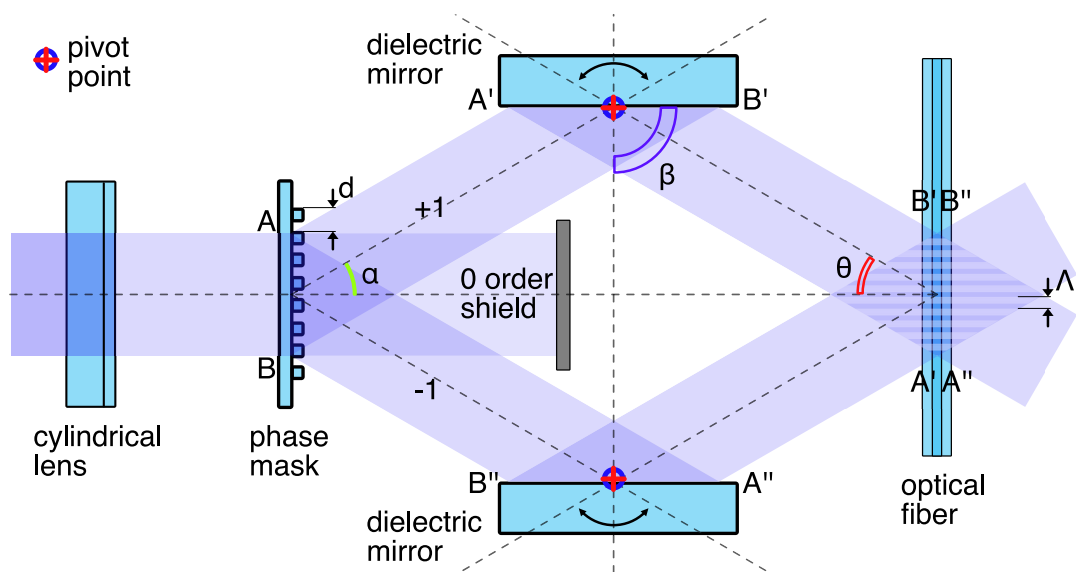


FIGURE 2.13: Talbot interferometer symmetry demonstration: the side A of the diffraction order +1 is overlapped with the side A of the diffraction order -1 in the fiber region.

## 2.3 Multicore optical fiber

As the main transmission element of modern telecommunication systems, the optical fiber is a waveguide for a confined electromagnetic radiation transmission, typically in the near-infrared region (NIR). Despite the vast majority of optical fibers operating in NIR, reported applications of optical waveguides cover the entire optical radiation region. After developing single-core waveguides, there have been early attempts to parallelize light-guiding cores, especially for imaging purpose. Starting from fiber bundles for flexible endoscopes, multicore optical waveguides have been developed. A multicore optical fiber is a fiber containing more than one light waveguiding core. Multicore fibers tackle the possibility of multiplying the signal capacity of a single fiber via a space-division multiplexing solution. This allows to pack more transmission channels in the same dimensions and manufacture information communication cables with larger transmission capability. Increased capacity at lower material and price cost was one of the main achievements of the optical fiber era, and multicore fiber enables the evolution of this feature. Along with the advantages of exploiting multicore fiber, there are several challenges to take when changing to multiple core fibers. This includes more sophisticated instrumentation for coupling and splicing (generally more expensive), new multiplexing elements, and stricter fiber design requirements. This creates an obstacle on the way to accepting multicore fiber-based cables as a standard for telecommunication networks. When talking about the general challenges of using multicore fibers, two main subjects are coming out. First is the intermodal coupling between the modes of different single-mode

cores. The second is the multiplexing/demultiplexing methods and devices. A major delaying factor for the use of such multicore fibers is the need for the physical discrimination of the signals coming from different fiber cores.

### 2.3.1 Multicore fibers fabrication

Multicore fibers are considered to be a relatively recent technology, but a patent from 1979 was already claiming that there are numerous techniques available, including a rod-in-tube which from description seems to be similar to the actually used nowadays stack-and-draw method [120]. The roots of multicore fibers go back to 1974 when a fiber drawn from a compound preform was demonstrated [121].

Today there are two main technologies used for multicore preforms: the stack-and-draw method and the drilling and insertion method, with majority of multicore fibers reported using the first one [122–139].

The drilling method is well known from the PANDA fibers manufacturing process, where the preform is drilled to insert two stress-inducing rods and then drawn normally [140, 141]. In multicore fibers, the holes are drilled in a silica rod for several cores (Figure 2.14). The cores are usually made using standard preform manufacturing technologies, i.e., Modified Chemical Vapor Deposition (MCVD).

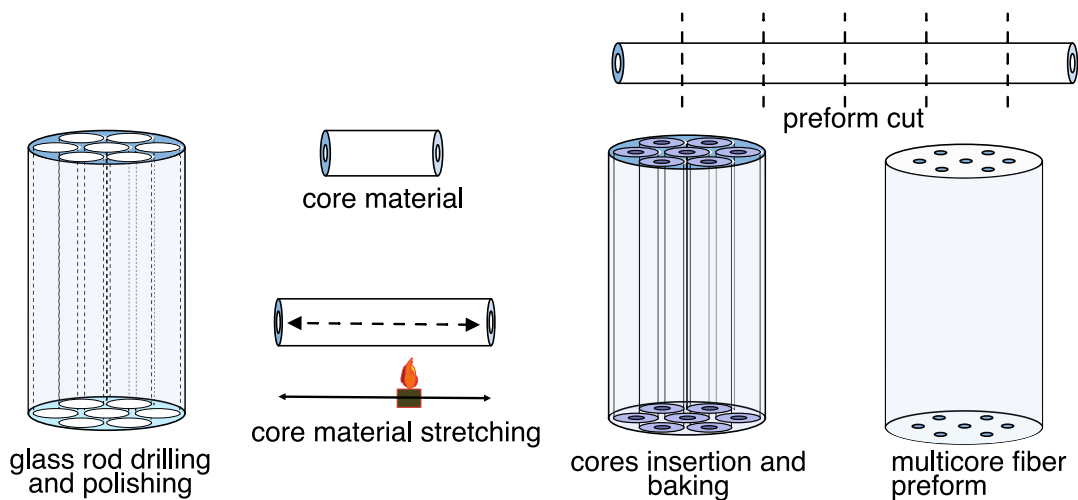


FIGURE 2.14: Drilling and insertion multicore fiber preform preparation method.

Then processing (polishing) of drilled channels has to be performed [29]. This is required to avoid defects in fibers that can develop from rough surfaces or microscopic scratches and glass particles. After the canes consisting of a down-scaled single-core preform are inserted into the channels, the fiber is drawn normally. Applying this method to multicore fibers is time-consuming and puts limitations on the preform length, depending on the drilling setup [142]. The only advantage that

can be counted for the drilling technique is the lack of need for a core to cladding ratio adjustment, which is frequently required in the stack-and-draw procedure.

Multicore fiber production using stack-and-draw technology is shown in Figure 2.15.

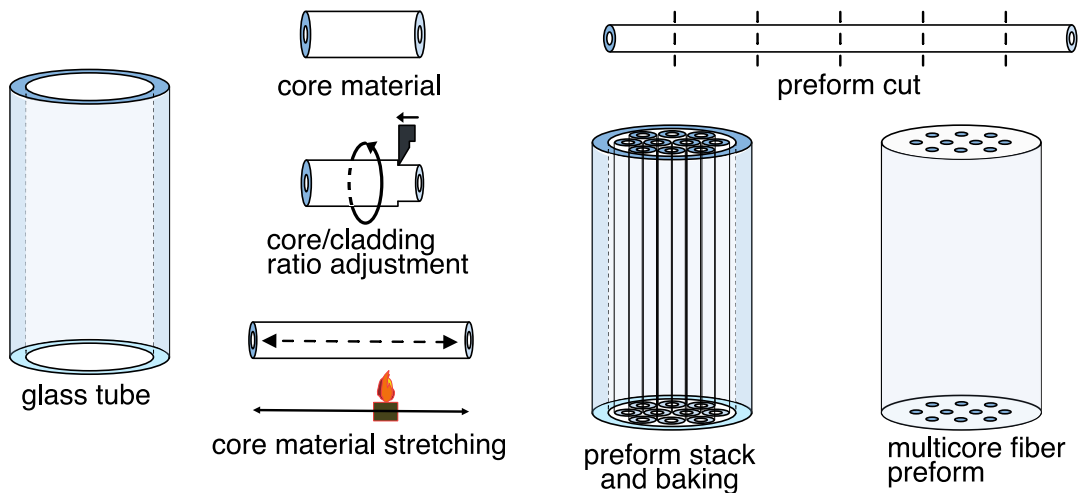


FIGURE 2.15: Stack-and-draw multicore fiber preform preparation method.

The core material is made from a regular preform manufactured using, i.e., the MCVD process. This core material is polished or etched from the outside to increase the core/cladding ratio. Typically, a hexagonal structure made of many rods is composed. Then this structure is inserted into a silica tube, and the tube is sealed or melted along with the inner elements. Multicore preform prepared this way can be drawn normally. A few examples of multicore fiber cross-sections drawn from fibers using the stack-and-draw technique are shown in Figure 2.16.

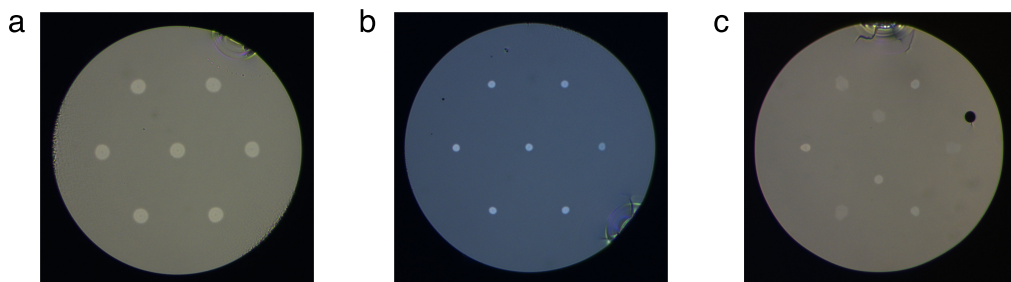


FIGURE 2.16: Multicore fiber examples drawn from a preform made using stack-and-draw technique. a) - Seven-core fiber optimized for splicing with SMF-28. b) - Photo-sensitive seven-core fiber optimized for FBG inscription. c) - Multicore fiber with eight cores.

A fiber drawing tower, as shown in Figure 2.17 consists of many components. The preform in-feed system is controlled by the amount of material consumption in the oven. The graphite oven, reaching temperatures above 2000° is working in a gas environment to prevent oxidation. Coating filers apply the coating in one or a few

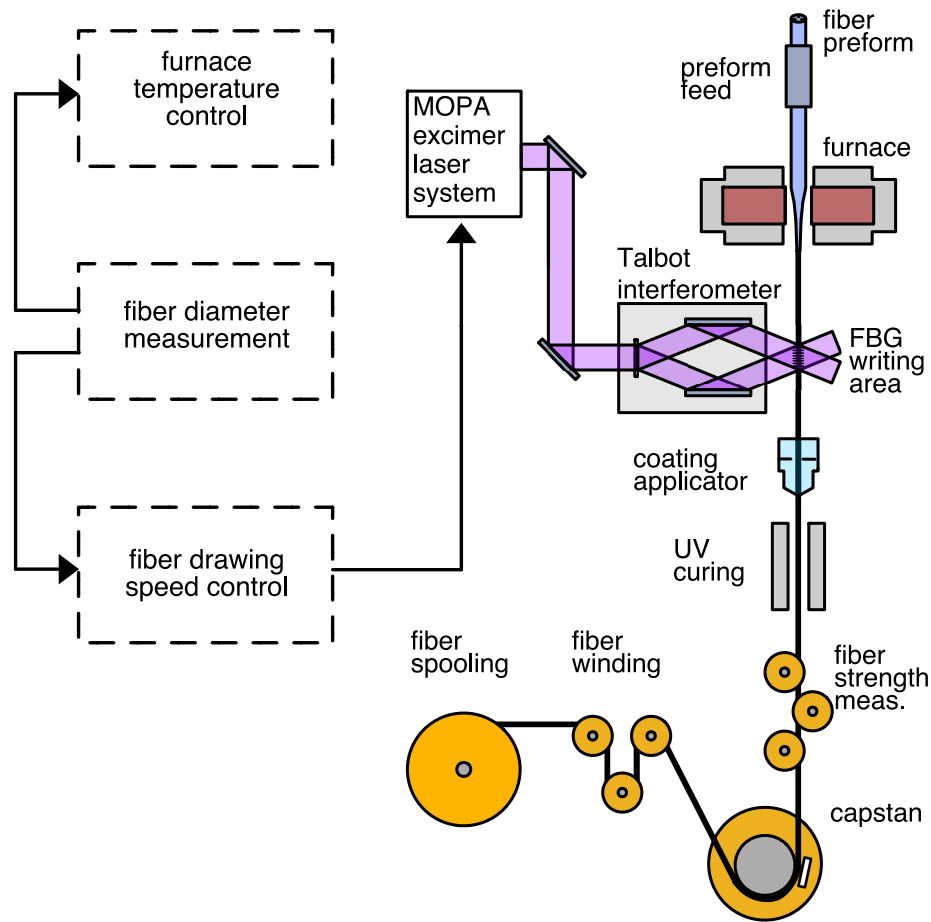


FIGURE 2.17: Schematic of a fiber drawing process.

steps with the following curing by the UV lamp. The tractor regulates the drawing speed depending on the measured fiber diameter. Then the fiber is wound on a spool.

### 2.3.2 Fanouts, splicing and channels management

Multicore optical fibers were demonstrated to comply with ITU-T Recommendations [143–149], but until today there is no standard for a multicore fiber [150, 151]. Lack of general standard classifies multicore fibers as a specialty optical fibers. Most commonly used single mode fibers in the telecommunication industry have very similar geometrical parameters, tolerances, mode field diameters and are often interchangeable. High-precision instrumentation has been developed to work with such fibers and has been made accessible through mass production. Handling protocols for single mode optical fiber have been established.

On the other hand, multicore fibers require more complex devices and additional equipment, development of which is not concentrated on a specific design but instead spread between fibers with the different number of cores, core-to-center

distances, and other variable parameters. Multicore fibers are usually made with fibers outer diameter of 125  $\mu\text{m}$  identical to telecommunication fibers, and the same coating materials are applied. This allows sharing cleaving and stripping equipment with standard single-mode fibers such as SMF-28. The process of stripping the fiber is identical to single-core fibers. Cleaving is more demanding in terms of quality since cracks on a cleave, which happen often and can be ignored for splicing single-core fibers, can result in poor connection with the multipole cores suffering from the crack.

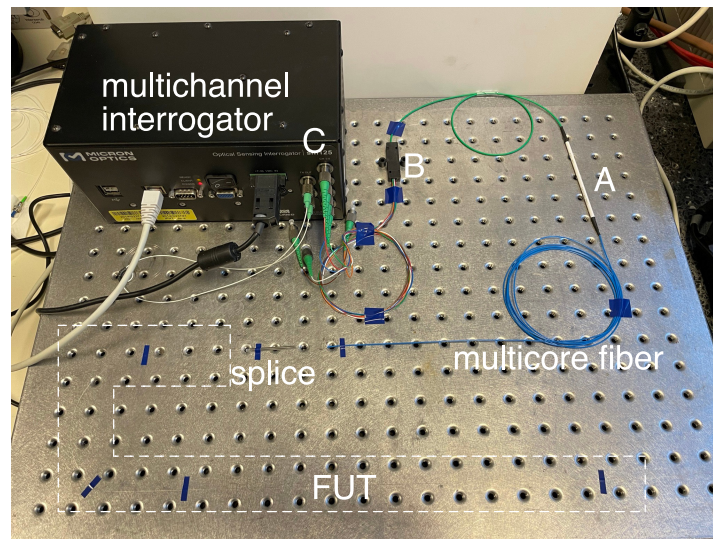


FIGURE 2.18: Typical multicore fiber measurement setup. Multicore fiber is marked by FUT, it is spliced to a fanout. Fanout consists of three parts. identical multicore fiber or a fiber with similar design, multicore fiber of the fanout is coupled to bundled fibers marked A. Bundled fibers are separated into individually jacketed fibers in the box B. C - multiple fiber connectors plugged in the multichannel interrogator.

The general utilization of multicore fibers is more complex, and the typical interrogation scheme includes a fanout device and a multichannel interrogator (Figure 2.18).

### Splicing multicore fibers

The current techniques for multicore optical waveguides splicing [152] are similar to alignment of polarization-maintaining fibers, which have no complete rotational symmetry [153–157] and rely on the white light illumination and allocation of the focal points. The automatic regimes, used in commercial splicers for splicing fibers with respect to their orientation are not applicable to multicore fibers or have low reliability. Precise alignment of the fibers must be completed by a visual comparison of the end facets of the cleaved fibers to prevent the common errors of the automatic method (Figure 2.19).

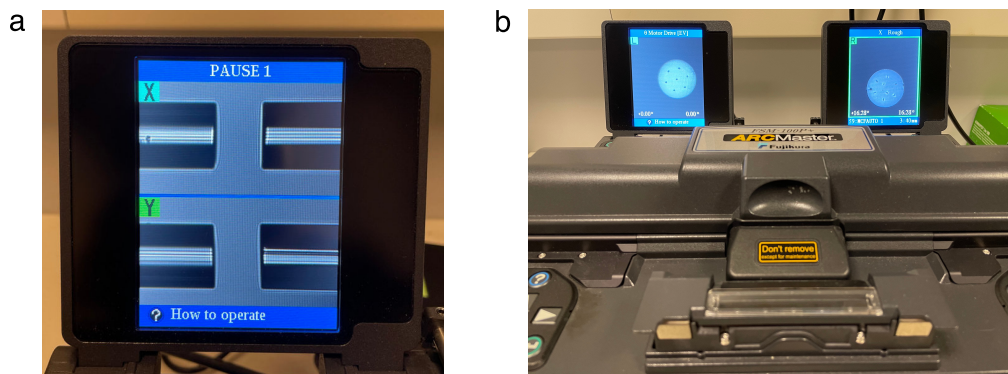


FIGURE 2.19: Multicore fiber splicing procedure. a) - Fibers side-view observation method. b) - Fibers end facets observation method.

After setting the orientation for both fiber ends, the splicer retains the angle and performs the splice normally. This method ensures that cores will be connected and even enables splicing fibers with different designs, e.g., single-core fiber to a multicore fiber or eight core fiber to a seven-core fiber as shown in Figure 2.20. In this case, only six cores (marked in green circles) would be interconnected.

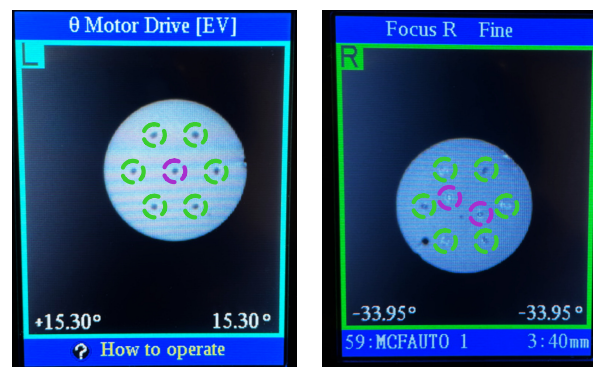


FIGURE 2.20: Fujikura 100p+ optical fiber splicer screen. Six cores of a seven-core fiber (marked green on the left side) are spliced to six cores of an eight core fiber (marked green on the right side).

The process of splicing multicore fibers is generally more complex and time consuming. Most of the splicing of multicore fibers has to be done semi-manually. This limits the use of multicore fiber in both telecommunication networks and sensing systems.

### Fan-in/fan-out devices

The most common scenario in multicore fibers splicing operations is the connection to a fan-in/fan-out (can be the same device, later referred to as fanout). Fanout is a device allowing for out-coupling the signals from each core of a multicore fiber into individual fibers or coupling a signal from several separate fibers to the cores



of a multicore fiber [158–161]. Fanouts up to date do not have a standard following a lack of a standard for multicore fibers in terms of design, and thus typically, they are custom-made. There are two types or manufacturing methods for fanouts. First type is the bundle of fibers (Figure 2.21a). This type of a fanout is made of a bundle of single-core fibers glued together. The fixed end then can be tapered to reach the required dimension for distance between the fiber cores to match this parameter with a specific multicore fiber. The second fanout type is based on a photonic lantern - a glass block with optical waveguides inscribed using a focused laser beam. A focused laser beam can locally modify (increase) the refractive index of glass and create a continuous trace. This allows to organize waveguides inside a glass block in such a way that it will match a multicore fiber design on one interface (or fringe) and will comfortably distance them on the other interface (Figure 2.21b).

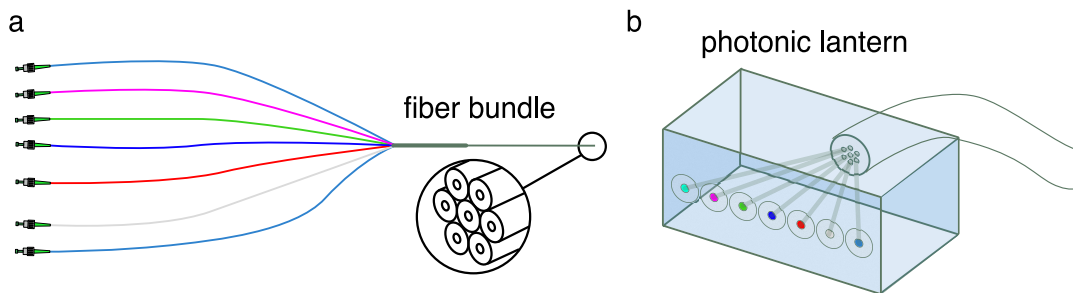


FIGURE 2.21: Fanout types. a) - Fiber bundle based fanout. b) - Photonic lantern based fanout.

After inscribing the waveguides, a multicore fiber can be glued to the surface, matching its design. Several single-core fibers are glued to the other surface to connect each single-core fiber to a corresponding core of a multicore fiber. The losses are typically lower in the fiber bundle since identical fiber can be used for bundling. The crystal used for the photonic lantern typically has a higher refractive index compared to the used fiber. Therefore, higher coupling losses are expected.

All in all, fanout is usually required for the operation with multicore fibers. Often new fibers are optimized for the use with existing fanouts due to high price and the complexity of manufacturing of new fanouts.

### Channels management

The multicore fiber connected to a fanout is ready to be used as a sensor. There are two regimes of core interrogation in this case. First is a simultaneous regime allowing for few cores measurement at a time. For such simultaneous measurement a multichannel interrogator is required. Multichannel interrogators used with shape sensors based on multicore fibers can provide real-time shape measurement.

The Micron Optics tunable laser interrogator as shown in Figure 2.22a, can be combined with a multiplexer, allowing for interrogating of 16 channels, four at a time. The OFDR reflectometer by 4DSP supports eight channels operating simultaneously (Figure 2.16c).

In the sequential regime, a single channel at a time can be measured, and the cores are interrogated in sequence. This way of interrogation does not require an interrogator with multiple channels. A multicore fiber with a spliced fanout can be connected to the interrogator via a fiber switch device (Figure 2.22c).

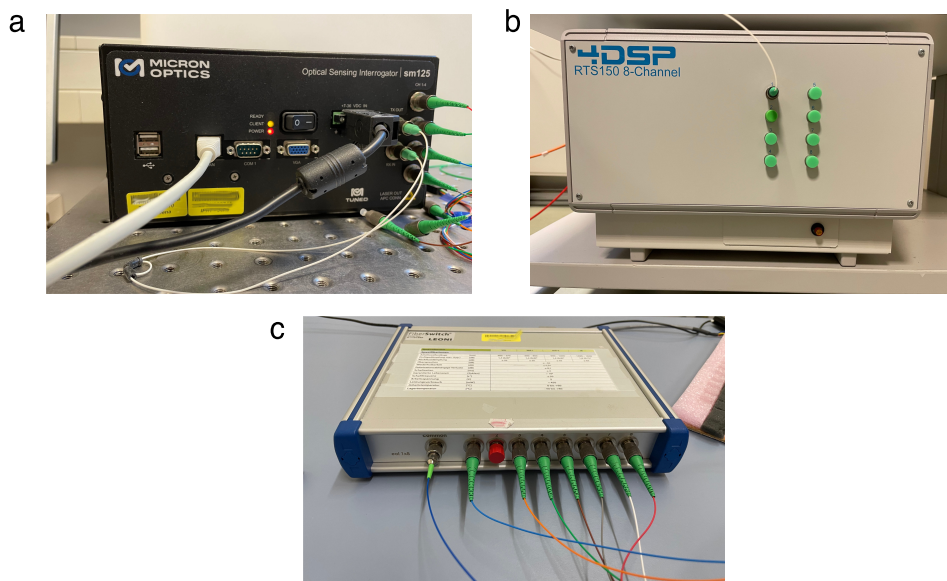


FIGURE 2.22: Devices optimized for multicore fiber connection. a) - Micron Optics tunable laser interrogator. b) - 4DSP multichannel OFDR. c) - Optical fiber switch with 8 fiber connectors.

Fiber switches can interconnect multiple input ports. One of the ports can be connected to a conventional single-channel interrogator. Other ports can be used by separate sensing fibers or a fanout. The configuration with the fanout allows for interrogating cores of a multicore fiber one at a time. Therefore, the signal from a specific core of a multicore fiber can be measured. After measurement for one core is finished, the switch can connect to the following core for the measurement. This concept can be used for applications where the interrogation frequency does not play a significant role, and the calculation does not rely on differential readings of the cores. Many demonstrations of shape sensors were done using single-channel interrogators. This allows for reconstructing of curvature - the shape, stable during a complete sequence of measurements.

The choice of the interrogation regime will depend on the dynamics of curvature measurement. The scheme with a fiber switch and single channel interrogator can be used for slow or discrete changes in shape. Typical fiber switch can operate with

a frequency above 1 kHz but any changes in shape between the cores reconnection will introduce measurement errors.

When dynamic measurement is required, a simultaneous cores interrogation is preferable.



## Chapter 3

# Angular properties characterization of multicore fibers

In this chapter, the issue of detecting the angular orientation of multicore fibers is studied. Angular orientation is an essential part of the accurate positioning of multicore fibers for many applications, such as shape sensing [162], optical fibers splicing [153], orientation-dependent FBG inscription [67], and multicore fibers characterization for a twist[163].

A method for multicore fibers orientation measurement via locating different cores or other distinct elements in the cladding is described and demonstrated. A scattering pattern of a fiber illuminated by a laser source is used for this structural analysis.

The presented method can measure the orientation along a fiber sensor in a scanning way and, thus, characterize it for the intrinsic twist. Intrinsic twist, as described in Chapter 2, occurs naturally in cylindrical optical waveguides during fiber drawing procedure and leads to inaccurate measurements, e.g., in torsion sensors [28, 164–167]. The intrinsic twist cannot be controlled unless a fiber has a preferable bending plane [168, 169], therefore fiber characterization via continuous orientation measurement during a fiber drawing process can also become an important application for the method presented in this chapter.

### 3.1 Measurement concept

The analysis of electromagnetic radiation penetrated through tissue is used in X-ray and tomography [170]. There, different kinds of tissue will be seen differently due to the varying density and absorption of electromagnetic waves. Similar to this, cores with differing refractive index and absorption ratio in a multicore optical fiber will modify a light field propagating through the fiber and become visible in the projection as a scattering pattern. This light field projection can be used as a fingerprint for a particular fiber orientation, and its position along the optical axis.

Therefore, this scattering pattern can be used for the recognition of specific fiber orientation.

A scattering pattern of a fiber illuminated by a laser source was already used for a birefringent optical fiber positioning [171]. Arkhipov et al. used laser light, scattered on a fiber and projected onto a screen, and then photographed the projection. This measurement method can be adapted here to multicore fibers and optimized in a few ways.

### 3.1.1 Optical scheme

When a laser illuminates multicore fiber with a beam diameter exceeding the fiber size, there are several sources that contribute to the light field propagating behind the fiber. The most energetic source is the light that circumvented the fiber. There is also light diffraction by the fiber, a focusing effect in the cladding, and the diffraction by the cores.

An optical scheme was developed to collect the diverging pattern produced by the illuminated fiber (Figure 3.1).

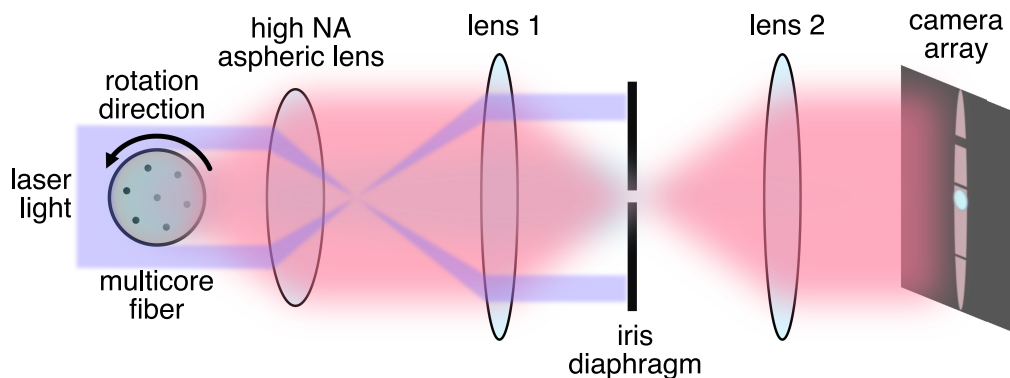


FIGURE 3.1: Optical scheme for scattering pattern projection onto a camera. Here colors represent laser beam modification: violet - direct laser beam bypassing the fiber, red - light scattered and refracted by the inner fiber structure.

In this optical arrangement, the scattering pattern is collected by an aspheric lens with high NA ( $>0.75$ ) and then filtered in a Keplerian telescope with a diaphragm inside. This optical scheme allows to remove direct laser illumination (depicted in violet in Figure 3.1) and partially filter light passing the fiber without scattering by inner elements. The scattering pattern recorded by the camera array is essentially the light highly diverging after passing through the fiber. It is interfering on a camera array and forming a specific fingerprint of a particular fiber orientation by the combination of bright and dark areas. This scattering pattern, in principle, can be used for reconstruction of the structure of an object using complex algorithms as often used in tomography [172–174]. However, structure reconstruction is an

excessive task for a fiber angular orientation measurement, since the fiber cross-section structure is already known.

### 3.1.2 Experimental setup

The setup consists of three sections: illumination, rotatable fiber clamps, and read-out system (Figure 3.2a). The fiber illumination is performed with a blue semiconductor laser (405 nm). The dark and bright areas on the camera (Figure 3.2b) are the result of interference, thus using coherent laser light is essential.

The motorized fiber clamps can be controlled by a computer. The grooves in the clamps are optimized for the coated fiber with a diameter of 250  $\mu\text{m}$ .

The read-out system is represented by a camera and high-NA objective containing an optical scheme shown in Figure 3.1. The camera is synchronized with the controller of the fiber rotators. The scattering patterns are recorded automatically with specified steps for a given range of orientations, e.g., for one complete rotation. This synchronization allows for collecting scattering patterns in a repeatable way.

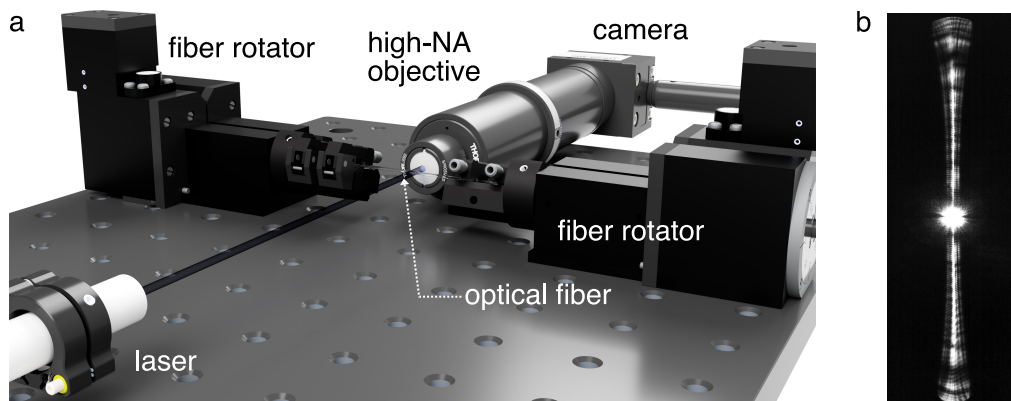


FIGURE 3.2: Experimental setups and a single measured scattering pattern. a) - Rendered model of a setup for scattering patterns recording during optical fiber rotation. b) - An example of a single scattering pattern of a 7-core fiber registered on a camera.

For the purpose of the intrinsic twist or torsion measurement a similar setup is used. To provide a scanning possibility, the fiber holders are placed on a linear translation stage moving perpendicular to the laser axis (Figure 3.3).

The distance between the fiber and the read-out system is optimized for a fixed value in a way that the light focused by the cladding is collimated by the high-NA aspheric lens. Therefore, the same distance between the fiber and the objective must be ensured in all positions of the moving platform.

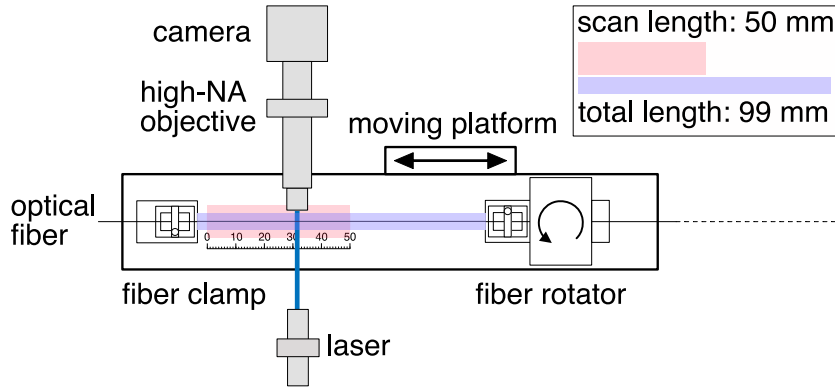


FIGURE 3.3: Setup schematic for a twist measurement along the fiber used in the experiments.

### 3.1.3 Cross-correlation

For associating a particular scattering pattern that corresponds to a certain fiber orientation with a set of reference patterns, a comparison based on Pearson's correlation coefficient  $\rho_j$  is used:

$$\rho_j(E, R_j) = \frac{1}{N-1} \sum_{i=1}^N \left( \frac{E_i - \mu_E}{\sigma_E} \right) \left( \frac{R_{i,j} - \mu_{R_j}}{\sigma_{R_j}} \right) \quad (3.1)$$

Here,  $E$  is a measured one-dimensional scattering pattern (1D data array) with elements  $E_i$ , where  $i$  indicates the pixel number.  $R_j$  with elements  $R_{i,j}$  is one of  $j$  scattering patterns (measured or simulated) taken from a reference data set with elements  $R_{i,j}$ , where  $i$  indicates the pixel or simulated detector element number and where  $j$  corresponds to particular fiber orientation. The variables  $\mu_E$ ,  $\mu_{R_j}$  and  $\sigma_E$ ,  $\sigma_{R_j}$  are the mean and standard deviations for the elements of data arrays  $E$  and  $R_j$ , respectively. The parameter  $\rho_j$  allows for analyzing the cross-correlation between a measured scattering pattern and the orientation-dependent reference patterns. The maximum value of  $\rho$  is thus expected to indicate the orientation of the measured fiber.

The angular orientation is determined by the scattering pattern from the reference with the highest Pearson coefficient, which is associated with a certain fiber angle. The suggested method is sensitive to both the fiber orientation and its position in respect to the objective. Nevertheless, a slight offset (about  $10 \mu\text{m}$ ) from the rotation axis can be accepted, which was observed from applying the same setup for slightly larger fibers that are not optimal for the fiber rotators.



### 3.1.4 Alternative methods

There are few alternative methods available for structural analysis of optical fibers and therefore, angular orientation, such as holography [175–179], lens effect tracing [155] or end facet imaging. Nevertheless, the suggested method is preferable due to universality and the ability to perform the measurement from aside, distant from the end facet. Holography has excessive sensitivity, which may cause an inability to associate holographic images because of the sensitivity of the fiber position regarding the objective or screen. In addition, a small deviation in fiber parameters leads to errors and limits the applicability of the holographic method. The suggested method has advantages in terms of tolerances. Lens effect tracing is used in commercial optical fiber splicers offered for polarization-maintaining fibers, such as Fujikura FSM 100P and Fujikura FSM 100P+. It can be applied to multicore optical fibers for finding a particular orientation for splicing. This method is limited to fibers with only a few core elements due to the limited analysis capabilities.

## 3.2 Measurement for orientation and twist in various complex fibers

Several different optical fibers were used for testing the method. All fibers were manufactured at Leibniz Institute of Photonic Technology using the stack-and-draw technique. Each of the tested fibers has a unique structure with multiple core elements (Figure 3.4).

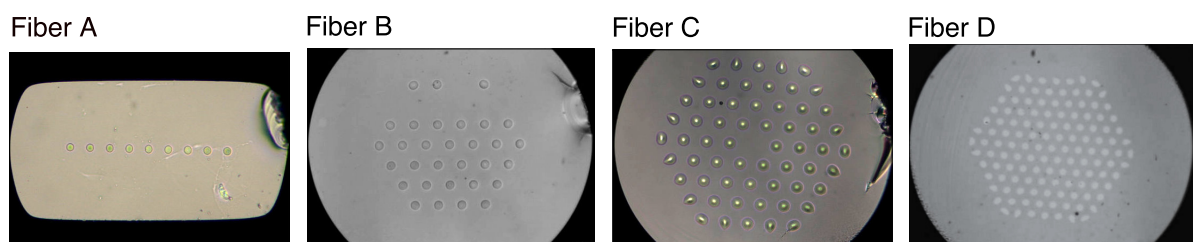


FIGURE 3.4: Microscope images of the cross-sections of the tested optical fibers. Fiber A - ribbon multicore fiber with nine cores in line and two flat sides. Fiber B - asymmetric 31-core fiber with a hexagonal cores arrangement. Fiber C - all-solid photonic bandgap fiber, grid elements are in a hexagonal arrangement. Fiber D - multicore fiber with 127 cores in a hexagonal arrangement.

Fiber A used for the experiment has nine cores arranged in a line. Often, such fibers are referred to as ‘ribbon’ fibers due to the polished sides. This is achieved by polishing or cutting a typical cylindrical fiber preform. This fiber has a diameter of  $125\ \mu\text{m}$  between the curved edges. The fiber structure has a rotational symmetry of  $180^\circ$ .

Fiber B has 31 cores arranged in a hexagonal structure. This fiber has a diameter of 125  $\mu\text{m}$  and is asymmetric.

Fiber C is an all-solid photonic bandgap fiber with multiple elements of the grid with different refractive indices. Grid elements are arranged in a hexagonal shape, the fiber diameter is 125  $\mu\text{m}$ , and it has a  $60^\circ$  of rotational symmetry.

Fiber D has 127 core elements in a hexagonal arrangement, 125  $\mu\text{m}$  in diameter and  $60^\circ$  of rotational symmetry.

### 3.2.1 Scattering patterns of the tested fibers

Complex optical fibers manufactured using the stack-and-draw method are often designed with a hexagonal structure. Since the scattering pattern used for the structural analysis is composed of multiple scattering and focusing effects, it would be expected that a more complex fiber structure produces a scattering pattern with more details. All fibers have the same outer diameter of 125  $\mu\text{m}$  (in the case of fiber A the outer diameter is the longest distance between curved sides) and identical focusing lengths of the cladding. Thus, the distance from fiber to the objective was the same in all experiments.

Each fiber was installed in fiber clamps in a random unknown orientation. The scattering pattern was recorded for one complete rotation with a step of  $0.3^\circ$ . Scattering patterns of fibers A, B, C, and D are shown in Figure 3.5).

As expected, the recorded scattering patterns have symmetries corresponding to the measured fiber structure. The scattering patterns of fiber A have areas with low scattering intensities (indicated in white color). This can be explained by the light field propagating through the polished sides of fiber A without refraction, nearly parallel to the laser axis. Therefore, the light, which was not scattered by the core elements, has been filtered by the iris diaphragm in the Keplerian telescope. In the scattering patterns of the fibers B, C, and D, distinct bright spots can be seen. These spots appear with a periodicity of  $60^\circ$  and correspond to the positions where the cores of the fiber structure line up parallel to the axis of the incident laser beam.

### 3.2.2 Orientation measurement based on cross-correlation

Orientation recognition based on cross-correlation of a scattering pattern was applied to the tested fibers. For this, the coefficient of correlation between one scattering pattern and a reference was measured.

For the reference collection, each fiber was installed in the measurement setup rotated for  $720^\circ$  with a step of  $0.3^\circ$ . Then one pattern of the set was selected as an experimental measurement. For each fiber, a scattering pattern recorded at the

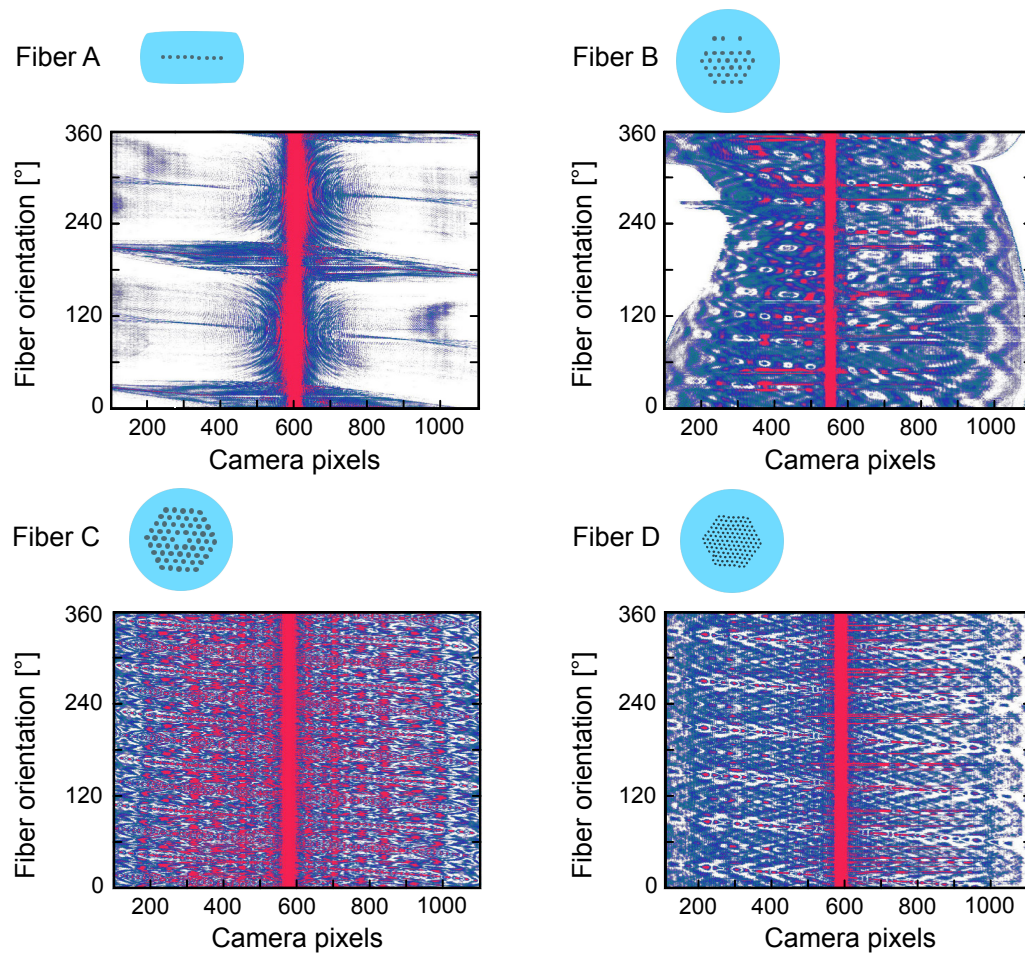


FIGURE 3.5: Scattering patterns of the tested optical fibers recorded for one complete rotation.

illumination angle of  $100^\circ$  was chosen as an experimental pattern E with a number of elements of  $i$  (see Equation 3.1). Since the fibers were installed in a random starting position, the chosen angle represents a random pattern selection. For the reference pattern R, one of the 2400 patterns was used consequently for the calculation of the correlation coefficient  $\rho_j$ . The correlation coefficient was plotted against the corresponding orientation for fibers A, B, C, and D in Figure 3.6.

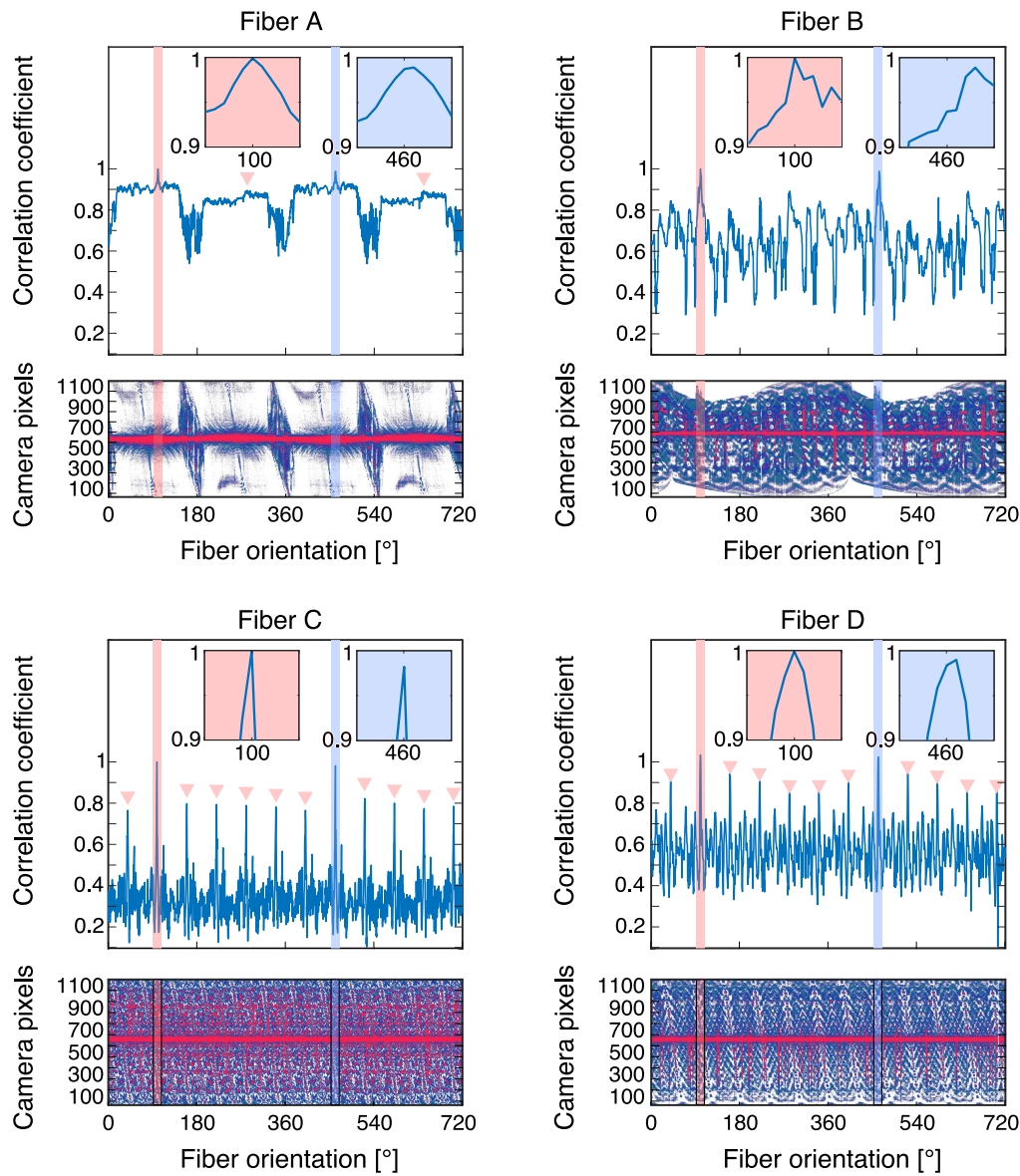


FIGURE 3.6: Cross-correlation  $\rho_j$  calculation applied to the tested fibers. The upper line is the correlation coefficient of a pattern extracted at the orientation position of 100 degrees (red bar) and two complete rotations. The blue bar corresponds to the same position after one complete turn. Colored insets show the 3°-width region of the highest values in detail. Correlation coefficient peaks correspond to the symmetric positions of the fibers (red triangles).

As seen from the Pearson's coefficient plotted against the angle, the highest value is achieved for auto-correlation at 100 degrees. The second highest value was at the region of 460 degrees, which is the exact orientation of the fiber after one complete rotation. Multiple maxima of the correlation coefficient plot indicate the symmetric orientations. However, the symmetric orientations still have lower contrast which a few factors can explain. The first factor is the uniqueness of a particular fiber orientation. Despite being similar visually, the cores are slightly deformed and misplaced during the fiber manufacturing process. This is sufficient to reduce the similarity between the scattering patterns of two symmetrical orientations. The second factor is the distance between the fiber and the objective. It can vary during the rotation due to the shifted center of rotation. This can happen because the coated fiber thickness is slightly offset from the optimal diameter for the used fiber clamps.

The contrast of Pearson's coefficient also depends on the fiber structure and details present in the scattering pattern. This is visible for the case of fiber A and C. Lower contrast in the case of fiber B is explained by the similarity of the scattering patterns in the false-symmetry orientations. This leads to a stronger correlation with similar scattering patterns and reduced contrast overall. Fibers C and D, on the contrary, have very detailed scattering patterns and, thus, good contrast of Pearson's coefficient.

### 3.2.3 Using simulated reference pattern stacks

For applications where the reference patterns cannot be measured experimentally, e.g., as the fiber drawing process, there is an interest in obtaining the reference using optical simulations. Lumerical FDTD (finite-difference time-domain) simulation software was used to replicate the reference pattern measurement. The simulation was made for a simplified model without considering possible differences in a core-to-center distance and the deformation of the core. The actual seven-core fiber and its model can be seen in Figure 3.7.

The simulation was performed for a range of  $60^\circ$  with a step size of  $1^\circ$ . The experimental reference patterns were recorded for  $720^\circ$  with a rotation step size of  $0.3^\circ$ . Then the obtained references were cropped to match the simulated reference patterns for visual comparison of the patterns (Figure 3.8 a and b). Also, to check the capabilities of the correlation coefficient-based measurement, seven-core fiber scattering patterns' were recorded without removing the coating for two rotations and a step size of  $0.3^\circ$  and cropped accordingly (Figure 3.8c).

The experimental reference pattern stack is visually similar to the simulated patterns. The main difference in Figure 3.8a and b stems from the central region where

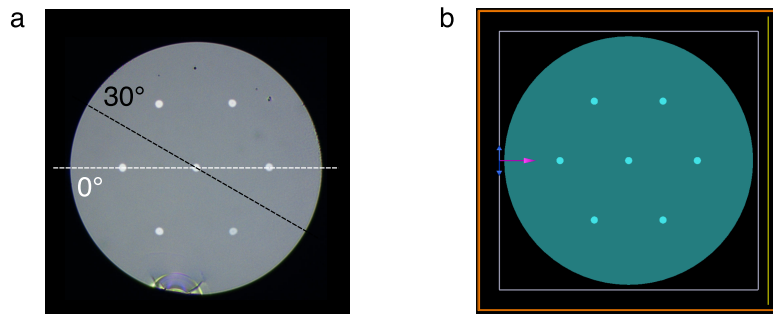


FIGURE 3.7: Comparison of the tested seven-core fiber and of its' simulated model. a) - Cross-section of a seven-core fiber, b) - Model of a seven-core fiber used for the simulation.

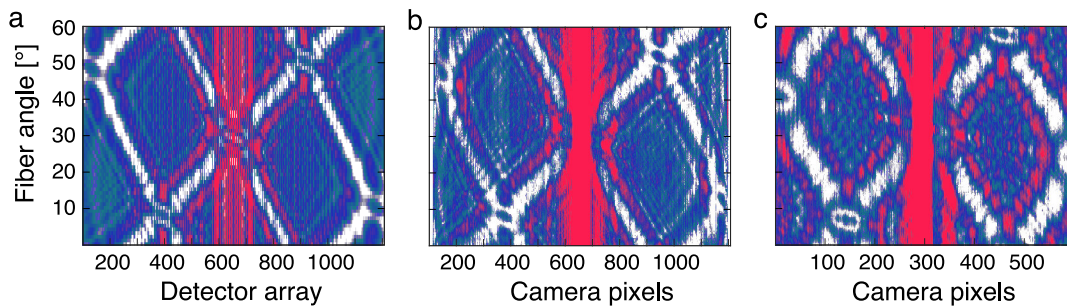


FIGURE 3.8: Simulated and experimental scattering pattern stacks for a seven-core fiber. a) - FDTD simulation of scattering patterns of a simplified model of a seven-core fiber, b) - Experimental scattering pattern of a seven-core fiber without coating, c) - Experimental scattering pattern of a coated optical fiber.

the image is saturated for the experimental results and still has details for the simulation results. This comes from a wider dynamic range of the detector in the simulation software while the camera in experimental patterns demonstrates saturation in the central region. There are also some artifacts in the experimental stacks, which presumably come from the dust particles or minor scratches on the surface of the uncoated fiber and from coating eccentricity and non-uniformity of the fiber in a coating. The optical properties of fiber coatings are usually not considered, hence, the applicability of the orientation measurement method might be limited for such coated fibers.

To verify the possibility of using a simulated reference pattern for the orientation measurement of an actual fiber, the cross-correlation of a scattering pattern from the simulation stack and two actual experimental stacks was performed for an uncoated fiber and for a fiber in a coating as shown in Figure 3.9.

The contrast of the correlation coefficient, defined as the difference between the minimum and maximum values, is lower for the simulated patterns than for the actual fiber (see, e.g., Figures 3.6 and 3.9 for comparison). However, the Pearson's

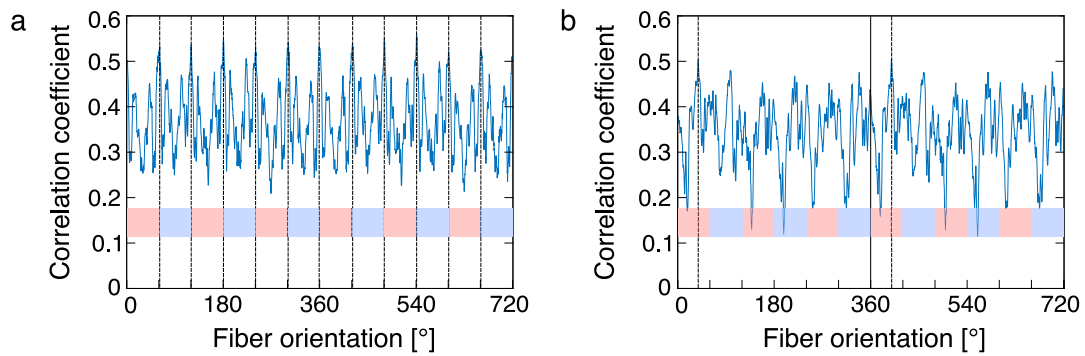


FIGURE 3.9: Scattering pattern from a simulation correlated to experimental results: a) - correlation coefficient of simulation with an uncoated fiber, b) - correlation coefficient of simulation with a fiber in a coating

coefficient peaks indicate the correct angular orientations using the scattering patterns obtained from the simulation. Hence, the described method can also be used with a simulated reference to measure optical fibers angular orientation. The flexibility of the method can also be seen in the correlation coefficient measurement results applied to the scattering patterns of a fiber in a coating. Despite the modification of the original scattering pattern by the coating, the method identified the scattering patterns corresponding to the orientation of the simulated fiber.

### 3.2.4 Optical fiber twist measurement

Twist is an important parameter for multicore optical fibers [180–182]. There are two types of twist that can be found in multicore optical fibers. The first is the designed twist - the intentional twist imprinted in a multicore fiber to achieve a helical shape of cores. As described in Chapter 2, this can be beneficial for shape sensors. The designed twist enables direction-sensitive torsion measurement.

The second type of twist is unintentional, often called ‘intrinsic’ - the twist occurring naturally during the fiber production process due to axial fiber rotation on a cylindrical capstan. A typical designed twist in shape sensors has a period of about 2 cm and is considerably stronger than naturally occurring twist.

However, the presence of designed twist does not exclude the intrinsic twist. In this case, the intrinsic twist locally modifies the designed twist period, which results in a changing twist period over the fiber length. Hence, the measurement of twist would be beneficial for all multicore fibers.

The orientation measurement continuously applied to a fiber allows for measuring the change of the cores position in the cladding. For the demonstration of the presented method applied to a twist measurement, a seven-core fiber was used. To perform a twist detection and measurement, the orientation measurement setup was

moved along the fiber axis. The distance between the clamps was 99 mm. The scan was performed on a 50 mm piece of this length with a step size of 0.1 mm. The fiber used for the tests has no designed twist. Therefore, different external twists were applied to detect the change of the cores position in the fiber. The fiber was measured first in a relaxed condition and then twisted by a fiber rotator on one side for 1, 3, 10, 30, 60, 90, and 180 degrees, respectively. The coating was removed to ensure that the twist was transferred to the fiber, and the fiber was glued to the clamps. The stack of scattering patterns for the different forced twists is shown in Figure 3.10.

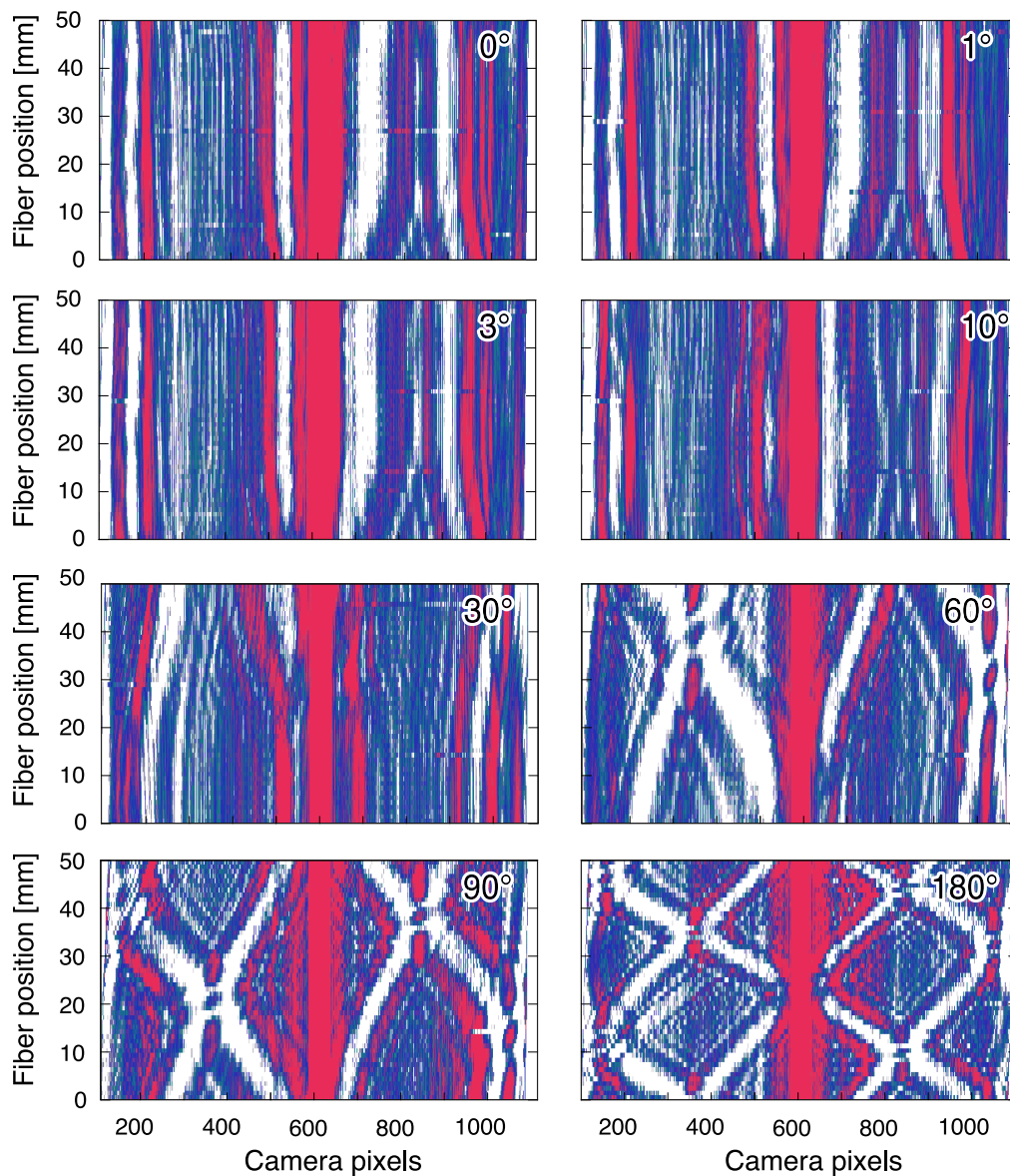


FIGURE 3.10: Scattering patterns of a seven-core fiber measured over 50 mm length of measurement. Applied external twist is indicated in the top right corner of each scattering pattern stack.

The stack of scattering patterns for an untwisted fiber should be composed of



identical patterns. Therefore, parallel lines should be seen in the stack formed by dark and bright areas. However, for the experiment with a relaxed fiber, curved lines can be seen. This indicated the presence of a twist in a relaxed fiber. This means that the tested piece of a seven-core fiber has an intrinsic twist. The curved lines in the stack straighten with an external twist applied to the fiber. At the angle of  $10^\circ$ , only a limited central part of the stack remains slightly curved. This means that at this condition, the cores were straightened, and the intrinsic twist was compensated by the externally applied twist. This also indicates that the intrinsic twist is counter-directed to the externally applied twist. After applying the external twist of  $30^\circ$ , the lines become curved again. The curvature reached its maximum for these measurements at the value of twist of  $180^\circ$  (half a rotation).

The orientation measurement based on the correlation coefficient calculation was applied to the experiment. The maxima of correlation coefficients were plotted, which allows for measuring the change of the fiber angular orientation depending on the fiber position. The results are shown in Figure 3.11.

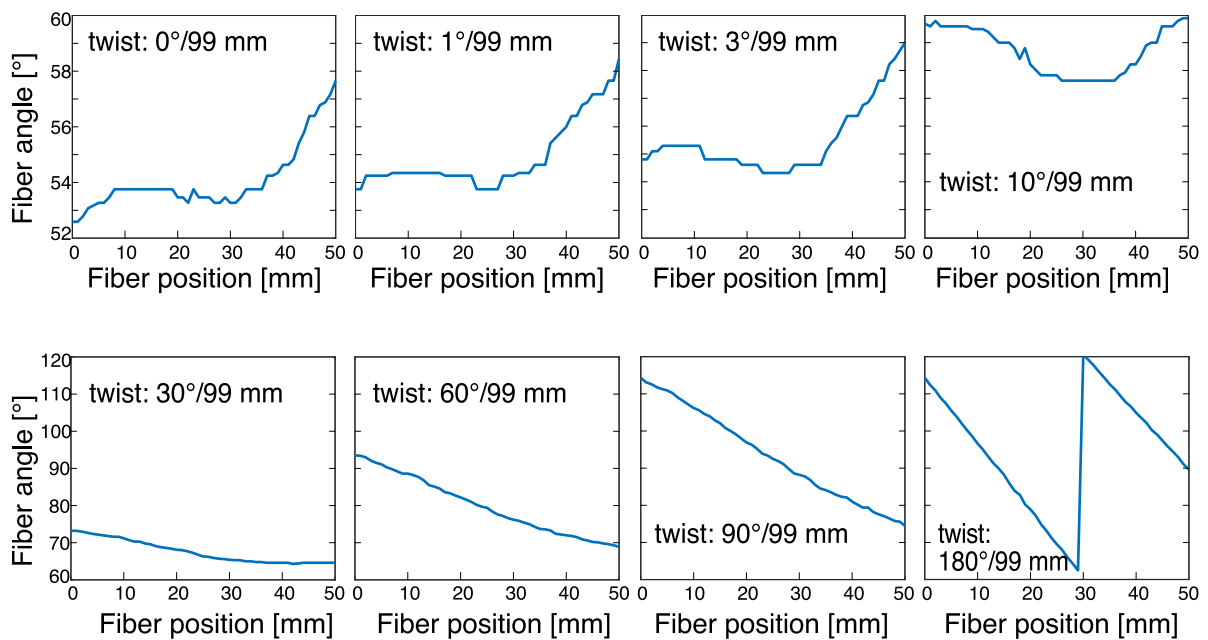


FIGURE 3.11: Twist measured in a seven-core fiber a relaxed condition and with an external twist applied. Non-uniformity of the fiber orientation along the length is confirmed by multiple measurements. The intrinsic twist is present in a relaxed fiber. The intrinsic twist is counter-directed to applied external twist.

Notably, the fiber in the relaxed condition shows an intrinsic twist of more than 5 degrees on the length of 50 mm. Twist distribution on the measured length of fiber is distributed non-uniformly and even changes direction. The intrinsic twist was counter-directed to the externally applied twist. The intrinsic twist is partially

compensated by an applied twist of about  $10^\circ/99$  mm, but due to complex distribution between 10 and 50 mm cannot be eliminated completely by the externally applied torsion. Overall, the measured intrinsic twist agrees in all measurements performed.

This experiment shows that the intrinsic twist appears in fibers with no designed twist. This orientation measurement presented in this chapter is applicable to a twist measurement in complex fibers.

### **3.3 Summary**

The method of the structural analysis of transparent objects based on the illumination projection can be found in various fields. It is also widely used in optics. In this chapter, a method for angular orientations measurement of optical fibers with multiple elements in the cladding was demonstrated. The orientation measurement system allows recording the scattering patterns for multiple angular orientations and finding the orientation angle by measuring the correlation coefficient with an experimental or simulated reference scattering pattern. The method was verified for several complex fibers, such as seven-core fiber, ribbon multicore fiber, all-solid photonic crystal fiber, and a multicore fiber with an asymmetric structure. The fibers with more structural elements have scattering patterns with more details, being potentially beneficial for more accurate orientation measurement. When used in a scanning manner on a piece of fiber, the intrinsic twist present in a scanned fiber piece can also be measured. Since it is challenging to avoid an intrinsic twist during the fiber drawing process, the intrinsic twist measurement can help to compensate for the twist. The twist measurement can improve the performance of shape sensors based on multicore fibers.

## Chapter 4

# Optimizing FBG inscription in multicore fibers

It is well known that FBG inscription in multicore fiber is more complex than an inscription in conventional single-mode single-core fiber [183, 184]. The reflectivity difference of FBGs simultaneously inscribed in identical cores of a multicore fiber will mainly depend on the laser-induced refractive index modulation depth  $\Delta n_{\text{mod}}$  as can be seen in Equation 4.1 (from Equations 2.10 and 2.11):

$$R = \tanh^2\left(\frac{\pi\Delta n_{\text{mod}}\eta L}{\lambda_B}\right) \quad (4.1)$$

The refractive index modulation depth, in turn, depends on the laser light distribution in the fiber. Laser light enters the fiber and gets focused by the cylindrical cladding, which can be further shaded, scattered, and focused by multiple fiber cores. Therefore, as shown in Figure 4.1, e.g., cores A and B will have different illumination conditions. When the multicore fiber is illuminated for an FBG inscription, it is expected that gratings in the cores A and B will give different reflectivity.

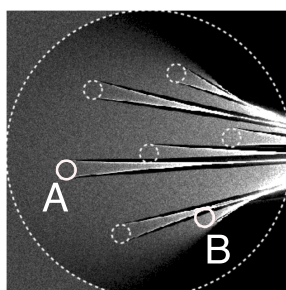


FIGURE 4.1: Model of a cross section of a seven-core fiber with propagating illumination beam. Light propagation from left to right side. Cores A and B have different illumination conditions.

Consistently low reflectivity gratings in the core A and consistently high reflectivity gratings in the core B can be interrogated appropriately via adjustment of the sensitivity in the core. However, for the consistency of the reflectivity of gratings in

a multicore fiber, the illumination conditions should not change during the inscription of a complete array. The stability of the illumination conditions often cannot be ensured.

In the case when the gratings are inscribed during the fiber drawing process, the fiber orientation regarding the laser beam cannot be fixed due to the intrinsic twist often found in the cylindrical waveguides, as discussed in Chapter 3. This intrinsic twist leads to a fiber rotation during the drawing process and during the inscription of the grating arrays. Such fiber rotation from one inscribed grating to another will cause the relocation of the cores and will subject the cores to a varying illumination intensity. The twist might be eliminated if a fiber with a preferential bending plane is used.

In the case when the array of gratings is inscribed on an optical table, the consistent orientation of the fiber is still challenging. First, an orientation measurement must be used for consistently installing the fiber in the same specific orientation. Second, in the case of a seven-core fiber, similar to the shown in Figure 4.1, the orientation can be detected only with a limitation of the fiber symmetry. It is often impossible to distinguish the orientations of, e.g.,  $0^\circ$  and  $180^\circ$ . For the case shown in Figure 4.1, this will mean the reversed reflectivity of the gratings inscribed in the cores A and B within a single FBG array. So the fiber with an asymmetric structure would be required for an orientation tracking, e.g., fiber with a marking element, such as a hole.

The problem of uneven illumination conditions may be approached by increased laser illumination for FBG inscription. At a certain illumination level, saturation for photosensitivity is reached for some cores and further increase in illumination is not followed by higher reflectivity, e.g., in the cores located in the focused-light areas. The cores that are not in saturation, then might experience stronger gratings inscription.

However, cores that are subject to higher illumination conditions can experience inscription of gratings with broader reflection peaks. This solution is not optimal since a large difference in spectral width is not desirable. For heavily germanium doped fibers (above 15 mol%), strong illumination conditions introduce a risk of type II FBG formation. Such type II gratings are created by multiple localized melting centers as a result of the thermal outcome of the strong absorption process [185–189]. Type II FBGs have an identical period to the type I FBGs and, thus, identical central wavelength but typically they are several times broader (can reach 1 nm in grating bandwidth) and stronger in reflectivity (can reach 100% in a single-pulse inscription). The type II grating formation leads to a significant degradation of mechanical properties of an optical fiber and is not desirable for strain-based sensors.

Now we consider the solutions for interrogation of non-uniformly reflecting gratings in a single core. A spectrometer-based peak-tracking FBG interrogator typically does not register the spectral shape of each reflection peak. Instead, it estimates the center of mass of the reflection peak measured by a few pixels. It performs best with arrays of gratings with comparable amplitude and bandwidth. Commercial FBG interrogators based on tunable lasers also utilize peak recognition techniques requiring arrays of gratings with similar reflectivities. A combination of low reflectivity and high reflectivity FBGs requires lowered detection line level for the peaks in the spectral domain, which can lead to misinterpreting the measured spectrum as shown in Figure 4.2.

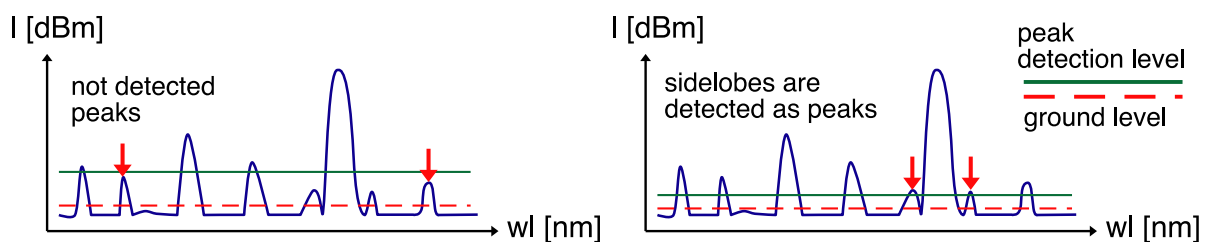


FIGURE 4.2: Peak tracking algorithm failure examples.

The problem of differently reflecting gratings could generally be solved by using special devices that use adaptive peak fitting algorithms. However, the special peak shape fitting algorithms are computationally demanding and not applicable to a high frequency measurements [190]. However, equal reflectivity Bragg gratings across multicore optical fiber are highly desirable [191].

There is no simple solution for achieving uniform Bragg gratings across the multicore fiber. Nevertheless, the difference of the achieved gratings must be studied for all laser illumination conditions, i.e., illumination orientations.

To optimize the procedure of inscribing FBGs and possibly adapt the fiber design, and select better illumination angles, it is required to study FBG inscription with different illumination conditions.

## 4.1 Ray tracing simulation of multicore fiber illumination

To evaluate the illumination difference occurring in a multicore fiber (seven-core fiber in our case, previously shown in Figure 3.7a in Chapter 3), it is possible to run a ray-tracing optical simulation to model a fiber illumination during an FBG inscription process. Despite the indirect transition of illumination intensity to the

FBG reflectivity, a comparative study can give an understanding of the best orientation for gratings uniformity. In our ray-tracing model, the absorption in the cores is not included due to the inability to estimate the UV light absorption in germania fibers accurately. In the literature, there are only few studies published, often with contradicting results [192–194]. Also, the reflectivity of the grating highly depends on multiple geometrical parameters affected in the fabrication process.

The graph shown in Figure 4.3a, indicates only the intensity of light present in a single core of a multicore fiber, offset from the center for  $36.5\ \mu\text{m}$ . Depending on the fiber angular orientation, this core is illuminated with different intensity, which reaches maximum values at around  $177^\circ$  and  $183^\circ$  (marked by arrows in Figure 4.3b).

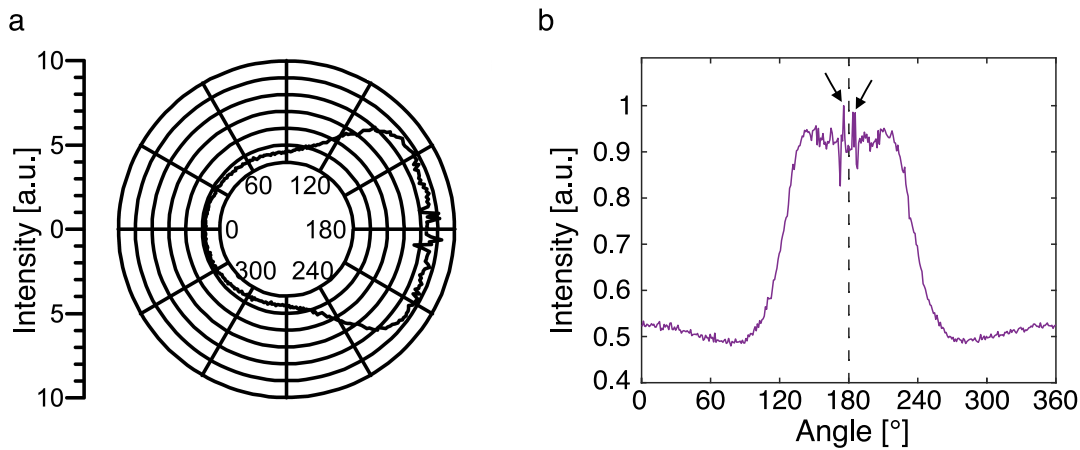


FIGURE 4.3: Intensity variation with orientation angle in an offset core in a multicore optical fiber illuminated by a UV light source presented in polar coordinates (a), and linear coordinates (b). Arrows indicate the maximum intensity values at  $177^\circ$  and  $183^\circ$ .

The cladding of the multicore fiber behaves like a cylindrical lens with a focal axis on a short distance behind the fiber. This leads to an increased illumination intensity at the backside of the cladding. The illumination intensity experienced by a core depending on the location can differ twice. Considering the distribution of the cores in a seven-core fiber, part of the cores will be subject to light exposure beyond saturation levels (here, the saturation level is defined as light intensity level beyond which the increase in the intensity will not contribute to a higher grating reflectivity).

In addition to the focusing effect in the cladding, diffraction on the edges of the core and focusing effects in the cores contribute to the complexity of the FBGs inscription condition. Angles of the maximum intensity and the angle in between are shown in the ray-tracing model in Figure 4.4.

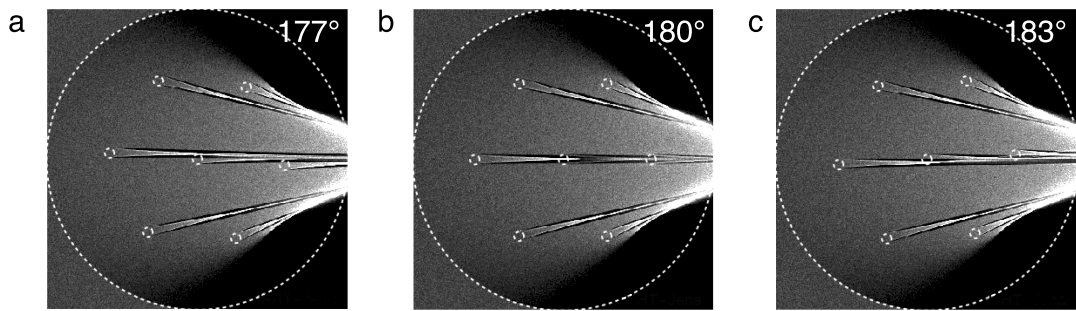


FIGURE 4.4: Simulation results of multicore fiber illumination by UV lightsource.

To present the illumination intensity in different cores simultaneously, the plot in polar coordinates can be transferred to linear coordinates and replicated six times with an angular shift of  $60^\circ$  (Figure 4.5a).

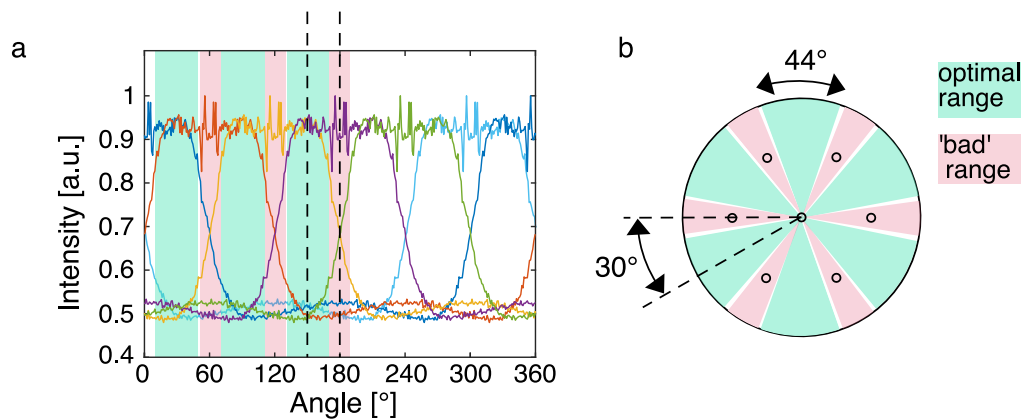


FIGURE 4.5: Light intensity in different cores of seven-core fiber over full rotation with identified bad and optimal ranges for FBG inscription. The region considered for the experiments later in Section 4.2, is marked between the dashed lines.

As can be seen, there are two states of illumination for the outer cores corresponding to the cores location. Lower level indicates the intensity values in the cores located on the fiber exposure side. Higher level corresponds to intensities experienced by the cores on the back side of the fiber where the focusing effects elevate the illumination intensity.

From the simulation results, ranges of illumination angles can be sorted into two groups. Optimal range of about  $44^\circ$  has similar illumination intensity of  $0.5 - 0.6$  a.u. for 4 out of 6 outer cores. The center of this preferable range of angles for FBG inscription is located at around  $150^\circ$  and is repeated every  $60^\circ$ , according to the fiber symmetry. The 'bad' range of angles has elevated illumination conditions for three outer cores with its center located at around  $180^\circ$  repeated every  $60^\circ$ . In the 'bad' regions, there are an especially bad angles present, e.g.,  $177^\circ$ , where one of the cores is located in the part of the fiber where it is subject to a complex combination of focused and diffracted light. To study the transformation of the illumination into

the final FBG reflectivity, experiments were carried for a simulated seven core fiber in the range of angles of  $30^\circ$ , indicated between the dashed lined in Figure 4.5b.

## 4.2 Experimental setup for FBG inscription

The task of the study is to inscribe Bragg gratings with different illumination angles, to measure the reflectivities for all cores, and to compare the results for different illumination angles with the simulation results. To be able to install the multicore fiber with the required orientation towards the laser beam, the setup described in Chapter 3 was used. One end of the fiber was installed in the rotatable clamps, and a camera measured its orientation with the high-NA objective. The other end was spliced to a fanout to measure the cores individually. The fanout was connected to a spectrum analyzer through a fiber switch, allowing for sequential measurement of the reflection spectrum of each core. The complete setup can be seen in Figure 4.6.

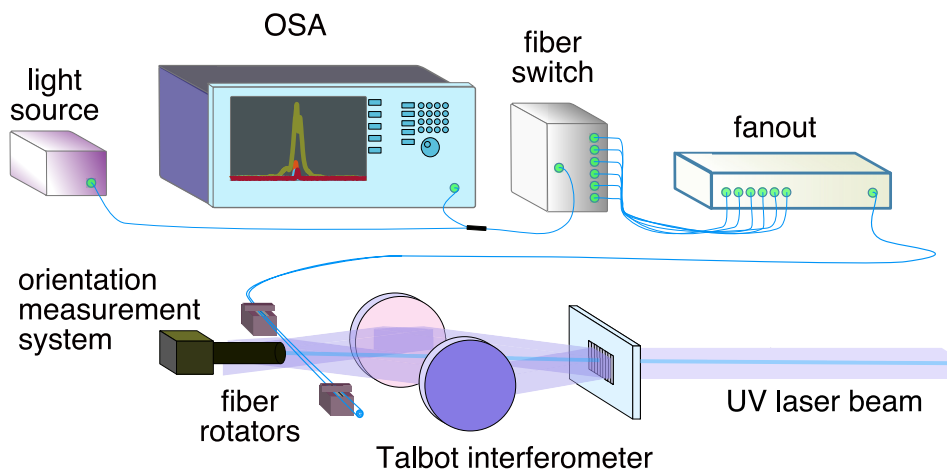


FIGURE 4.6: Scheme of FBG inscription setup with multicore angular positioning bench included.

For measuring the absolute reflectivity of the gratings in the cores, the reflected signal by a single grating in the core was normalized to the Fresnel reflection from the cleaved end of the fiber. Since the ratio of light reflected from a normal surface is known, and this reflection is subject to all other losses at fiber connections, the reflectivity of each single grating can be calculated relative to the incident light.

Bragg gratings were inscribed in a seven-core fiber with an angular shift of  $3^\circ$  - from  $150^\circ$  to  $180^\circ$  (Figure 4.7a). The seven-core fiber has a symmetry of  $60^\circ$ . There is also an additional reflection symmetry of  $30^\circ$ . Therefore, it is sufficient to analyze a  $30^\circ$  range.

The fiber orientation was ensured using the images (scattering patterns) from the orientation measurement setup. The angular position of  $150^\circ$  has a recognizable



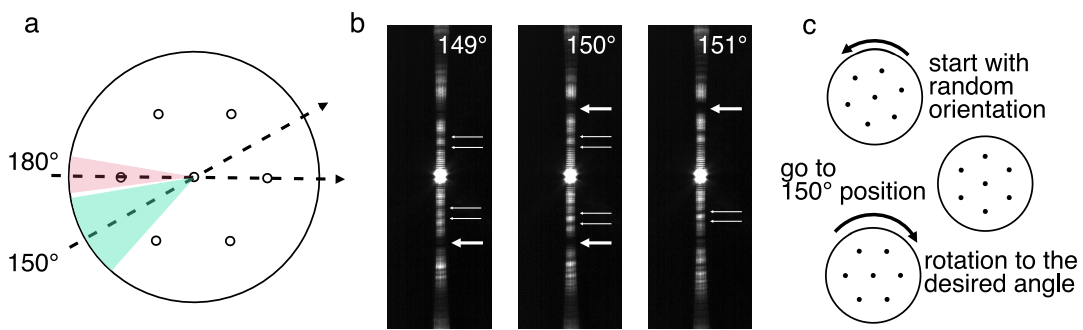


FIGURE 4.7: a) - The range of angles used in the experiment. b) - Scattering patterns measured at 149°, 150° and 151°. c) - The procedure for installing the fiber to the required angular orientation.

symmetric pattern, as shown in Figure 4.7b. Depending on the proximity to the 150° position, features marked with arrows in Figure 4.7b appear or fade. When this desired pattern is found, the fiber can be rotated to the required orientation (Figure 4.7c). The angle installation using this technique has an accuracy of about 0.3-0.6 degrees. All gratings were inscribed by a single pulse of a KrF excimer laser with an energy density of about 200mJ/cm<sup>2</sup>. The length of each grating is 5 mm. The spectra of the gratings were measured with a delay of a minute after inscription. This allows to wait for the rapid decay in reflectivity following the inscription process. This waiting period permits the grating to stabilize in reflectivity and to avoid that the relaxation affects the interrogation of the gratings in different cores, which is done sequentially.

### 4.3 Results and discussion

Fiber Bragg gratings were measured in all cores, normalized to the Fresnel reflection, and then were normalized to the strongest grating achieved in the same inscription process. This was done to neglect the effect of pulse energy variation, common in excimer lasers, and to compare directly the orientation from the perspective of grating uniformity or equality. The results for the optimal inscription range of angles are shown in Figure 4.8.

In the range which is assumed to be preferable for FBG inscription, the best result achieved between the weakest and the strongest grating was about 30 %. The angles of 153°, 159° and 162° showed the least variation in gratings reflectivity within the cross-section of a fiber. For the other angles, the difference was considerably higher, reaching more than 60% for the angles of 150°, 165°, 168° and 174°.

Two gratings were inscribed in a presumably 'bad' orientation for the FBG inscription. The angle of 177° presents an extreme case of the orientations endangering

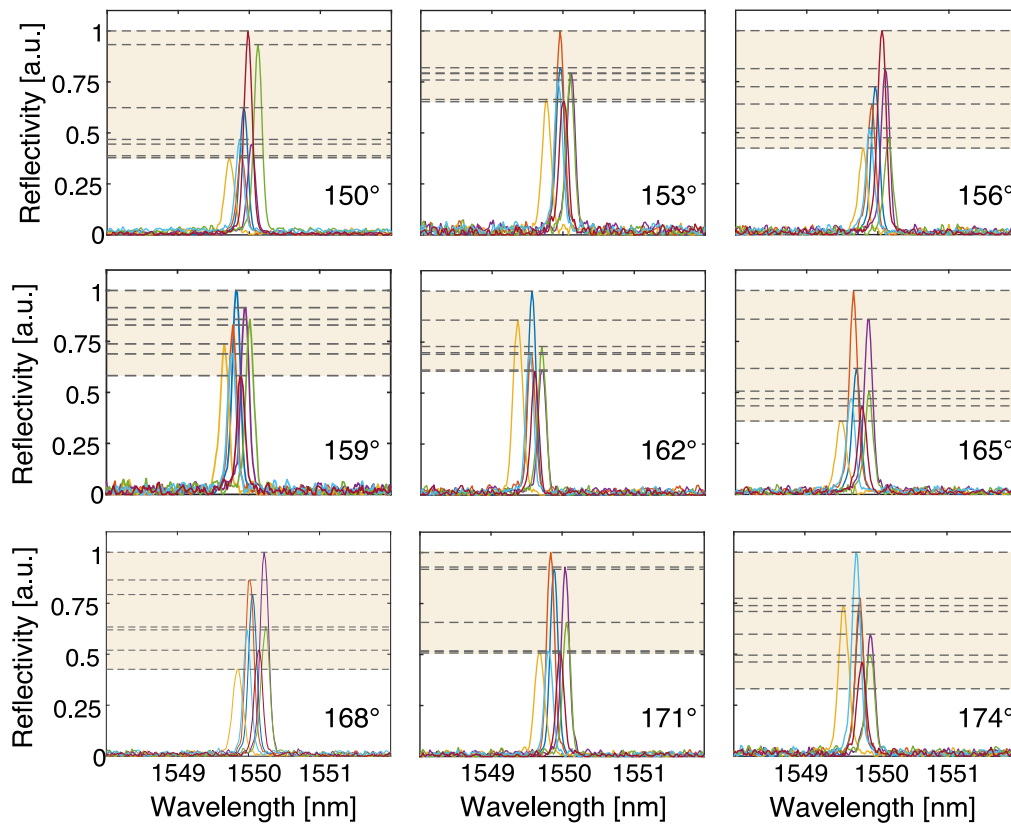


FIGURE 4.8: Results of FBGs inscription in a multicore fiber within an optimal illumination range of angles. Dashed horizontal lines indicate the individual gratings reflectivity level.

a complete array of gratings in the core. Incidence angle of  $177^\circ$ , as shown in Figure 4.4a, led to the FBG type II formation in the core (Figure 4.9a), which drastically reduces mechanical properties of the core and complete fiber. This type II FBG (depicted in the violet curve) has amplitude and bandwidth multiple times larger than type I FBG. The experiment for the FBG inscription with an incidence angle of  $177^\circ$  was repeated, and led to the core damage as an extreme case of type II FBG formation. This unwanted effect is caused by a combination of strong focusing in the cladding and the diffraction from other cores projected to one single core. Such type II grating formation, as well as the destruction of a core, might occur in the region at illumination angles of  $177^\circ$ ,  $183^\circ$  and others according to the fiber symmetry. These illumination angles should not be used for FBG inscription. When the ‘bad angles’ cannot be avoided, the illumination density must be reduced below the FBG type II formation level, to eliminate unwanted effects caused by such strong, focused laser beam exposure.

The orientation of ( $180^\circ$ , shown in 4.4b), does not stand out of other inscription sessions (Figure 4.9b). The laser light is focused in the first and central cores but also strongly absorbed in these photosensitive cores, which is compensated for strong

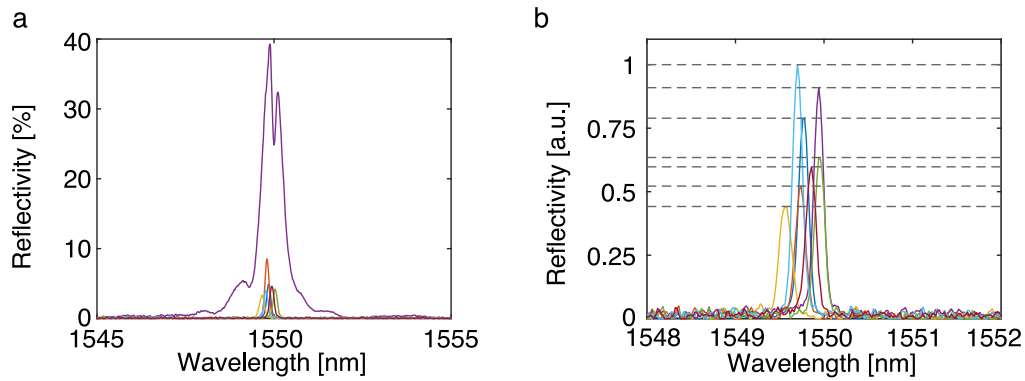


FIGURE 4.9: Reflection spectra of FBG inscribed in 'bad' range of orientations of multicore fiber. a) - Spectrum of gratings inscribed at  $177^\circ$ , b) - Spectrum of gratings inscribed at  $180^\circ$ .

focusing effects for the third core. However, this orientation is located in a narrow range between the unwanted illumination angles and cannot be recommended for FBG inscription.

The reflectivity distribution from the experimental results can be extended to a complete rotation of  $360^\circ$  due to the symmetry of the fiber design. Now, this reflectivity distribution can be compared to the intensity distribution achieved from the ray-tracing simulation. The agreement of simulation and the experimental result is shown in Figure 4.10).

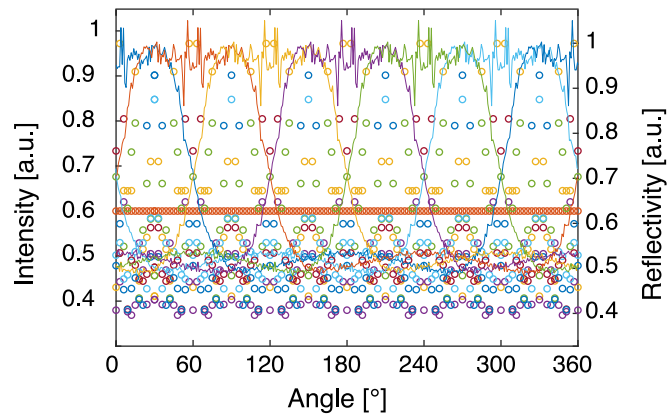


FIGURE 4.10: Experimental results of FBGs reflectivity are shown in circles and overlapped with the simulation results of intensity in different cores of multicore fiber shown in lines. Different colors represent different cores of the multicore optical fiber.

Generally there are two distinct levels that are visible for the experimental results. The points representing the gratings reflectivities follow the curves of the illumination intensities present in the cores obtained from the ray-tracing simulation. However, there are some gratings with reflectivities positioned outside the simulation lines. These cases can be explained by the complexity of the real experiment

compared to the simulation, e.g., the effects induced by absorption and diffraction in the cores.

## 4.4 Summary

In this chapter, a study of the FBG reflectivity depending on the illumination angle was presented. Multicore fibers will suffer from uneven illumination of the cores during the FBG inscription process. This will lead to the gratings with different reflectivities across fiber. Methods based on compensating the focusing effect of the cladding [183], or adjusting the photosensitivity of cores according to the illumination conditions [191] are often inapplicable for specific FBG inscription methods. Grating inscription performed on an optical table allows for rotating the fiber into a desired position. For the tested design of a seven-core fiber, the smallest reflectivity range for the different cores in the fiber was about 30%. However, there is no perfect orientation providing gratings with identical reflectivity. Nevertheless, using the measurement of the illumination angle would allow for avoiding critical orientations leading to a type II FBG formation or to local core destruction. Better results of FBGs reflectivity uniformity can be achieved through rearrangement of the cores in the cladding. One of such alternative arrangements is the eight core fiber described in Chapter 7.

## Chapter 5

# Multicore fibers calibration for curvature sensing

As discussed in Chapter 2, shape measurement is based on the interpretation of the strain along the fiber length as a combination of curvature, twist, and longitudinal strain effect. In the case of medical applications, of great importance is not only the general object shape but also the tracking of the sensor tip coordinates, which is sensible to the accumulated shape measurement error along the full sensor length. The reduction of these errors, based on applying different interpolation techniques for shape reconstruction using quasi-distributed sensors, has been shown in the literature [195–197]. In this chapter, in order to limit the effect of error propagation, a series of factors were examined. These include sensor geometry, photo-elastic coefficient, Bragg wavelength reference, and presence of twist that influence the accuracy in curvature sensing. A methodology for shape sensor calibration and characterization is presented with the results of an experimental study using multicore fibers with FBGs inscribed by an interferometric technique [198].

### 5.1 Shape sensor calibration in steps

Optical shape sensing with FBGs in multicore optical fibers relies on the measurement of the strain distribution across the fiber cross-sections, caused by a combination of elongation or compression, bend, and torsion (Figure 5.1). The approach of shape reconstruction determines the curvature along the sensing fiber based on strain measurements and calculates the shape through curvature interpolation and integration.

The strain distribution along a multicore fiber depends on the type of deformation that each cross-section is subjected to. Stretching generates a uniform increase in strain throughout the cross-section of the fiber. Torsion has no effect on the center of the fiber and reaches maximum strain on the fiber edges. Therefore, only outer cores are experiencing strain. Bending introduces a gradient of strain over the

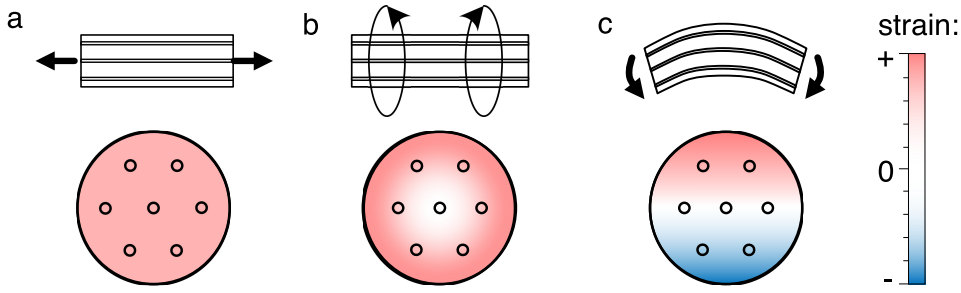


FIGURE 5.1: Strain distribution in stretched (a), twisted (b) and bent (c) multicore optical fiber.

cross-section with no strain on the neutral axis, perpendicular to the bend direction (Figure 5.2). Reconstructing this strain gradient in a multicore fiber and discriminating it from other types of deformation, using information from a combination of measurement points, is the main task of curvature and direction measurement along the sensing fiber length. The combination of reconstructed curvature values and curvature direction parameters allows performing a general shape measurement.

The local curvature  $\kappa$  of a bent multicore fiber, defined as the inverse local bending radius  $R$ , can be described mathematically at a certain position along the fiber as in Equation (2.6), previously shown in Chapter 2:

$$\kappa = \frac{2 \times \sqrt{\left(\sum_{i=1}^N \frac{\epsilon_i}{r_i} \cos \theta_i\right)^2 + \left(\sum_{i=1}^N \frac{\epsilon_i}{r_i} \sin \theta_i\right)^2}}{N} \quad (5.1)$$

Here,  $\epsilon_i$  and  $r_i$  are the curvature-caused strains measured in the single core  $i$  and the distance from the core  $i$  to the center of the fiber,  $N$  is the number of cores used for curvature calculation;  $\theta_i$  is the angle between one of axes of the coordinate system, which can be associated with core 1 relative to core  $i$  (Figure 5.2). For each grating of the longitudinal array, the curvature is an averaged value calculated by using the measured strain of  $N$  cores in the transversal FBG array. Therefore, the correct and efficient strain measurement in each core affects the overall curvature calculation.

With the calculated curvature, the local neutral axis of the bending and an angular distance to the neutral axis can be defined for each core. We can then calculate the bending angle  $\theta_{\text{bend}}$  between the neutral axis and the coordinate system associated with one of the cores, using strain information in the core nearest to the neutral axis:

$$\theta_{\text{bend}} = \arcsin\left(\frac{\epsilon_i}{r_i \kappa}\right) - \theta_i \quad (5.2)$$

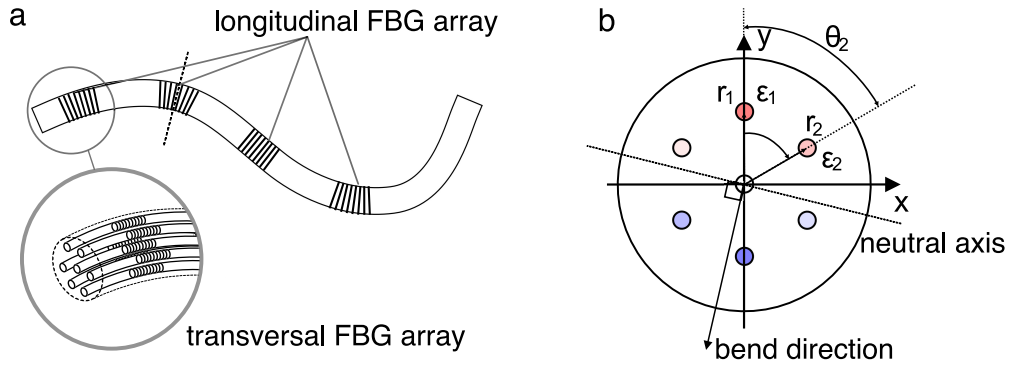


FIGURE 5.2: Schematic of a bent multicore fiber (a) with core orientations and radial distances and strains indicated for two cores (b).

Knowledge about the local curvatures and the bending orientation then allows reconstruction of the continuous shape along the fiber through interpolation methods.

Shape measurement using arrays of FBGs as a quasi-distributed sensor requires knowledge of several parameters, such as the fiber geometry, the gratings location, photo-elastic coefficient. Strain measurement based on FBGs is a method of measuring a fiber core elongation via a shift of the reflection peak wavelength for an inscribed FBG. For each core  $i$ , there is a relation between the local strain  $\epsilon$  and the measurable wavelength shift  $\Delta\lambda_B$  of the FBG reflection peak:

$$\epsilon = \frac{\lambda_m - \lambda_B}{\lambda_B (1 - \rho_e)} \quad (5.3)$$

with  $\lambda_B$  and  $\lambda_m$  being the initial and the measured strained wavelength peak position, respectively, and  $\rho_e$  being the photo-elastic coefficient that has to be measured once for a specific fiber. Local strain  $\epsilon$  is generally defined by a relative elongation  $\epsilon = \Delta L/L$ .

Therefore, for reconstructing a specific curvature, the wavelengths of Bragg reflection peaks  $\lambda_m$  for each grating have to be measured, and a number of other parameters such as  $\theta_i$ ,  $r_i$ ,  $\lambda_B$ ,  $\rho_e$  have to be known from characterization or calibration measurements [199]. Some of these parameters can be measured directly, and others are derived indirectly by a calibration procedure. In the following sections, the procedures for determining these parameters will be discussed. The improvements in curvature measurement accuracy will be demonstrated for a test object. Since the general curvature reconstruction is based on differential measurements, the exact knowledge of these parameters is of great interest in order to limit possible error accumulation along the length of the fiber sensor.

### 5.1.1 Fiber geometry

Several multicore fibers have been reported in the literature for application in shape sensing [200]. Using each particular fiber for shape sensing requires knowledge about its geometry – such as the number of cores  $N$ , the information about cores location described via core-to-center distance  $r_i$ , and the angle  $\theta_i$ . This information can be obtained from a datasheet or a microscope cross-section image. A previously used in Chapter 3 seven-core fiber was used for this study. The geometrical parameters were derived from a microscopic image shown in the Figure 5.3. This fiber has enhanced photosensitivity and low cross-talk between the cores due to a high  $\text{GeO}_2$  concentration (above 20 mol%) in the cores.

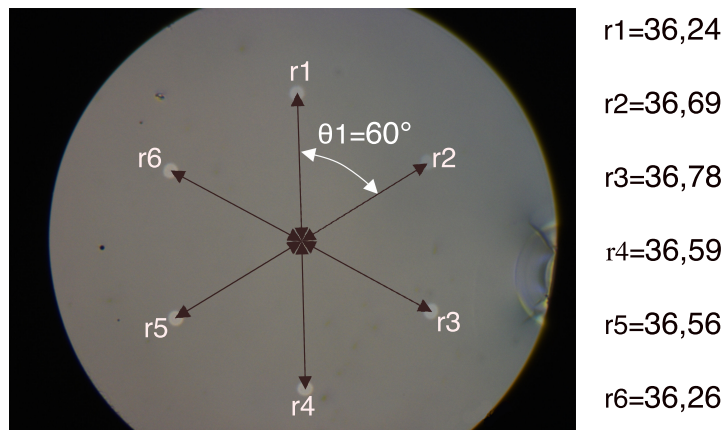


FIGURE 5.3: Microscope image of an experimental seven-core fiber, with geometrical parameters.

Besides the specific values of the core-to-center distances (also called core spacing), the knowledge of relative variations (the ratio of core distance relative to the average distance) would be an essential parameter for the reconstruction algorithm. In our case, the core-to-center distances for the position shown are in a range of  $36.24 \mu\text{m}$  to  $36.78 \mu\text{m}$ . Due to only minor variation, often, one single averaged value of the core-to-center distance is used for the reconstruction. However, a variation of such core-to-center distances may also occur along the fiber as discussed in section 5.1.2. Three outer cores and a central core were used for the experimental study of the calibration procedure. As discussed in Chapter 2, four cores are sufficient for a shape measurement. In case of the shown seven-core fiber, other cores are arranged with a mirrored symmetry and, therefore, will not increase the measurement accuracy.



### 5.1.2 Photo-elastic coefficient

The photo-elastic coefficient ( $\rho_e$ ) describes the strength of the change of optical properties of the material under mechanical deformation. As applied to an optical fiber, this parameter defines the effective refractive index change in response to a physical fiber deformation. For such a case, a single characterization or calibration measurement of a single measured photo-elastic coefficient  $\rho_m$  (e.g., in the central core) would be sufficient to determine this parameter. However, it has to be considered that the multicore fiber manufacturing process might introduce individual modifications of the different fiber cores and variations of the structural parameters, e.g., fiber and core diameters or material/doping distributions. Such variations can be considered as an additional correction factor  $\alpha_i$ , measured experimentally during a calibration procedure, which would have to be included in the curvature calculation algorithm (Equation (5.4)). In the case of strain gauges based on FBGs, this coefficient also defines the shift of reflection peak wavelength.

$$\Delta\lambda_B = \lambda_B (1 - \rho_m \alpha_i) \epsilon \quad (5.4)$$

A setup that can stretch the fiber and associate the elongation with the peak wavelength shift is shown in Figure 5.4.

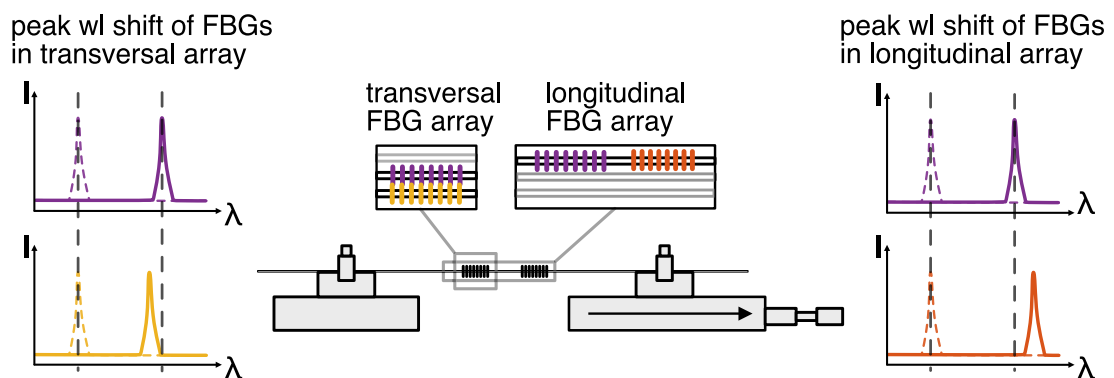


FIGURE 5.4: Setup for photo-elastic ( $\rho_e$ ) and correction coefficient ( $\alpha_i$ ) measurement. Peak wl - peak wavelength.

The photo-elastic coefficient  $\rho_e$  and correction coefficients  $\alpha_i$  are responsible for an adequate conversion of the measured wavelength shift data into strain, which is later used for curvature calculation. In order to measure the variation of the photo-elastic coefficients in different cores and along the fiber, the fiber was pulled to track the wavelength shift of the FBG in the array in the central and three outer cores of the fiber. The measured wavelength shifts in the cores are shown in Figure 5.5.

As can be seen from Figure 5.5, a peak wavelength shift difference of 9 pm on average was detected for the fiber cores. This will define  $\alpha_i$  coefficients in the range

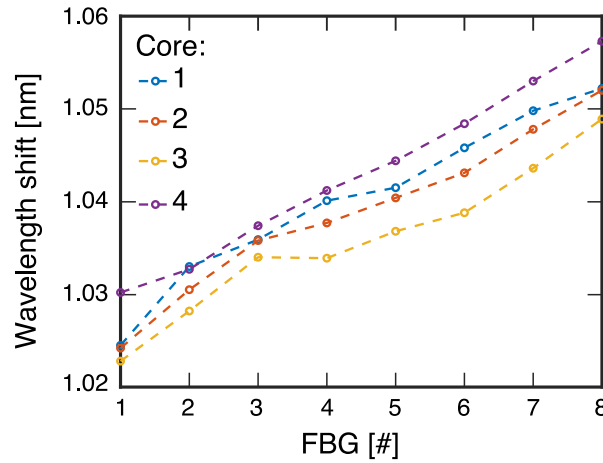


FIGURE 5.5: Wavelength shift in an array of FBGs in the stretched fiber.

of 0.9819 to 1.0054. Moreover, the shift is growing over the sensor length for each core by about 27 pm. This means that the stretched fiber has a non-uniform strain along the sensing length due to a varying fiber diameter, which can be measured and compensated via correction factors  $\gamma_j$  (0.9913 to 1.0125), interpreted as a change of the fiber diameter for each FBG of the longitudinal array and, hence, the core-to-center distance  $r_i$ . The final equation used for the curvature calculation in the  $j$ -th grating via the strain measured in  $N$  cores and considering the correction factors is:

$$\kappa_j = \frac{2 \times \sqrt{\left( \sum_{i=1}^N \frac{\epsilon_{i,j}}{r_i \gamma_j} \cos \theta_i \right)^2 + \left( \sum_{i=1}^N \frac{\epsilon_i}{r_i \gamma_j} \sin \theta_i \right)^2}}{N} \quad (5.5)$$

### 5.1.3 Initial fiber Bragg gratings reflection peak wavelengths

For the measurement of wavelength shifts, the knowledge of the exact starting conditions is mandatory. In general, the measurement of initial reflection peak centers is a standard procedure. For high accuracy, it should be considered that this measurement would be temperature-sensitive and that any additional strain due to bend, twist, or axial load during the characterization procedure should be avoided. Clamping optical fibers on both sides can cause twist and bend in the fiber. It is also difficult to set the fiber in a straight condition horizontally without strong stretching due to the gravity effect on the fiber. Therefore, a setup with the fiber clamped on one side is favorable. (Figure 5.6). The fiber is suspended vertically in this case and, to straighten the fiber, a load of a few grams can be fixed at the end of the fiber. This load leads to a wavelength shift of the reflection peaks from the initial position in a small range but ensures to avoid the strain hysteresis caused by the coating. However, the effect of the additional negative strain during calibration can be considered and corrected later in the measurement data processing.

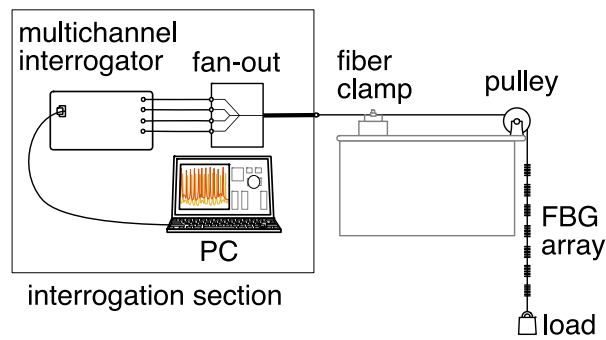


FIGURE 5.6: Setup for initial FBG reflection peak wavelength measurement.

This method with an additional load helps the fiber to take its natural shape and prevents any additional torsion and curvature.

The spectra shown in Figure 5.7 were measured for gratings simultaneously recorded by a single laser pulse in seven cores of a multicore fiber without specific orientation consideration. Reflectivity measurements were performed using Fresnel reflection from the cleaved fiber end facet as a reference.

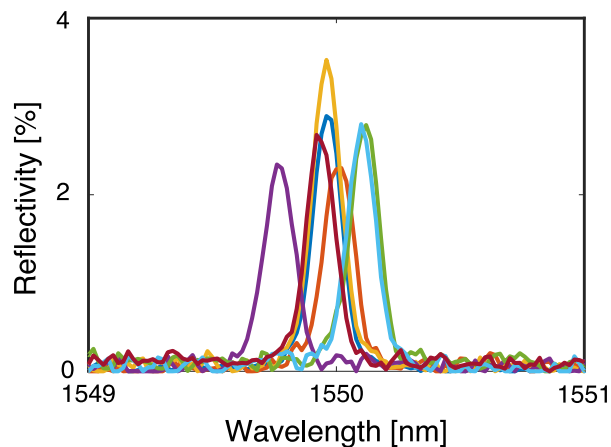


FIGURE 5.7: Spectra of FBGs recorded in seven cores of a multicore fiber.

There are obvious differences in peak position and reflection peak strength. The wavelength in this case varies between 1549.77 and 1550.12 nm, and the reflectivity varies between 2.3 and 3.5%. These variations can be attributed to differences in the effective refractive index of different cores and to variations of the grating modulation depth due to lensing and shadowing effects produced during the inscription of gratings in a multicore optical fiber.

#### 5.1.4 Intrinsic twist measurement

Intrinsic twist issue has been discussed in detail in Chapter 3. In a shape measurement procedure, intrinsic twist cannot be directly discriminated from an experimentally measured twist. Hence, a fiber curved in a plane would then seem to have a

helical shape in the reconstruction of the measured shape. Since it is hard to control or reduce intrinsic twist, the shape sensor fiber must be calibrated to reduce a shape error induced by an intrinsic twist. It may also happen that the fiber is intentionally twisted during the manufacturing process. Also, in this case, the twist has to be well characterized.

For the intrinsic twist characterization, two different methods are suggested. With the first method, the inner structure of the fiber is observed in a diffraction projection pattern from a side-illuminated fiber. Applying this procedure requires installing the fiber without adding a twist by handling the fiber. This can be achieved by hanging the loaded fiber vertically clamped on top and then, after taking its natural shape, clamping the fiber end at the bottom. Then the fiber can be used for observation of its diffraction pattern through one complete rotation (Figure 5.8a) and by scanning along its longitudinal axis (Figure 5.8b).

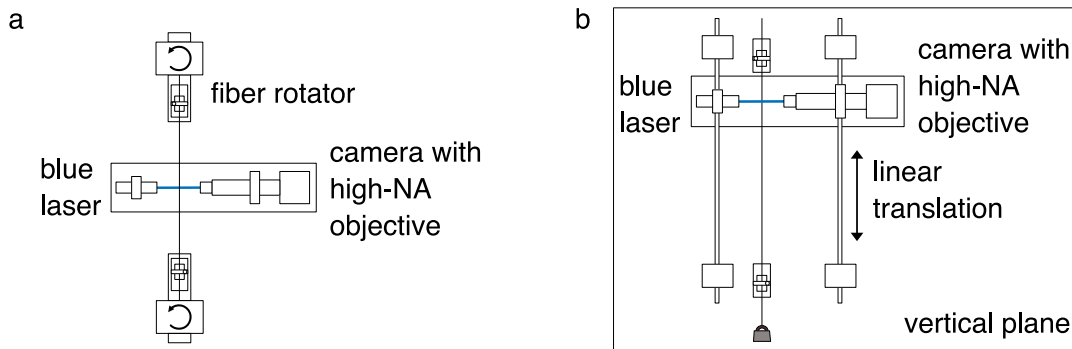


FIGURE 5.8: Setups for intrinsic twist measurement using side laser illumination for fiber rotation (a) and fiber scanning (b).

In this setup, plane wave laser light passes through the fiber and is diffracted and focused by the refractive and diffractive core structures. This light pattern is collected by an objective with a high numerical aperture and projected into a camera. Dark areas in such recorded patterns are typically caused by the fiber cores. The current angular orientation of the fiber therefore detectable. Moving the illumination laser and the camera along the fiber enables recording the diffraction patterns for all positions of the sensor (Figure 5.9a) and comparing it with the reference patterns recorded for all possible orientations, i.e., for a complete rotation (Figure 5.9b).

An analysis of these patterns allows quantification of the rotation angle of the cores in a given sensor length, which corresponds to the intrinsic twist of the fiber. The scanned pattern of 20 mm of fiber in our case shows the same pattern as a multicore fiber rotation from  $131^\circ$  to  $134^\circ$ , which corresponds to the twist of  $1.5^\circ/\text{cm}$  to  $2^\circ/\text{cm}$ . This method does not require Bragg gratings to be inscribed in the cores and can be applied before FBG inscription. In this particular case, the measurement accuracy does not exceed  $1\text{-}2^\circ/\text{cm}$ , since extracting the angle from the diffraction

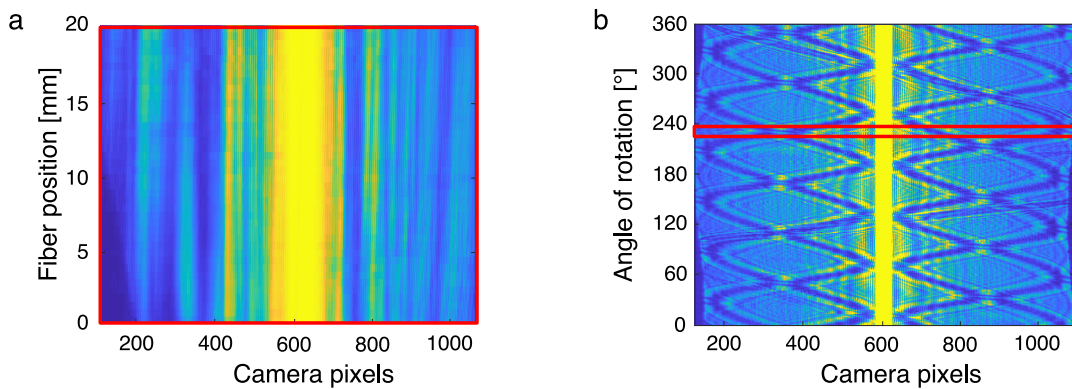


FIGURE 5.9: Pattern formed by a stack of images obtained by: a) - scanning a length of 20 mm. b) - one complete rotation of the seven-core fiber.

pattern is limited due to minor orientation change along the scanning length applied. The accuracy of this method can be improved by employing the Pearson coefficient based measurement of an orientation angle.

Such distinct pattern structures can be observed with a periodicity corresponding to the fiber symmetry ( $60^\circ$  in our case). Therefore, observing such distinct pattern structures twice during the fiber scanning can reveal an internal fiber torsion of  $60^\circ$  between the points where the patterns were detected. Since an angle of  $60^\circ$  is a rather large value of twist for a fiber, scanning of longer pieces of a fiber might be necessary in this case: higher twist values are better to investigate and more easily detectable. Such a measurement can be achieved especially with fibers with a designed twist of, e.g., 50 rotations per meter since the shorter twist period, in this case, allows the scanning length to be reduced and the twist period is then measured with sub-millimeter accuracy.

The second method for twist measurement can be based on the shape measurement procedure of a known flat test shape structure applied with the same interrogation scheme as the one used for the general shape measurement. In this specific case, the measurement fiber is positioned in a curved shape on a flat plane surface (Figure 5.10a). The bending radius must be small enough to ensure that the wavelength shift of the reflection peaks of FBGs in the cores caused by the bend is larger than the possible noise level accuracy of the spectral measurement system. An intrinsic twist of the fiber will result in a reconstructed helical shape in the reconstructed fiber position beyond the actual plane surface in the test setup (Figure 5.10b) since, due to twist, a non-zero value of torsion will be detected.

The intrinsic twist is measured as the change of the angle between the neutral axis and one of the cores for two different gratings along the longitudinal array. In our case, the measurement was performed several times to ensure measurement repeatability and achieved a rotation of  $12.3^\circ$  on a length of 72 mm between the

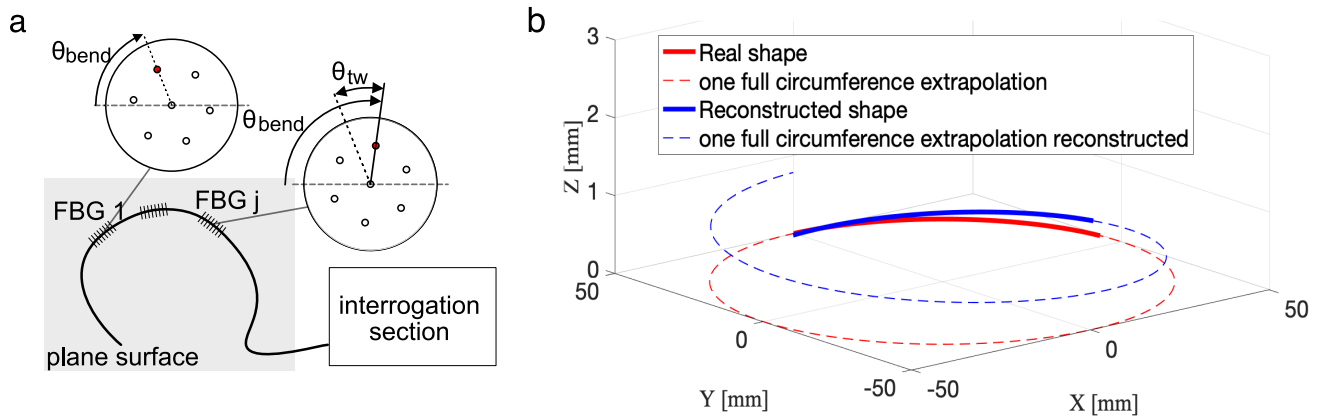


FIGURE 5.10: a) -Setup for the intrinsic twist measurement. b) - Shape reconstruction and real shape comparison for a twisted fiber.

centers of the first and the last gratings, which corresponds to an intrinsic twist of  $1.71^\circ/\text{cm}$ . This value will be used to correct the shape measurement for the intrinsic twist as a coordinate system rotation and will be subtracted from the bending angles measured. This second intrinsic twist measurement method is simple and does not require additional equipment. It can be applied using the same interrogation system as that used for the shape measurement. The accuracy of the twist measurement achieves an accuracy below  $1^\circ$  and therefore fits better to multicore fibers with a low intrinsic twist.

## 5.2 Evaluation of calibration corrections with a test object

The impact of the discussed calibration corrections will now be shown for curvature measurements with a test object. A multicore fiber with four cores, eight FBGs in each core and with a total length of 72 mm was used for testing of the impact of the calibration procedures on the measurement accuracy. For defining a specific shape, a plane mold with a set of grooves of different diameters representing shapes of different curvatures was used. The sensing fiber was then installed in the grooves with a defined curvature without clamping or gluing (Figure 5.11)a.

The fiber was positioned in this plane mold with curvature radii  $R_{groove}$  40, 50, 60, and 70 mm so that all grating positions would experience the same bending with a radius,  $R_{fiber}$ , that is slightly smaller than the outer radius of the groove,  $R_{groove}$ , for half the diameter of the fiber (Figure 5.11b). Then the curvature can be calculated using Equation (5.1). In Figure 5.12, the measured curvature values are presented for the fiber positioned in the aluminum mold.

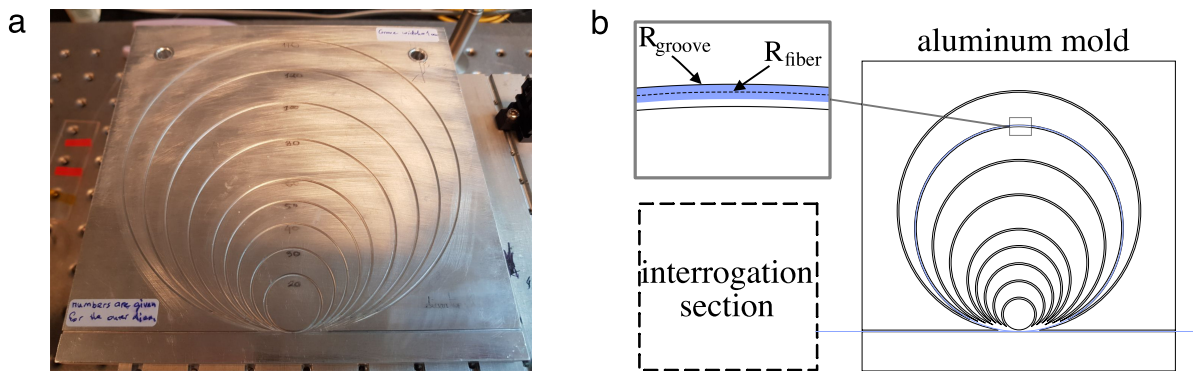


FIGURE 5.11: Setup for positioning a sensing fiber in a plane test shape with fixed radii of curvature (a) and a photograph of the aluminium mould (b).

Figure 5.12a shows different reconstructed radii of curvature for eight grating positions along the fiber length without the use of the correction factors from calibration. Here, rectangles correspond to the time-averaged value of the radius of curvature as measured during a 3-minutes experiment. The bars indicate the range variation of 360 single measurements acquired with a frequency of 2 Hz. The theoretical curvature of the center of the fiber,  $R_{fiber}$ , is shown as a black horizontal line. It is interesting to note that the variations in the single measurements are higher for larger curvature radii. The reason is that the reflection peak wavelength measurement error is affecting the fiber more strongly when it is bent with a larger radius, as it is subjected to lower strain and shows a lower peak wavelength shift in the cores. As a next step, the correction factors  $\alpha$  were applied as shown in Figure fig:corb. In this case, the averaged relative error for all experiments slightly decreased from 0.89 % to 0.88 %. This minor change of accuracy indicates that the variation of photo-elastic coefficient along the fiber is not high in our case and does not induce large additional errors for the curvature measurement. For the results in Figure 5.12c, the correction factors of  $\gamma$  were applied in addition. In this case, the averaged error for the experiments decreased to 0.5 %. For FBG 1, which showed the most prominent errors, the maximum observed error was almost halved, decreasing from 2.48 % to 1.37 %. This improvement indicates that the fiber diameter in our case may have varied along the fiber length leading to a core-to-core distance change in a range of 35.9  $\mu\text{m}$  to 36.8  $\mu\text{m}$ .

Hence, the calibration procedure enables us to increase the accuracy in curvature sensing remarkably. The measurement of the photo-elastic coefficients (as material parameters) for the individual cores had a relatively low impact on accuracy in our case because of low differences. However, this procedure should still be applied generally since photo-elastic coefficient differences are hard to predict for complex fibers. Using multicore fibers with a designed twist leads to different wavelength

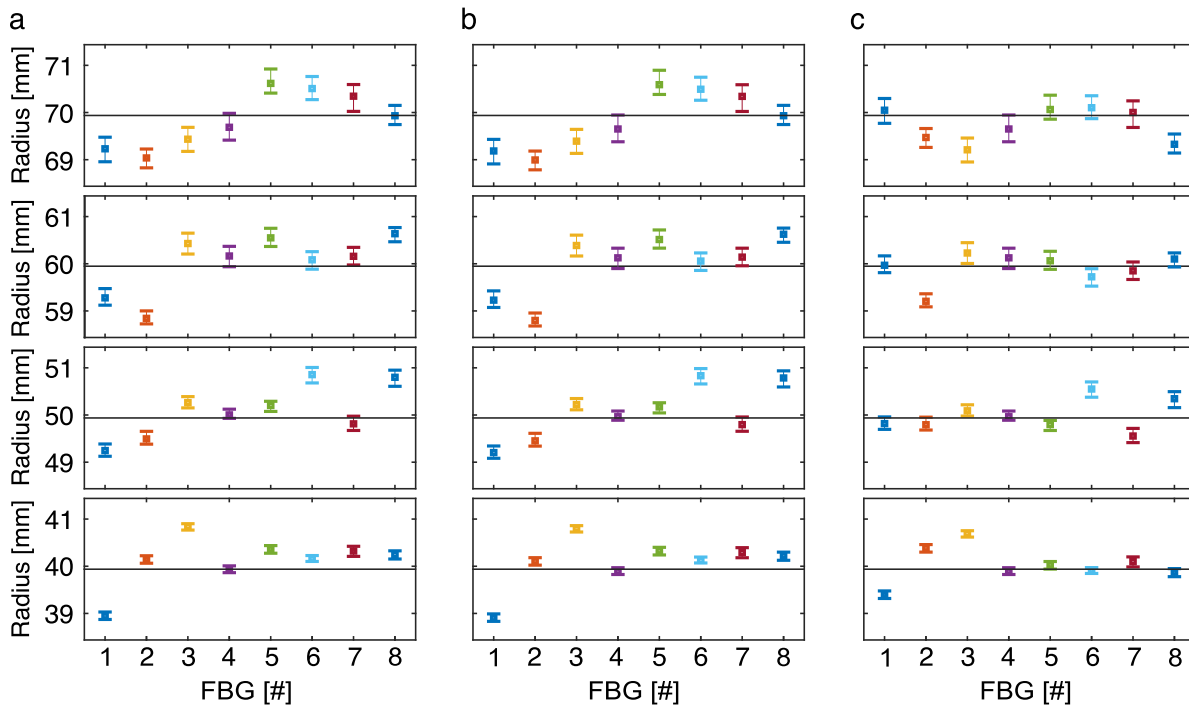


FIGURE 5.12: Shape measurement of the grooves on the mould with no correction (a), with  $\alpha_0$  (b) and additional  $\gamma$  (c) correction factors applied. The horizontal line in the center of each graph indicates the ground truth for the radius measurement.

shift-to-strain conversion factors for the helically twisted side cores and the straight central core and the  $\alpha$  factor can be used to take these conversion differences into account. The same calibration procedure can be applied to check for local fiber diameter variations. In this case, one can identify fiber imperfections that are hard to check otherwise and which have been shown to substantially impact reconstruction accuracy. The calibration of the correction factors  $\alpha$  and  $\gamma$  can be implemented with setups very similar to those for the initial reflection peak wavelengths measurement by means of measuring the wavelength shifts of reflection peaks in each individual FBG in the longitudinal and transversal arrays. The observed twist of  $12.3^\circ$  measured along a length of 17 cm is considerably large value for a fiber with no designed twist. This intrinsic twist information is important for the overall accuracy of the sensor when reconstructing a complete 3D shape by a combination of curvature magnitude and curvature direction data.

### 5.3 Summary

Calibration procedures for shape sensing with multicore optical fibers and inscribed FBGs have been shown and discussed. The proposed procedures allow for considering the sensitivity of each FBG individually by elaborating the effective photo-elastic



---

coefficient for every single core and adjusting the strain conversion coefficient in the transversal array of the fiber gratings. Calibration includes a measurement of the intrinsic twist of multicore fibers that can be introduced during the manufacturing process, whether by chance or intentionally. Overall, the maximum error of measuring curvature and the averaged relative error has been shown to be reduced by almost a factor of 2 in a test setup with curvature radii in a range between 40 to 70 mm for the used fiber. These results show the high importance of well-adapted calibration procedures in shape sensing using optical fibers. The effect can be more prominent for the fibers with more substantial deviations in core-to-center distances and more significant differences in photo-elastic coefficient across and along the fiber sensor.



## Chapter 6

# Multiplexing of FBGs in multicore fibers using the inverse bend sensitivity

Multicore optical fibers are a promising solution to the task of developing new multiplexing methods. Space-division multiplexing can be used in multicore optical fibers to increase the transmission capacity of telecommunication optical fibers or enable new types of sensing for the optical fiber sensors. The need for special equipment was already discussed in Chapter 2. One of the essential components allowing for addressing the cores of a multicore fiber individually is the optical fanout. Optical fanouts are complex devices and need special equipment to be made (see Section 2.3.2). Additionally, the fanouts have to be optimized for a specific multicore fiber design.

Optical fiber sensors based on multicore fiber and FBGs often require a fanout for the individual interrogation of the gratings inscribed in a single plane (Figure 6.1a). This is required due to overlap of the FBGs reflection peaks in the spectral domain, as shown in Figure 6.1b. Some methods, such as sinusoidal spectral shape [201], strong coupling [202] or focused femtosecond point-by-point inscription [203], have been suggested for multicore fibers interrogation simplicity.

Usually, shape sensors using FBGs in optical fibers are inscribed in a linear condition. Then, while the fiber is bent, the reflection peaks of gratings in different cores are separated in the spectral domain, as shown in Figures 6.1c and 6.1d).

Considering this effect, in this chapter, a simple approach for wavelength multiplexing and interrogation of FBGs in a multicore fiber using grating inscription under a pre-bent condition is presented. This approach takes advantage of the inverse bend sensitivity of multicore fibers and suggests inscribing FBGs in a curved fiber to separate the spectral peaks for the linear fiber. It can be beneficial for simple sensors based on multicore fibers, and FBGs, e.g., for fiber optic inclinometers or directional bending sensors [204].

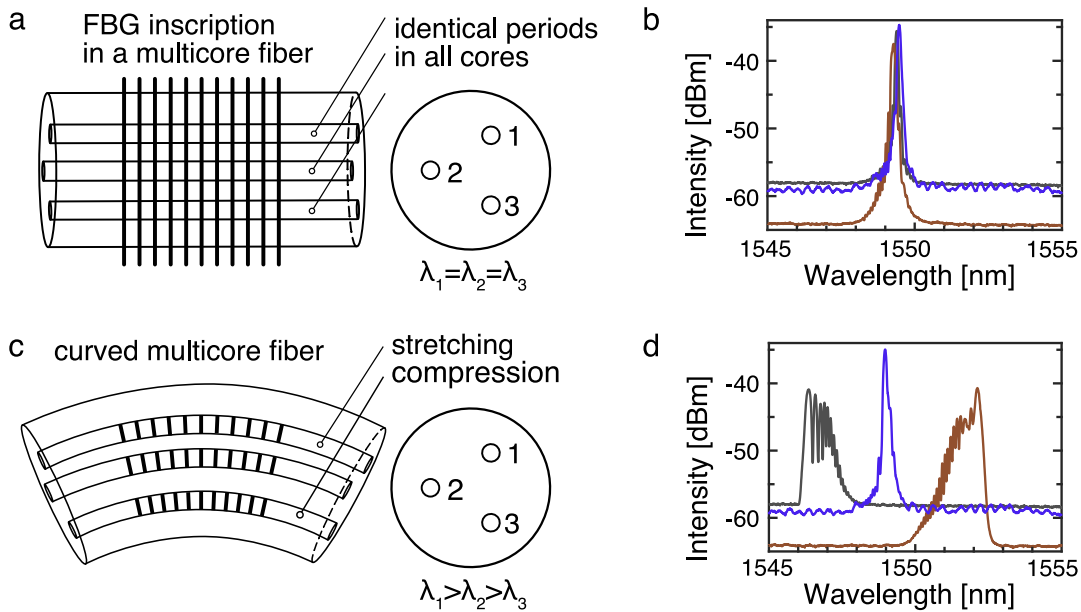


FIGURE 6.1: a)-Conventional FBG inscription. b)-FBG spectrum in multicore fiber.

## 6.1 Concept of the inverse bend sensitivity

The conventional FBG inscription methods, such as phase mask inscription or interferometric method, applied to multicore fibers usually obtain gratings with identical reflection wavelengths. Minor shifts of the central reflection wavelengths are caused by the different levels of the average refractive index modulation in different cores (see Chapter 4). However, this minor variation in the reflection wavelengths is insufficient to discriminate the peaks reflected from different cores in the spectral domain.

The concept of the inverse bend sensitivity for FBG inscription suggests pre-bending the multicore fiber and, therefore, creating different deformation conditions for different cores. Hence, the inscribed FBGs will have closely located reflection wavelengths but in a deformed condition. After the fiber is relaxed, the separation of the gratings spectra in different cores is achieved. The multicore fiber can then be used as a sensor without the necessity of a spatial discrimination of the cores, as shown in Figure 6.2.

A multicore fiber sensor prepared using this method can be interrogated by a single channel.

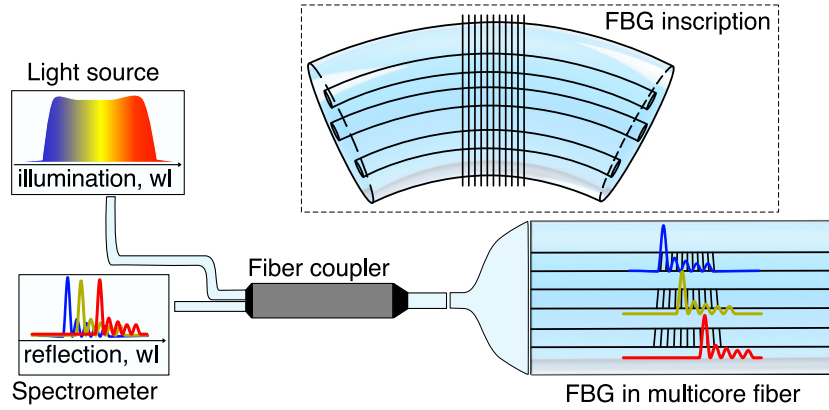


FIGURE 6.2: FBG inscription in a pre-bent fiber inscribed and single-channel interrogation of multiple FBGs.

### 6.1.1 Comparison of the FBG inscription in a linear and curved fiber

The multicore fiber with FBG inscribed using the presented method can be used as an omnidirectional shape sensor. The measurement range, in this case, would be limited by an overlap of the reflection peaks in the spectral domain due to ambiguity created by the overlapped peaks. However, this overlap will be reached only by curving the fiber in the same direction as used for the FBG inscription, and with a smaller bending radius. To explain the reason for that, the inscription in a bent fiber must be compared to the inscription in a straight fiber.

#### The case of an FBG inscription in a linear multicore fiber

Let us assume first the conventional FBG inscription in a linear multicore fiber with three identical cores, as shown in Figure 6.3a.

Since the cores are identical, the FBGs inscribed in all three cores will have identical periods  $\Lambda_0$ . All three cores will also have the same effective refractive index  $n_0$ . Thus, the central peaks of the reflection wavelength of the gratings  $\lambda$ , in this case, can be calculated as:

$$\begin{aligned}\lambda_{\text{core1}} &= 2n_0\Lambda_0 \\ \lambda_{\text{core2}} &= 2n_0\Lambda_0 \\ \lambda_{\text{core3}} &= 2n_0\Lambda_0\end{aligned}\tag{6.1}$$

The bending applied to the multicore fiber with a radius  $R$ , as shown in Figure 6.3b, will cause changes in both the effective refractive index and the grating period in Cores 1 and 3. Since the cores are equally distant from the neutral axis,

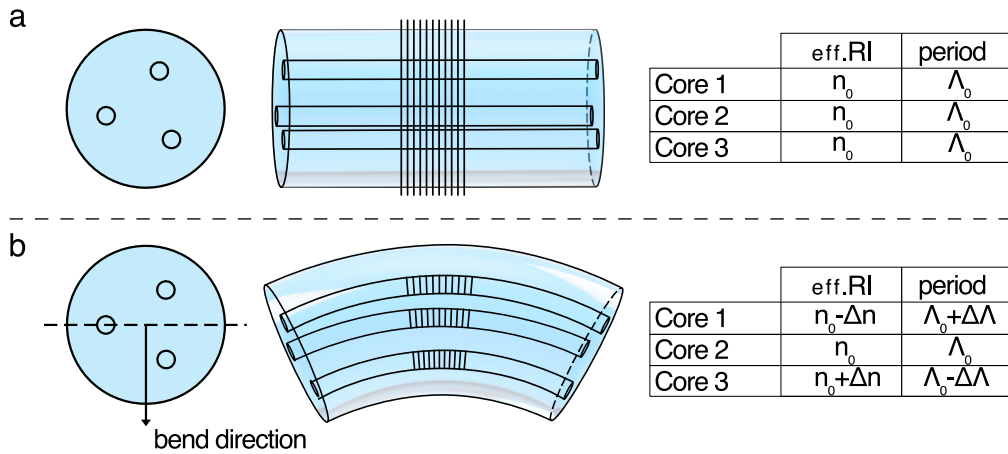


FIGURE 6.3: Effective refractive indices and grating periods in a multicore fiber core fiber in a linear and curved state. (a) - FBG inscription in a linear state, the gratings in all cores have identical reflection peak wavelength due to a matching effective refractive index and period. (b) - Fiber is curved after FBG inscription. Both the effective refractive index and the period change in the cores 1 and 3.

the effective refractive index is expected to change by the same absolute value of  $\Delta n$ , and the period will also change identically by the absolute value of  $\Delta \Lambda$ . This will lead to a shift of the reflection peaks of the FBGs  $\lambda^b$  in the Cores 1 and 3, as:

$$\begin{aligned}
 \lambda_{\text{core1}}^b &= 2(n_0 - \Delta n)(\Lambda_0 + \Delta \Lambda) \\
 \lambda_{\text{core2}}^b &= 2n_0\Lambda_0 \\
 \lambda_{\text{core3}}^b &= 2(n_0 + \Delta n)(\Lambda_0 - \Delta \Lambda)
 \end{aligned} \tag{6.2}$$

The shift of the central wavelength of the grating in the Core 1 towards the longer wavelengths, due to the increased period  $\Lambda + \Delta \Lambda$ , will be partially compensated by the decreased effective refractive index  $n_0 - \Delta n_0$  for the Core 1, and vice versa for the Core 3. Core 2 is located on a neutral axis of bending, therefore, no wavelength shift is expected for this core.

### The case of an FBG inscription in a curved multicore fiber

We can now consider the case with a bent fiber FBG inscription and compare it to the previous one. For the gratings inscription, the fiber is bent with a radius of  $R$  in the identical direction, as shown in Figure 6.4a.

The grating periods  $\Lambda$  in all cores will be identical. Since the fiber is pre-strained, the cores will have a varying effective refractive index with negative change for Core 1 and positive change for Core 3. The effective refractive index in the central core is expected to be unchanged as the core is located on the neutral axis, where the stress

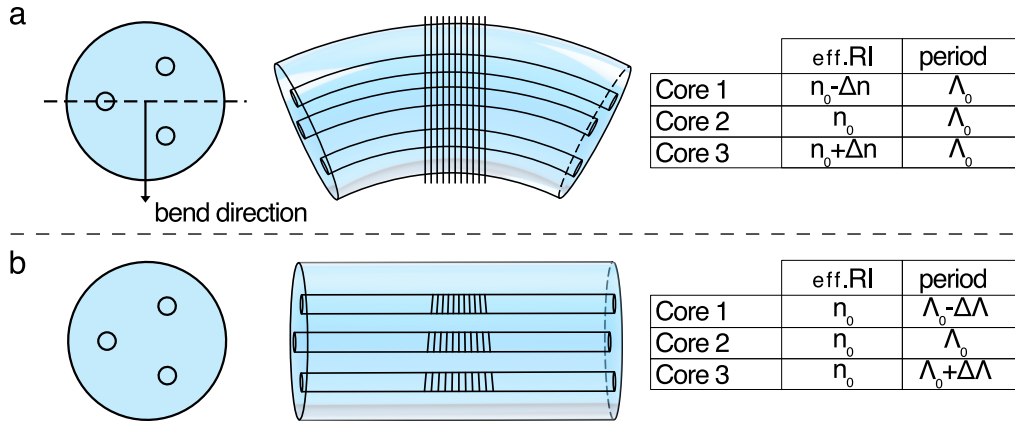


FIGURE 6.4: Effective refractive index and grating periods in a multicore fiber in a linear and curved state. a) - FBG inscription in a curved state, the gratings in all cores have different reflection peak wavelengths due to varying effective refractive index. b) - Spectral separation of the reflection peaks for the straightened fiber is increased due to the stronger effect of the period change. Effective refractive indices are identical.

equals zero. At this bent condition, the central reflection wavelengths are expected to be as:

$$\begin{aligned}
 \lambda_{\text{core1}}^* &= 2(n_0 - \Delta n)\Lambda_0 \\
 \lambda_{\text{core2}}^* &= 2n_0\Lambda_0 \\
 \lambda_{\text{core3}}^* &= 2(n_0 + \Delta n)\Lambda_0
 \end{aligned} \tag{6.3}$$

The reflection peaks from the stretched Core 1 on top will be shifted towards shorter wavelengths from the central core reflection peak, and the reflection peaks in the Core 3 in the bottom will be shifted towards longer wavelengths.

Then relaxation of the fiber into the linear state will result in equalizing the effective refractive indices in the cores.

The peaks shifted to the shorter and longer wavelength will move further in the same direction since the contribution of period change is stronger than the change in the effective refractive index. Thus, the reflection wavelengths of gratings are expected to as:

$$\begin{aligned}
 \lambda_{\text{core1}} &= 2n_0(\Lambda_0 - \Delta\Lambda) \\
 \lambda_{\text{core2}} &= 2n_0\Lambda_0 \\
 \lambda_{\text{core3}} &= 2n_0(\Lambda_0 + \Delta\Lambda)
 \end{aligned} \tag{6.4}$$

Then an optical multicore fiber with inscribed gratings with different reflection wavelengths is obtained. In the case of using such fiber for shape sensing, bending

in the opposite direction to the bend direction shown in Figure 6.4, will further increase the spectral distance between the reflection peaks. Bending the fiber in the same direction might cause an overlap of the peaks. However, this state can be reached only in the case of a stronger bending. If the fiber is bent with the same radius of  $R$  (as for the FBG inscription), the peaks will still be separated and the reflection wavelengths in the cores will be equal to  $\lambda_{\text{core1}}^*, \lambda_{\text{core2}}^*, \lambda_{\text{core3}}^*$  for the cores 1, 2, and 3 respectively.

For the inscription in bent multicore fiber, there is a limitation for the bending in the same direction as was used for the FBG inscription. The limitation extends beyond the radius that was used for gratings inscription due to initial peaks offset, which can overlap only via stronger bending in the same direction. Such bending sensor can be used without channels separation for interrogation with a limited range of bending in one direction.

## 6.2 Method for the multiplexed FBGs inscription

Multiplexed fiber Bragg gratings in multicore fiber using the presented method are made in a few steps. The fiber must be bent in a specific direction for the best performance and for equal spectral distance between the FBGs in different cores. In the case of a three-core fiber with identical core-to-center distances, the bending direction must be selected to place one of the cores on the neutral axis of bending. In the case of multicore fiber with identical cores, it will mean that projections of the core positions onto the curvature plane should be equidistant. The appropriate curvature direction can be ensured by using the orientation measurement setup described in Chapter 3.

The fiber must be installed with a possibility of orientation adjustment (Figure 6.5a). If the fiber is bent vertically, the fiber is rotated to the position where the cores are equidistant on the vertical projection, as shown in Figure 6.5b. Then the fiber can be bent in a vertical plane, and the FBGs can be inscribed (Figure 6.5c). After FBG inscription, the reflection peaks will be separated in the spectrum due to the strain-induced refractive index differences in the cores. After releasing the clamps and relaxation of the fiber to a linear position, the separation of the peaks will be further increased.

In general, a wavelength offset  $\Delta\lambda_B$  of the FBG reflection peaks can be achieved by applying strain  $\epsilon$  to a fiber as:

$$\Delta\lambda_B = \epsilon (1 - \rho_e) \lambda_B \quad (6.5)$$



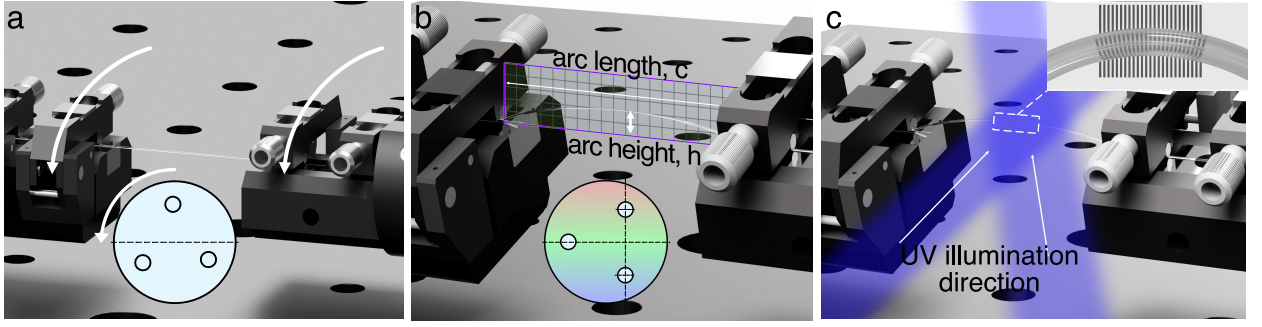


FIGURE 6.5: Step-by-step FBG inscription process using a curved optical fiber. (a) - Multicore fiber is installed in clamps and rotated to the required position. (b) - Fiber is bent in vertical plane for the desired radius by shifting the holders. (c) - FBGs are inscribed.

Here,  $\lambda_B$  is the central reflection wavelength of an FBG achieved in a relaxed condition, and  $\rho_e$  is the photo-elastic coefficient.

The strain in the bent fiber is related to the curvature  $\kappa_c$  (inverse of the bending radius) as described in Equation 2.6 in Chapter 2.

For the case of a symmetric three-core fiber as depicted in Figure 6.5 b and assuming that the photo-elastic coefficient difference in the cores is negligible, the achieved wavelength shift  $\Delta\lambda_B$  can be simplified from Equations 2.6 and 6.5 to:

$$\Delta\lambda_B = \frac{3r}{4R} \times \frac{\lambda_B(1 - \rho_e)}{\sin(60^\circ)} = 0.87 \frac{r(1 - \rho_e)\lambda_B}{R} \quad (6.6)$$

Where  $r$  is the core distance from the fiber center and  $R$  is the bending radius. The applied bending radius of the fiber in the inscription setup can be derived from the observed arc length  $c$  and the arc height  $h$  (see Figure 6.5b):

$$R_m = \frac{c^2 + 4h^2}{8h} \quad (6.7)$$

### 6.3 Experimental proof of principle

As a proof of principle of the presented concept, a seven-core fiber was used with three cores selected to simulate a more simple three-core fiber (Figure 6.6).

In Figure 6.7 examples for applied bending on multiplexed FBG spectra are shown. The cores were addressed using a fanout spliced to multicore fiber. The equal distancing of the reflection peaks in a spectral domain allows for the maximum achievable measurement range limited by the possible overlap of the peaks.

As mentioned before, even in the bent position, the gratings already show a wavelength shift for the different radial positions with peaks maxima at 1548.32,

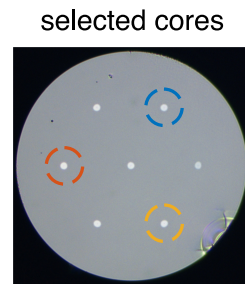


FIGURE 6.6: Multicore fiber used for a proof-of-principle.

1550.52, and 1553.07 nm (see Figure 6.7b). This wavelength shift increases when the fiber is relaxed to a linear position with peaks maxima shifting to 1546.53, 1550.59, and 1554.92 nm, respectively (Figure 6.7a). The overlap of the reflection peaks in the cores is achieved by bending the fiber in the same direction with a smaller radius of curvature (Figure 6.7c).

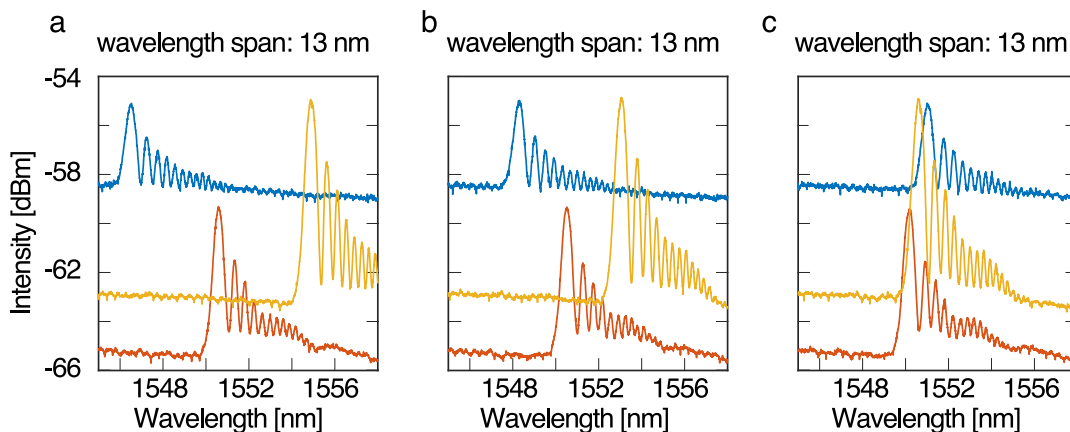


FIGURE 6.7: a) - FBGs spectra in a relaxed optical fiber. b) - Spectra of the FBGs while fiber is bent in the same direction and strength as during FBG inscription. c) - Overlap of the FBGs reflection peaks due to stronger bending.

There is a direct correlation between the multicore fiber curvature for FBG inscription and the spectral distance between the peaks. However, a stronger bending will reduce the effective length of the grating, thus decrease the reflectivity. In addition to a weaker reflectivity, a stronger bending will introduce more prominent side lobes on the longer wavelengths side of the spectrum. In Figure 6.8, the spectra of the FBGs inscribed with weak and strong bends are compared.

As seen in Figure 6.8b, the reflection peak spectrum in each core is distributed over a few nanometers, whereas the spectra of gratings inscribed under weaker bending conditions have a shorter spectral decay, and thus are easier for a peak-fitting algorithm to analyze.

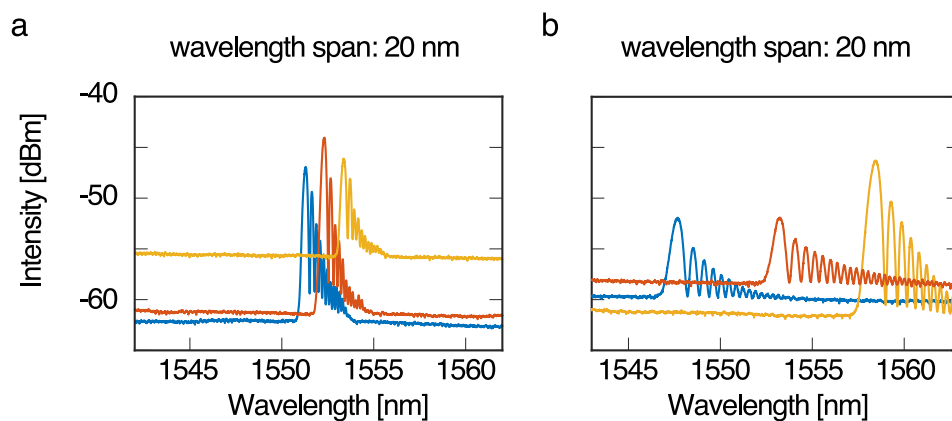


FIGURE 6.8: Demonstration of the spectral distance achievable by the method described in the paper and spectra of gratings inscribed under weak (a), and strong (b) bending conditions.

## 6.4 Summary

A simple method for realizing FBGs in a multicore fiber with different reflection wavelengths was presented. A conventional interferometric inscription arrangement is sufficient for the method realization. The modification of the grating properties is achieved by laying out the fiber in a specific curved shape before the gratings are inscribed in the cores simultaneously. After grating inscription, the fiber is straightened, resulting in a further separation of the wavelength reflection peaks. Therefore the limiting bending radius before overlapping the different FBGs spectra can be considerably smaller than the bending radius used for the grating inscription.



## Chapter 7

# Space division multiplexing with FBGs in a multicore fiber

This chapter is dedicated to a novel multicore optical waveguide component based on unique fiber designs optimized towards selective grating inscription combined with an extension of the applicable fiber length with such grating sensors. Such fiber design enables increasing the optical sensor capacity and, thus, the sensing length of a single optical fiber while preserving spatial resolution. The method used for the composed multicore fiber production allows achieving a specific performance which can be enabled by selective gratings inscription in a single fiber core, e.g., by using a focused femtosecond laser beam. It can also apply to a draw tower inscription process enabling a very efficient production of FBGs. Besides the concept, the chapter discusses the manufacturing of the sensing fiber component and an application example optimized for shape sensing.

Currently, the space-division multiplexing for fiber gratings is usually enabled by multiple single core fibers, as shown in Figure 7.1, or by selective fiber inscription in a multicore fiber, with multiple cores integrated in a common cladding.

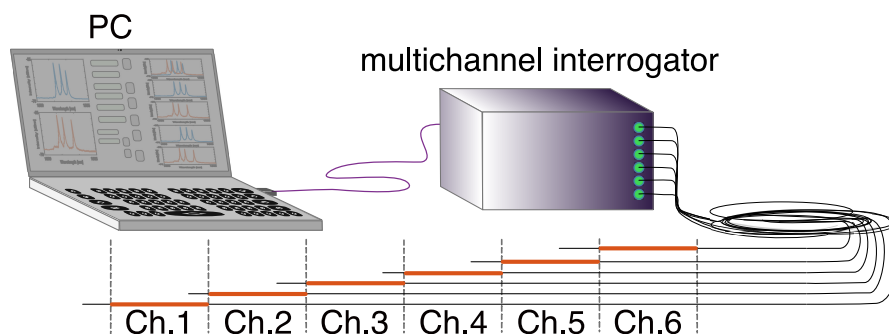


FIGURE 7.1: Conventional method with multiple single core fibers for sensing length extension based on space-division multiplexing.

A selective inscription in a single core of multicore fibers is currently achieved by special methods such as strong laser beam focusing, or limited coherence of a

light source providing an interference pattern with sufficient contrast for inscription of gratings only for part of the photosensitive cores [205, 206].

The cores with gratings then become sensitive to a specific external parameter measured using the fiber, while other cores, without gratings, remain insensitive. As a result, only one core is reflecting light in each position of the fiber. A sensing system for such spatially divided gratings is shown in Figure 7.2.

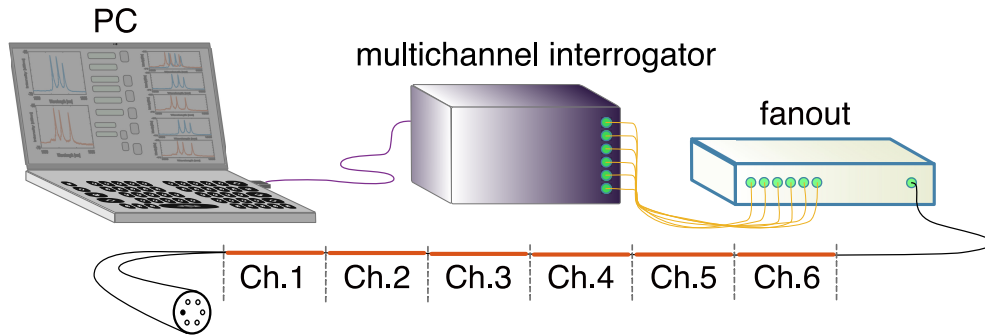


FIGURE 7.2: Optical fiber sensing length extension based on space-division multiplexing using, e.g., selectively inscribed FBGs.

Selective gratings inscription using different illumination conditions of the cores is time-consuming, due to the requirements for a precise fiber positioning. Here, an alternative method providing selective gratings inscription by illuminating all cores in parallel is presented. The suggested method allows for making a composed fiber component combining extended sensing length of multiple fibers with single cores and the compactness of a fiber sensor with selectively inscribed gratings in a multicore fiber. The process of a special fiber manufacturing is explained. As a proof of principle, a multicore fiber component was prepared for a fiber optical shape sensing application with two-fold extension of the measurement length using a selective grating inscription with a conventional interferometric setup.

## 7.1 Multicore fiber component concept

The composed multicore fiber component integrates the flexibility of selective grating inscription in multiple fibers for position multiplexing (Figure 7.3a), in a singular and compact multicore fiber component (Figure 7.3b). Different combinations of photosensitive and non-photosensitive cores allow for, e.g., a 6-fold or 12-fold length extension with cores placed in a ring shape (see fibers 1 and 2 in Figure 7.3c). Components made for shape sensing, with more than one sensing core in a cross-section, can also be designed using the same principle, as shown for fiber 3 in Figure 7.3c).

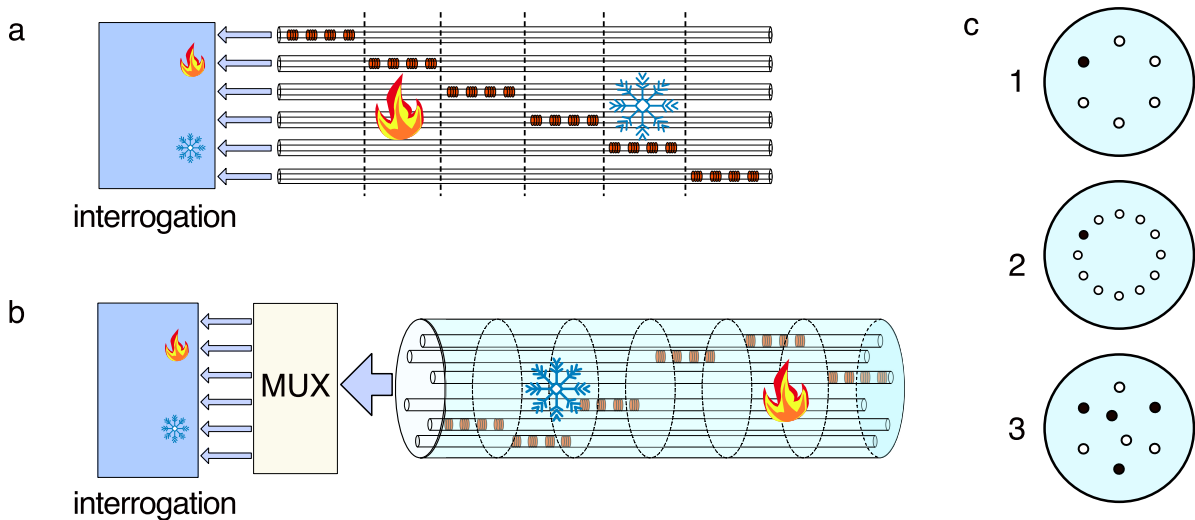


FIGURE 7.3: a) - Space-division multiplexing using single core fibers. b) - Concept of a space-division multiplexing based on a multicore fiber with selectively inscribed FBGs. c) - Examples of multicore fibers for selective FBG inscription based on photosensitive and non-photosensitive cores.

The multicore fiber component with photosensitive and non-photosensitive cores is composed of several pieces of the same fiber, spliced together with different orientation angles. Optical fiber cores with high germanium content have the ability to change refractive index for inscription of gratings under UV-illumination condition [207–209]. Other materials, usable for fiber production (boron, fluorine, aluminum oxide), show no or very poor photosensitivity to UV light. Now, purposely incorporating both high and low photosensitive cores in a single multicore fiber allows achieving a selective sensitivity to FBG inscription. If such fiber's cores are arranged in shape with rotational symmetry, it is possible to connect specific photosensitive and non-photosensitive, light-guiding cores to one another by splicing two separate rotated pieces of the fiber. If these pieces contain identical arrays of fiber gratings, their separation in channels allows for increasing the sensing networks' capacity for multiplexed sensing points. The interrogation of such fiber components is possible using a multichannel spectrometer or reflectometer or by a combination of a single-channel device and a fiber switch. Selective inscription of fiber gratings in the above-described multicore fibers can be achieved with the same setups as used for conventional FBG inscription, e.g., interferometric inscription setups.

The composed fiber component allows for extending the number of single sensors multiplexed within one fiber when identical grating arrays are interrogated. Alternatively, when splicing nonidentical arrays of gratings, the sensitivity of each piece can be tailored for components with different number of sensing points in spliced fiber pieces (Figure 7.4). This can be beneficial for the shape sensors which can combine different measurement ranges along the sensor length, e.g., cardiac

catheters, as shown in Figure 7.4.

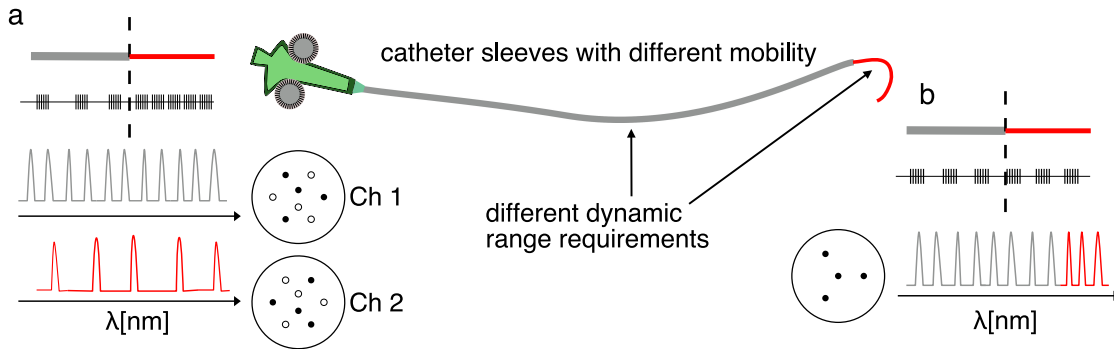


FIGURE 7.4: Combination of different sensitivity ranges enabled by different spectral distances in FBGs in suggested fiber component (a), compared to the conventional single fiber sensor (b).

The length of a usable sensitive area is determined by the losses or the attenuation in the sensing cores. The number of multiplexed gratings in a single-core channel is limited by the spectral range of the interrogator.

## 7.2 Multicore fiber component fabrication procedure

The stack-and-draw method can be used for the fabrication of the multicore fiber. For this purpose, several sub-preforms and filling rods are placed in a capillary tube (Figure 7.5a). The sub-preforms are made of different preforms with an increased core-to-cladding ratio. Germanium-doped fibers are well studied for fiber gratings inscription [207, 210]. Therefore, for the photosensitive cores, a high germanium content (>15%) is used for enabling high-reflectivity Bragg gratings inscription. Such doping concentration elevates the refractive index of a core [211–214], being beneficial since the mode field diameter becomes smaller and cross-talk between cores is reduced. On the other hand, a side effect of high-content germanium fibers is a higher transmission loss and a greater numerical aperture (NA). Transmission losses are not the major concern for fiber sensors with limited lengths in a range of meters to some hundreds of meters. The increased NA might be contributing to higher splicing losses when combined with non-photosensitive cores. In order to minimize the splicing losses, cores of both purposes should have comparable core size and refractive index.

Therefore, an essential requirement for a non-photosensitive preform material is the achievable refractive index contrast between core and cladding preferably the same values as for a photosensitive core.



The grating inscription may be performed during the fiber drawing process before coating application (Figure 7.5b), or after fiber drawing, through a UV-transparent coating [215], or with a removed coating.

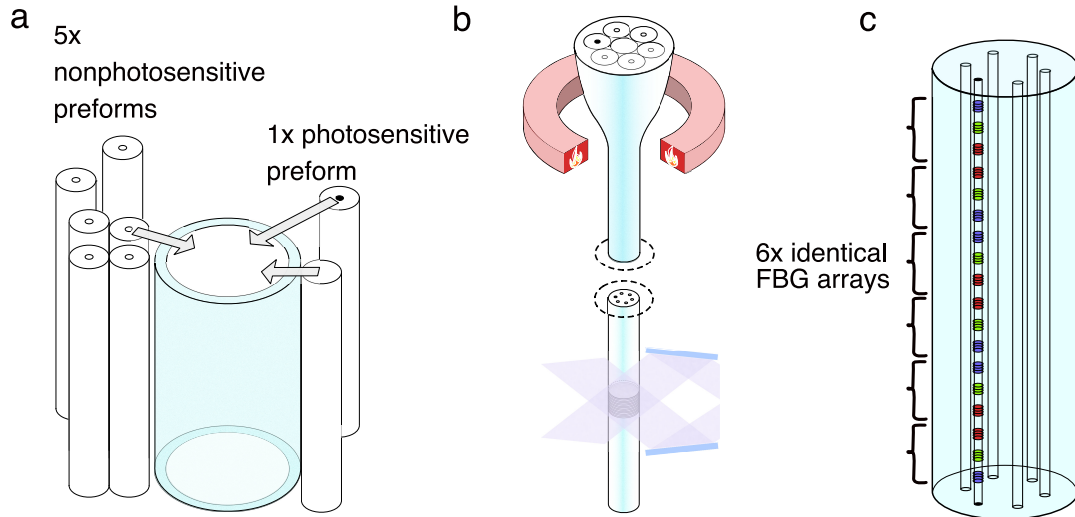


FIGURE 7.5: Process of a concept fiber manufacturing. a) - Preform stacking, space in between sub-preforms is filled with silica rods. b) Fiber Bragg gratings inscription during the fiber drawing process. c) The resulting fiber has FBGs inscribed only in photosensitive cores.

With an inscription process, a repeated sequence of spectrally resolved gratings (Figure 7.5c) or a continuous periodic structure can be achieved. Further steps are cutting the fiber in a way that each piece contains the gratings, which are supposed to be interrogated in discrete channels, rotated in respect to each other, and spliced again (Figure 7.6). As a result, a fiber component is achieved.

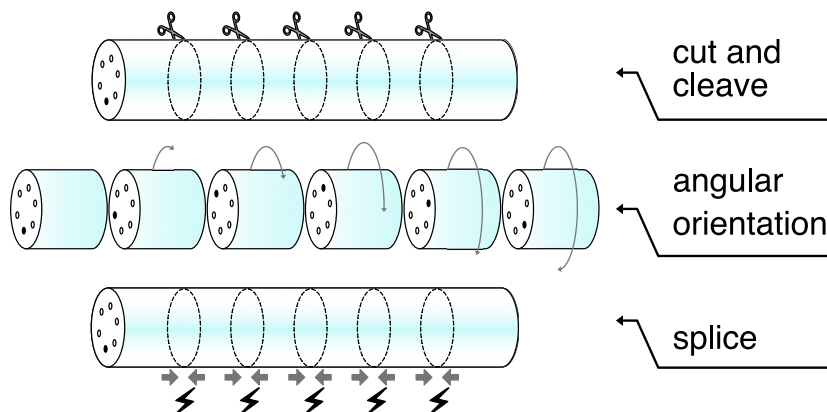


FIGURE 7.6: Further fiber handling, component preparation. The fiber is cut in pieces with arrays of FBGs. Then, different parts are connected and spliced so that each resulting core channel has only one sensing component.

### 7.3 Proof of principle with two connected elements

In order to validate multiplexing functionality of the suggested multicore fiber component, experimental results of FBG inscription in a multicore fiber with four photosensitive cores (Figure 7.3c, fiber 3) are given. In this specific example, it extended the length by a factor of two compared to a conventional fiber sensor with four photosensitive cores. For the extended concept, the fiber has to consist of an additional set of cores with very low photosensitivity in addition to photosensitive cores. For the photosensitive cores, a sub-preform with 15mol% of germanium has been chosen. The sub-preform was cut into four pieces to provide four cores with identical parameters for the final stacked preform.

The selection of a non-photosensitive sub-preform material is optimized towards matching with the photosensitive core with an expected NA of 0.25 and a core diameter of 4.5 $\mu\text{m}$ . There is a number of materials available with matching properties studied for both dispersion and photosensitivity [216–220]. Aluminum oxide ( $\text{Al}_2\text{O}_3$ ) is one of the dopants which has high  $\Delta n$  [221, 222]. A design with four photosensitive fiber cores has been chosen, matching the hexagonal symmetry of the stacking and providing the required structure for a shape sensing application. There is a limitation of the allowed  $\text{Al}_2\text{O}_3$  concentration in the cores due to a risk of crystallization and mechanical stress. Therefore, a sub-preform with 5%  $\text{Al}_2\text{O}_3$  has been used for the preform stack as shown in Figure 7.7a. With this low concentration, a lower numerical aperture compared to germanium-doped cores is achieved (about 0.17). A coupling efficiency in a splice of a germania and aluminum core of about 70% is expected.

The cross-section of the final realized multicore fiber is shown in Figure 7.7b. An additional hole was implemented for creating asymmetry for a simple fiber orientation when splicing using a side-view image, and for a scattering pattern analysis-based orientation measurement. Multicore fibers with four cores are often used for directional bending and shape sensing. Hence, the three outer cores were arranged equally distant from the center for bending measurement. The central photosensitive core is slightly offset from the center to be able to have a non-photosensitive twin core in the composed fiber component. The central core provides twist and strain discrimination, which is impossible to do with only three equidistant cores.

Fiber Bragg gratings have been inscribed in the multicore fiber in a post-drawing process. This was done using a single KrF excimer laser pulse and a Talbot interferometer. Two sequences of FBGs were inscribed, each sequence having three gratings with 1.5nm spectral distance between the reflection peaks. The second sequence was shifted by 1nm towards longer wavelengths, in respect to the first sequence, so

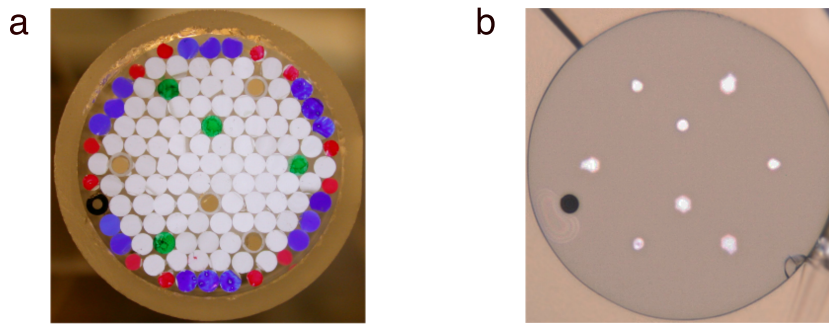


FIGURE 7.7: Experimental approximation of the multiplexing fiber concept. a) Stacked preform resembling the fiber structure with photosensitive sub-preforms marked green, insensitive to UV-light sub-preforms appear in dark-beige. b) Microscope image of the drawn fiber, larger cores correspond to the cores insensitive to UV-illumination, smaller cores represent the photosensitive cores.

that gratings of both sequences appear one after another in the reflection spectrum. This would allow to see additional peaks in case of a cross-talk between the cores. The fiber was cut so that each piece contained one sequence of three FBGs. These pieces were spliced with a rotational shift of  $180^\circ$  in respect to each other, as shown in Figure 7.8a. A fanout is used for interrogation of six outer cores. The spectra of the grating reflectivities for two of these six channels are shown in Figure 7.8b in different colors. No cross-talks were seen in the spectrum. The gratings in two channels have comparable reflectivities. The losses induced by the splice are therefore negligible. The other channels have shown very similar spectra.

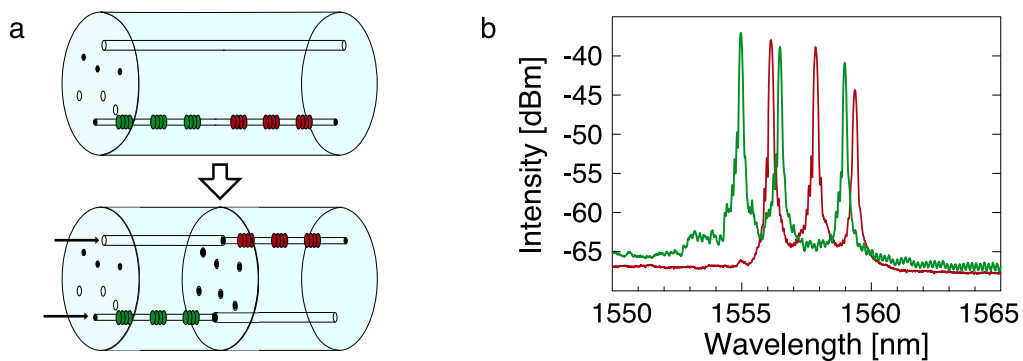


FIGURE 7.8: Experimental realization of the multiplexing fiber concept. a) Fiber component is prepared by splicing two pieces with a rotational shift of  $180^\circ$  b) Spectra of two cores.

The design of this fiber takes advantage of simplified orientation measurement, which is achieved with a hole incorporated in the cladding. In the case of the non-invasive measurement method, this hole will allow seeing the exact orientation of the fiber due to the unique position of the hole in the structure, unlike the orientation limited to the symmetry of the structure described in several cases in Chapter 3. In

the case of visually indistinguishable core sets, this hole will help to splice the fiber pieces to avoid incorrect splicing.

This result proves that the proposed multicore fiber can increase the capacity of optical sensors with fiber gratings as sensor elements.

### Three fold increase in length

The presented example has a factor of two of the sensing length extension. With a design with more cores it is possible to achieve longer sensor without inducing cross-talk between the cores. Configuration with nine outer cores and  $40^\circ$  shift in between the cores would enable a three-fold increase in the shape sensing length (Figure 7.9).

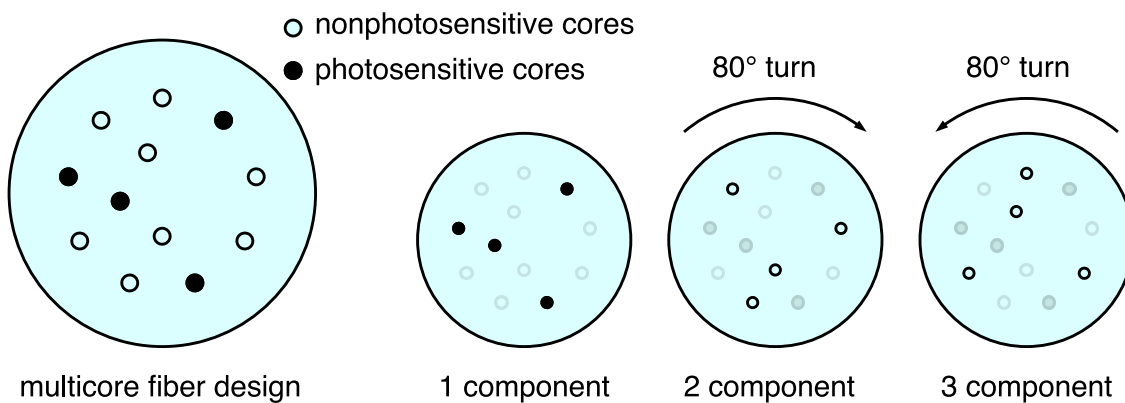


FIGURE 7.9: Design for a shape sensor with a three-fold increase in sensing length

An obstacle on the way of manufacturing the preform with this design is the difficulty to fit the structure to a hexagonal grid with an identical number of elements. Thus, other methods, such drilling and insertion, can be considered for realizing more advanced length extension.

## 7.4 Summary

A novel composed fiber component exploiting a special fiber design principle is presented. This design principle enables multiplexing-based space-division multiplexing with arrays of fiber gratings separated in sets of channels. The main advantage of the design is a simple realization of selective fiber grating inscription without the need of creating different illumination conditions for the cores of a multicore fiber, e.g., focusing or limited coherence illumination. Stacking of preforms with different doping materials can be performed with standard techniques. Selective gratings inscription is provided by the different dopings (photosensitive and non-photosensitive) in the cores of the multicore fiber. Selectively inscribed grating

---

sets can then be separated into channels by cutting the fiber into a few pieces and splicing them together with a rotational shift to provide transmission of the gratings signals from one piece through others via unmodified cores. This allows for achieving multiple times longer sensors compared to single core fibers with FBGs with identical spectral properties. An example of a multicore fiber designed for bend and shape sensors multiplexing was manufactured and tested with several gratings. The presented design example allows for increasing the sensing length by a factor of two without reducing spatial resolution.



## Chapter 8

# Conclusions and outlook for future work

In the presented dissertation, several aspects contributing to the optimization of shape sensors based on multicore fibers are discussed. These aspects include the orientation and twist measurement in complex optical fibers, fibers characterization and calibration, FBG inscription in multicore fibers, and finally, conceptual aspects with new multiplexing methods.

Multicore fibers angular orientation method study became a skeleton of the work as it is used in many parts of the research. The scattering pattern achieved by a laser side illumination of multicore fiber showed sufficient detail to be used for angular orientation of multicore fibers. In combination with the correlation coefficient measurement, the measurement system allows for quick automatic recognition of fiber orientation. A method based on Pearson coefficient calculation allows for automatic orientation measurement. One of the most promising applications for this method would be a fiber characterization running during a fiber drawing process. The results obtained in this work suggest that the orientation angle recognition can be used not only with experimental reference scattering patterns but also with a simulated reference patterns stack. Using the simulated patterns would enable the characterization of a fiber already with first preparing a test fiber.

Fiber Bragg gratings have been reviewed as a successful instrument for enabling curvature and shape sensing in multicore fibers. However, the fiber gratings inscription is a more complex process compared to the single core fibers. The lensing and diffraction effects would differently affect the FBG inscription in the cores of a multicore fiber depending on the illumination angle. The effects of focusing can negatively affect the applicability of inscribed FBGs since very low reflective grating, and very high reflective gratings are not desirable for best interrogation system performance. When possible, the orientation of a multicore fiber must be controlled for the FBG inscription. This study aimed to reduce or eliminate the negative optical effects on cores induced in a multicore fiber. However, the focusing effect of the

fiber cladding might also be used for achieving FBGs with higher reflectivity at the lower illumination conditions. Such a technique can be realized, e.g., by inscribing the gratings in a fiber with a core offset from the center.

Sophisticated components and interrogation instrumentation required for the multicore fibers are obstacles to a general implementation of multicore fiber sensors due to high costs and the need for customization for specific applications. Lack of a standard for multicore fiber leads to underdeveloped instrumentation, which increases overall complexity and costs. Bending the fiber for FBG writing will apply strain to the cores depending on the location regarding the neutral axis. This restrained condition of the cores for simultaneous FBG inscription with identical gratings would then allow the reflection peak wavelengths to be separated in the spectral domain after straightening the fiber. This concept can be used for short multicore fiber sensors with a short wavelength interrogation range.

Calibration is a standard process for optical fiber sensors. Calibration is specifically important for using multicore fibers in shape sensing because of the geometrical and material content variations appearing in the state-of-the-art multicore fibers. The calibration algorithms can be automatized and combined. For example, instead of dedicated measurements for photo-elastic coefficient and thickness variation, the sensors may be curved with known conditions multiple times, and optimization of the parameters used for the calculation may be performed by adapting the parameters for ground truth.

Spectral limitations of FBG interrogators limit the number of sensing points, therefore, the length of optical sensors based on fiber gratings. Large sensor capacity is paramount for multicore fiber shape sensors, as the strain measurement should be performed in many cores concurrently. Combining different fiber doping materials allowed to achieve cores with different functionalities and photosensitivity in a single fiber. In the fiber component prepared using such fiber, a series of light-guiding and sensing cores provide spatially resolved measurement. Hence, the sensing fiber capacity can be increased by a factor of  $N$ , where  $N$  is the number of all cores divided by a number of sensing cores.



# Bibliography

1. Williams, E. F. *et al.* Distributed sensing of microseisms and teleseisms with submarine dark fibers. *Nature communications* **10**, 1–11 (2019).
2. Burnett, J., Blanchard, P. & Greenaway, A. Optical Fibre-based Vectorial Shape Sensor. *Strain* **36**, 127–133 (2000).
3. Gander, M. *et al.* Bend measurement using multicore optical fiber in *Optical Fiber Sensors* (1997), OWC6.
4. Duncan, R. R. & Raum, M. Fiber-optic shape and position sensing in *Proceedings of the 5th International Conference on Structural Health Monitoring* (2005), 804–811.
5. Duncan, R. G. *et al.* High-accuracy fiber-optic shape sensing in *Sensor Systems and Networks: Phenomena, Technology, and Applications for NDE and Health Monitoring 2007* **6530** (2007), 65301S.
6. Moore, J. P. & Rogge, M. D. Shape Sensing Using Multi-Core Fiber Optic Cable and Parametric Curve Solutions. en. *Optics Express* **20**, 2967. ISSN: 1094-4087 (Jan. 2012).
7. Kirby III, G. C., Lindner, D. K., Davis, M. A. & Kersey, A. D. Optimal sensor layout for shape estimation from strain sensors in *Smart Structures and Materials 1995: Smart Sensing, Processing, and Instrumentation* **2444** (1995), 367–376.
8. Leal-Junior, A. G., Frizera, A. & Pontes, M. J. Sensitive zone parameters and curvature radius evaluation for polymer optical fiber curvature sensors. *Optics & Laser Technology* **100**, 272–281 (2018).
9. Chen, X., Zhang, C., Webb, D. J., Kalli, K. & Peng, G.-D. Highly sensitive bend sensor based on Bragg grating in eccentric core polymer fiber. *IEEE photonics technology letters* **22**, 850–852 (2010).
10. Gherlone, M., Cerracchio, P. & Mattone, M. Shape Sensing Methods: Review and Experimental Comparison on a Wing-Shaped Plate. *Progress in Aerospace Sciences* **99**, 14–26. ISSN: 03760421 (May 2018).
11. Koch, E. & Dietzel, A. Surface Reconstruction by Means of a Flexible Sensor Array. *Sensors and Actuators A: Physical* **267**, 293–300. ISSN: 09244247 (Nov. 2017).

12. Schaefer, P.-L., Barrier, G., Chagnon, G., Alonso, T. & Moreau-Gaudry, A. Strain Gauges Based 3D Shape Monitoring of Beam Structures Using Finite Width Gauge Model. *Experimental Techniques* **43**, 599–611. ISSN: 0732-8818, 1747-1567 (Oct. 2019).
13. Plamondon, A. *et al.* Evaluation of a Hybrid System for Three-Dimensional Measurement of Trunk Posture in Motion. *Applied Ergonomics* **38**, 697–712. ISSN: 00036870 (Nov. 2007).
14. Dementyev, A., Kao, H.-L. C. & Paradiso, J. A. *SensorTape: Modular and Programmable 3D-Aware Dense Sensor Network on a Tape* in *Proceedings of the 28th Annual ACM Symposium on User Interface Software & Technology* UIST '15: The 28th Annual ACM Symposium on User Interface Software and Technology (ACM, Charlotte NC USA, Nov. 5, 2015), 649–658. ISBN: 978-1-4503-3779-3.
15. Ye, X. W., Dong, C. Z. & Liu, T. A Review of Machine Vision-Based Structural Health Monitoring: Methodologies and Applications. *Journal of Sensors* **2016**, 1–10. ISSN: 1687-725X, 1687-7268 (2016).
16. Cha, Y.-J., Choi, W. & Büyüköztürk, O. Deep Learning-Based Crack Damage Detection Using Convolutional Neural Networks: Deep Learning-Based Crack Damage Detection Using CNNs. *Computer-Aided Civil and Infrastructure Engineering* **32**, 361–378. ISSN: 10939687 (May 2017).
17. Frau, A, Pieczonka, L, Porcu, M. C., Staszewski, W. J. & Aymerich, F. Analysis of Elastic Nonlinearity for Impact Damage Detection in Composite Laminates. *Journal of Physics: Conference Series* **628**, 012103. ISSN: 1742-6588, 1742-6596 (July 9, 2015).
18. Wong, W. Y. & Wong, M. S. Detecting Spinal Posture Change in Sitting Positions with Tri-Axial Accelerometers. *Gait & Posture* **27**, 168–171. ISSN: 09666362 (Jan. 2008).
19. Choi, S., Kim, B., Lee, H., Kim, Y. & Park, H. A Deformed Shape Monitoring Model for Building Structures Based on a 2D Laser Scanner. *Sensors* **13**, 6746–6758. ISSN: 1424-8220 (May 21, 2013).
20. Gentile, C. in *Radar Technology* (ed Kouemou, G.) (InTech, Jan. 1, 2010). ISBN: 978-953-307-029-2.
21. Gentile, C. & Bernardini, G. Radar-Based Measurement of Deflections on Bridges and Large Structures. *European Journal of Environmental and Civil Engineering* **14**, 495–516. ISSN: 1964-8189, 2116-7214 (Apr. 2010).
22. Hill, K. O. & Meltz, G. Fiber Bragg grating technology fundamentals and overview. *Journal of Lightwave Technology* **15**, 1263–1276. ISSN: 07338724 (1997).

23. Xiong, L., Jiang, G., Guo, Y., Kuang, Y. & Liu, H. Investigation of the temperature compensation of FBGs encapsulated with different methods and subjected to different temperature change rates. *Journal of Lightwave Technology* **37**, 917–926 (2019).
24. Haran, F. M., Rew, J. K. & Foote, P. D. A strain-isolated fibre Bragg grating sensor for temperature compensation of fibre Bragg grating strain sensors. *Measurement Science and Technology* **9**, 1163 (1998).
25. Hsu, Y., Wang, L., Liu, W.-F. & Chiang, Y. Temperature compensation of optical fiber Bragg grating pressure sensor. *IEEE Photonics Technology Letters* **18**, 874–876 (2006).
26. Frenet, F. Sur les courbes a double courbure. *Journal de mathematiques pures et appliquees 1 serie* **17**, 437–447 (1852).
27. Askins, C. G., Miller, G. A. & Friebele, E. J. Bend and twist sensing in a multiple-core optical fiber in *OFC/NFOEC 2008-2008 Conference on Optical Fiber Communication/National Fiber Optic Engineers Conference* (2008), 1–3.
28. Yin, G. *et al.* Distributed directional torsion sensing based on an optical frequency domain reflectometer and a helical multicore fiber. *Opt. Express* **28**, 16140–16150 (May 2020).
29. Cooper, L. J. *et al.* Design and Performance of Multicore Fiber Optimized towards Communications and Sensing Applications en. in *SPIE OPTO* (eds Jiang, S. & Digonnet, M. J. F.) (San Francisco, California, United States, Apr. 2015), 93590H.
30. Floris, I., Madrigal, J., Sales, S., Calderón, P. A. & Adam, J. M. Twisting compensation of optical multicore fiber shape sensors for flexible medical instruments in *Optical Fibers and Sensors for Medical Diagnostics and Treatment Applications XX* **11233** (International Society for Optics and Photonics, 2020), 1123316.
31. Porcu, M., Patteri, D., Melis, S. & Aymerich, F. Effectiveness of the FRF Curvature Technique for Structural Health Monitoring. *Construction and Building Materials* **226**, 173–187. ISSN: 09500618 (Nov. 2019).
32. MacPherson, W. N. *et al.* Tunnel Monitoring Using Multicore Fibre Displacement Sensor. *Measurement Science and Technology* **17**, 1180–1185. ISSN: 0957-0233, 1361-6501 (May 1, 2006).
33. Lopez-Higuera, J. M., Rodriguez Cobo, L., Quintela Incera, A. & Cobo, A. Fiber Optic Sensors in Structural Health Monitoring. *Journal of Lightwave Technology* **29**, 587–608. ISSN: 0733-8724, 1558-2213 (Feb. 2011).

34. Ye, X. W., Su, Y. H. & Han, J. P. Structural Health Monitoring of Civil Infrastructure Using Optical Fiber Sensing Technology: A Comprehensive Review. *The Scientific World Journal* **2014**, 1–11. ISSN: 2356-6140, 1537-744X (2014).
35. Barrias, A., Casas, J. & Villalba, S. A Review of Distributed Optical Fiber Sensors for Civil Engineering Applications. *Sensors* **16**, 748. ISSN: 1424-8220 (May 23, 2016).
36. Vallan, A., Carullo, A., Casalicchio, M. L. & Perrone, G. *Design and characterization of curvature sensors based on plastic optical fibers for structural monitoring in 2013 IEEE International Instrumentation and Measurement Technology Conference (I2MTC)* (2013), 996–1000.
37. Qiao, Q., Borghesan, G., De Schutter, J. & Vander Poorten, E. Force from Shape—Estimating the Location and Magnitude of the External Force on Flexible Instruments. *IEEE Transactions on Robotics*, 1–8. ISSN: 1552-3098, 1941-0468 (2021).
38. Lu, Y., Lu, B., Li, B., Guo, H. & Liu, Y.-h. Robust Three-Dimensional Shape Sensing for Flexible Endoscopic Surgery Using Multi-Core FBG Sensors. *IEEE Robotics and Automation Letters* **6**, 4835–4842. ISSN: 2377-3766, 2377-3774 (July 2021).
39. Vincent, M., Eric, L., Christian, V., Johan, V. & Jessica, B.-K. *Curvature and Shape Sensing for Continuum Robotics Using Draw Tower Gratings in Multi Core Fiber in Optical Fiber Sensors* (Optical Society of America, 2018), ThE70.
40. Arkwright, J. W. *et al.* Design of a High-Sensor Count Fibre Optic Manometry Catheter for in-Vivo Colonic Diagnostics. *Optics Express* **17**, 22423. ISSN: 1094-4087 (Dec. 7, 2009).
41. Al-Ahmad, O., Ourak, M., Vlekken, J. & Vander Poorten, E. FBG-Based Estimation of External Forces Along Flexible Instrument Bodies. *Frontiers in Robotics and AI* **8**, 718033. ISSN: 2296-9144 (July 30, 2021).
42. Ourak, M. *et al.* Fusion of Biplane Fluoroscopy With Fiber Bragg Grating for 3D Catheter Shape Reconstruction. *IEEE Robotics and Automation Letters* **6**, 6505–6512. ISSN: 2377-3766, 2377-3774 (Oct. 2021).
43. Nicolas, M. J., Sullivan, R. W. & Richards, W. L. Large scale applications using FBG sensors: determination of in-flight loads and shape of a composite aircraft wing. *Aerospace* **3**, 18 (2016).
44. Ma, Z. & Chen, X. Fiber Bragg gratings sensors for aircraft wing shape measurement: Recent applications and technical analysis. *Sensors* **19**, 55 (2019).

45. Pinto, N., Frazao, O, Baptista, J. M. & Santos, J. Quasi-distributed displacement sensor for structural monitoring using a commercial OTDR. *Optics and lasers in Engineering* **44**, 771–778 (2006).
46. Wang, X. *et al.* An OTDR and gratings assisted multifunctional fiber sensing system. *IEEE Sensors Journal* **15**, 4660–4666 (2015).
47. Nakamura, K., Husdi, I. R. & Ueha, S. A distributed strain sensor with the memory effect based on the POF OTDR in *17th International Conference on Optical Fibre Sensors* **5855** (2005), 807–810.
48. Tangudu, R. & Sahu, P. K. Strain resolution enhancement in Rayleigh-OTDR based DSS system using LWT-MPSO scheme. *Optik* **176**, 102–113 (2019).
49. Zhang, Z. & Bao, X. Distributed optical fiber vibration sensor based on spectrum analysis of Polarization-OTDR system. *Optics express* **16**, 10240–10247 (2008).
50. Liu, T. *et al.* Ultra-high resolution distributed strain sensing based on phase-OTDR in *2019 Optical Fiber Communications Conference and Exhibition (OFC)* (2019), 1–3.
51. Masoudi, A., Belal, M. & Newson, T. A distributed optical fibre dynamic strain sensor based on phase-OTDR. *Measurement Science and Technology* **24**, 085204 (2013).
52. Zhao, Z., Soto, M. A., Tang, M. & Thévenaz, L. Distributed Shape Sensing Using Brillouin Scattering in Multi-Core Fibers. en. *Optics Express* **24**, 25211. ISSN: 1094-4087 (Oct. 2016).
53. Zafeiropoulou, A., Masoudi, A., Cooper, L. & Brambilla, G. Distributed shape sensing with a multicore fibre based on BOTDR technique in *26th International Conference on Optical Fiber Sensors* (Optical Society of America, 2018), ThE15.
54. Zafeiropoulou, A., Masoudi, A., Zdagkas, A., Cooper, L. & Brambilla, G. Curvature sensing with a D-shaped multicore fibre and Brillouin optical time-domain reflectometry. en. *Opt. Express* **28**, 1291. ISSN: 1094-4087 (Jan. 2020).
55. Yamaguchi, T. & Shinoda, Y. Development of fast FBG interrogator with wavelength-swept laser in *Optical Sensors 2015* (eds Baldini, F., Homola, J. & Lieberman, R. A.) **9506** (SPIE, 2015), 272 –279.
56. Qin, C. *et al.* FBG interrogation method based on wavelength-swept laser in *International Conference on Optics in Precision Engineering and Nanotechnology (icOPEN2013)* (eds Quan, C., Qian, K. & Asundi, A.) **8769** (SPIE, 2013), 572 –578.

57. Slavík, R. & LaRochelle, S. Large-Band Periodic Filters for DWDM Using Multiple-Superimposed Fiber Bragg Gratings. *IEEE photonics technology letters* **14**, 1704–1706 (2002).
58. Askins, C. G., Putnam, M. A., Williams, G. M. & Friebele, E. J. Stepped-Wavelength Optical-Fiber Bragg Grating Arrays Fabricated in Line on a Draw Tower. *Optics letters* **19**, 147–149 (1994).
59. Goh, C. S. *et al.* Wavelength Tuning of Fiber Bragg Gratings over 90 Nm Using a Simple Tuning Package. *IEEE Photonics Technology Letters* **15**, 557–559 (2003).
60. Yang, Z., Albrow-Owen, T., Cai, W. & Hasan, T. Miniaturization of optical spectrometers. *Science* **371**, eabe0722 (2021).
61. Das, B. & Chandra, V. Fiber-MZI-based FBG sensor interrogation: comparative study with a CCD spectrometer. *Appl. Opt.* **55**, 8287–8292 (Oct. 2016).
62. Konishi, T. & Yamasaki, Y. *Compact and cost-effective multi-channel optical spectrometer for fine FBG sensing in IoT technology in Optical Data Science: Trends Shaping the Future of Photonics* (eds Jalali, B., ichi Kitayama, K. & Mahjoubfar, A.) **10551** (SPIE, 2018), 31–37.
63. Li, J. *et al.* High spatial resolution distributed fiber strain sensor based on phase-OFDR. *Optics express* **25**, 27913–27922 (2017).
64. Zhao, S. *et al.* Performance investigation of OFDR sensing system with a wide strain measurement range. *Journal of Lightwave Technology* **37**, 3721–3727 (2019).
65. Kwon, Y.-S., Seo, D.-C., Choi, B.-H., Jeon, M. Y. & Kwon, I.-B. Strain measurement distributed on a ground anchor bearing plate by fiber optic OFDR sensor. *Applied Sciences* **8**, 2051 (2018).
66. Ding, Z. *et al.* Distributed strain and temperature discrimination using two types of fiber in OFDR. *IEEE Photonics Journal* **8**, 1–8 (2016).
67. Leyendecker, P & Haslinger, R. *Fiber optic curvature sensor in IEEE SENSORS 2014 Proceedings* (2014), 43–46. ISBN: 1930-0395 VO -.
68. Bos, J., Klein, J., Froggatt, M., Sanborn, E. & Gifford, D. *Fiber optic strain, temperature and shape sensing via OFDR for ground, air and space applications in Nanophotonics and Macrophotonics for Space Environments VII* **8876** (2013), 887614.
69. Parent, F. *et al.* Enhancement of accuracy in shape sensing of surgical needles using optical frequency domain reflectometry in optical fibers. *Biomedical optics express* **8**, 2210–2221 (2017).

70. Lally, E. M., Reaves, M., Horrell, E., Klute, S. & Froggatt, M. E. *Fiber optic shape sensing for monitoring of flexible structures in Sensors and Smart Structures Technologies for Civil, Mechanical, and Aerospace Systems 2012* **8345** (2012), 83452Y.
71. Ohanian, O. J. *et al.* *OFDR on photonic circuits: Fiber optic sensing infrastructure and applications in Optical Fiber Sensors* (2018), WB1.
72. Triana, A., Pastor, D. & Varón, M. A Code Division Design Strategy for Multiplexing Fiber Bragg Grating Sensing Networks. *en. Sensors* **17**, 2508. ISSN: 1424-8220 (Nov. 2017).
73. Sweetser, J., Johnson, A. & Grunnet-Jepsen, A. *Demonstration of Code-Division Multiplexing with Synchronous Orthogonal Coding Using Fiber Bragg Gratings in OFC 2001. Optical Fiber Communication Conference and Exhibit. Technical Digest Postconference Edition (IEEE Cat. 01CH37171)* **4** (Opt. Soc. America, Anaheim, CA, USA, 2001), ThH3-T1-3. ISBN: 978-1-55752-655-7.
74. Triana, C. A., Pastor, D. & Varón, M. Optical Code Division Multiplexing in the Design of Encoded Fiber Bragg Grating Sensors. *en. Opt. Pura Apl.* **49**, 17-28. ISSN: 21718814, 00303917 (Mar. 2016).
75. Götten, M., Lochmann, S., Ahrens, A., Lindner, E. & Van Roosbroeck, J. 2000 Serial FBG Sensors Interrogated With a Hybrid CDM-WDM Scheme. *Journal of Lightwave Technology* **38**, 2493-2503 (2020).
76. Götten, M. *et al.* A CDM-WDM Interrogation Scheme for Massive Serial FBG Sensor Networks. *IEEE Sensors Journal*, 1-1 (2021).
77. Feng, D. *et al.* Co-Located Angularly Offset Fiber Bragg Grating Pair for Temperature-Compensated Unambiguous 3D Shape Sensing. *Applied Optics* **60**, 4185. ISSN: 1559-128X, 2155-3165 (May 10, 2021).
78. Liu, Z. *et al.* Temperature-Insensitive Curvature Sensor Based on Bragg Gratings Written in Strongly Coupled Multicore Fiber. *Optics Letters* **46**, 3933. ISSN: 0146-9592, 1539-4794 (Aug. 15, 2021).
79. Zhu, W. *et al.* Shape Reconstruction Based on a Multicore Optical Fiber Array with Temperature Self-Compensation. *Applied Optics* **60**, 5795. ISSN: 1559-128X, 2155-3165 (July 10, 2021).
80. Liu, Y., Zhou, A. & Yuan, L. Multifunctional Fiber-Optic Sensor, Based on Helix Structure and Fiber Bragg Gratings, for Shape Sensing. *Optics & Laser Technology* **143**, 107327. ISSN: 00303992 (Nov. 2021).
81. Chen, Z. *et al.* Demonstration of Large Curvature Radius Shape Sensing Using Optical Frequency Domain Reflectometry in Multi-Core Fibers. *IEEE Photonics Journal* **13**, 1-9. ISSN: 1943-0655, 1943-0647 (Aug. 2021).

82. Issatayeva, A., Amantayeva, A., Blanc, W., Tosi, D. & Molardi, C. Design and Analysis of a Fiber-Optic Sensing System for Shape Reconstruction of a Minimally Invasive Surgical Needle. *Scientific Reports* **11**, 8609. issn: 2045-2322 (Dec. 2021).
83. Snyder, A. W. Coupled-Mode Theory for Optical Fibers. *J. Opt. Soc. Am.* **62**, 1267–1277 (Nov. 1972).
84. Yariv, A. Coupled-mode theory for guided-wave optics. *IEEE Journal of Quantum Electronics* **9**, 919–933 (1973).
85. Haus, H. & Huang, W. Coupled-mode theory. *Proceedings of the IEEE* **79**, 1505–1518 (1991).
86. Zhou, W., Dong, X., Ni, K., Chan, C. & Shum, P. Temperature-insensitive accelerometer based on a strain-chirped FBG. *Sensors and Actuators A: Physical* **157**, 15–18 (2010).
87. Tang, Z. *et al.* Tunable optoelectronic oscillator based on a polarization modulator and a chirped FBG. *IEEE Photonics Technology Letters* **24**, 1487–1489 (2012).
88. Li, S., Ngo, N., Tjin, S., Shum, P & Zhang, J. Thermally tunable narrow-bandpass filter based on a linearly chirped fiber Bragg grating. *Optics letters* **29**, 29–31 (2004).
89. Theodosiou, A. *et al.* Er/Yb double-clad fiber laser with fs-laser inscribed plane-by-plane chirped FBG laser mirrors. *IEEE Photonics Technology Letters* **31**, 409–412 (2019).
90. Dar, A. B. & Jha, R. K. Chromatic dispersion compensation techniques and characterization of fiber Bragg grating for dispersion compensation. *Optical and Quantum Electronics* **49**, 108 (2017).
91. Lee, S *et al.* Adjustable compensation of polarization mode dispersion using a high-birefringence nonlinearly chirped fiber Bragg grating. *IEEE Photonics Technology Letters* **11**, 1277–1279 (1999).
92. Meena, M. & Gupta, R. K. Design and comparative performance evaluation of chirped FBG dispersion compensation with DCF technique for DWDM optical transmission systems. *Optik* **188**, 212–224 (2019).
93. Berger, N. K. *et al.* Temporal differentiation of optical signals using a phase-shifted fiber Bragg grating. *Optics express* **15**, 371–381 (2007).
94. Rosenthal, A., Razansky, D. & Ntziachristos, V. High-sensitivity compact ultrasonic detector based on a pi-phase-shifted fiber Bragg grating. *Optics letters* **36**, 1833–1835 (2011).



95. Agrawal, G. P. & Radic, S. Phase-shifted fiber Bragg gratings and their application for wavelength demultiplexing. *IEEE photonics technology letters* **6**, 995–997 (1994).
96. Guan, B.-O., Tam, H.-Y., Tao, X.-M. & Dong, X.-Y. Simultaneous strain and temperature measurement using a superstructure fiber Bragg grating. *IEEE Photonics Technology Letters* **12**, 675–677 (2000).
97. Alemohammad, H. & Toyserkani, E. Simultaneous measurement of temperature and tensile loading using superstructure FBGs developed by laser direct writing of periodic on-fiber metallic films. *Smart materials and structures* **18**, 095048 (2009).
98. Patrick, H. J. & Vohra, S. T. *Fiber bragg grating with long-period fiber grating superstructure for simultaneous strain and temperature measurement in European Workshop on Optical Fibre Sensors* **3483** (1998), 264–267.
99. Zhang, A.-P., Guan, B.-O., Tao, X.-M. & Tam, H.-Y. Mode couplings in superstructure fiber Bragg gratings. *IEEE Photonics Technology Letters* **14**, 489–491 (2002).
100. Zychowicz, Ł., Klimek, J. & Kisala, P. Methods of producing apodized fiber Bragg gratings and examples of their applications. *Informatyka, Automatyka, Pomiar w Gospodarce i Ochronie Środowiska* **8** (2018).
101. Singh, H. & Zippin, M. *Apodized Fiber Bragg Gratings for DWDM Applications Using Uniform Phase Mask in 24th European Conference on Optical Communication. ECOC'98 (IEEE Cat. No. 98TH8398)* **1** (IEEE, 1998), 189–190.
102. Ashry, I, Elrashidi, A, Mahros, A, Alhaddad, M & Elleithy, K. *Investigating the performance of apodized Fiber Bragg gratings for sensing applications in Proceedings of the 2014 Zone 1 Conference of the American Society for Engineering Education* (2014), 1–5.
103. Hill, K. O., Fujii, Y., Johnson, D. C. & Kawasaki, B. S. Photosensitivity in optical fiber waveguides: Application to reflection filter fabrication. *Applied Physics Letters* **32**, 647–649. ISSN: 10773118 (1978).
104. Lam, D. K. W. & Garside, B. K. Characterization of single-mode optical fiber filters. *Applied Optics* **20**, 440. ISSN: 0003-6935 (1981).
105. Glass, A. M. The Photorefractive Effect. *Optical Engineering* **17**, 476. ISSN: 0091-3286 (Oct. 1978).
106. Meltz, G, Morey, W. W. & Glenn, W. H. Formation of Bragg gratings in optical fibers by a transverse holographic method. *Optics Letters* **14**, 823–825 (1989).

107. Hill, K. O., Malo, B., Bilodeau, F., Johnson, D. C. & Albert, J. Bragg gratings fabricated in monomode photosensitive optical fiber by UV exposure through a phase mask. *Applied Physics Letters* **62**, 1035–1037. ISSN: 00036951 (1993).
108. Niu, H. *et al.* Fabrication and application of a novel long period fiber grating with arched fiber cores. *Optical Fiber Technology* **67**, 102708. ISSN: 1068-5200 (2021).
109. Pérez-Millán, P., Torres-Peiró, S., Cruz, J. & Andrés, M. Fabrication of chirped fiber Bragg gratings by simple combination of stretching movements. *Optical Fiber Technology* **14**, 49–53. ISSN: 1068-5200 (2008).
110. Zhang, Q. *et al.* Tuning Bragg wavelength by writing gratings on prestrained fibers. *IEEE Photonics Technology Letters* **6**, 839–841 (1994).
111. Mihailov, S. J. *et al.* Ultrafast Laser Processing of Optical Fibers for Sensing Applications. *Sensors* **21**, 1447. ISSN: 1424-8220 (Feb. 19, 2021).
112. Stuart, B. C. *et al.* Optical Ablation by High-Power Short-Pulse Lasers. *Journal of the Optical Society of America B* **13**, 459. ISSN: 0740-3224, 1520-8540 (Feb. 1, 1996).
113. Schaffer, C. B., Brodeur, A. & Mazur, E. Laser-Induced Breakdown and Damage in Bulk Transparent Materials Induced by Tightly Focused Femtosecond Laser Pulses. *Measurement Science and Technology* **12**, 1784–1794. ISSN: 0957-0233, 1361-6501 (Nov. 1, 2001).
114. Nieuwland, R., Rylander, R. & Karlsson, P. *NORIA: flexible automation in Fiber Bragg manufacturing* tech. rep. (working paper 10.13140/RG. 2.1. 2239.5925, 2016).
115. Pozo, J. “Sensors Everywhere!” The history of industry’s first fiber Bragg grating manufacturing system and subsequent sensors development. *PhotonicsViews* **16**, 18–20 (2019).
116. Atezhev, V. V., Vartapetov, S. K., Zhukov, A. N., Kurzanov, M. A. & Obidin, A. Z. Excimer laser with highly coherent radiation. *Quantum Electronics* **33**, 689–694 (Aug. 2003).
117. Idrisov, R. F. *et al.* Spectral Characteristics of Draw-Tower Step-Chirped Fiber Bragg Gratings. *Optics & Laser Technology* **80**, 112–115 (2016).
118. Carr, J., Saikkonen, S. & Williams, D. Refractive index measurements on single-mode fiber as functions of product parameters, tensile stress, and temperature. *Fiber & Integrated Optics* **9**, 393–396 (1990).

119. Iadicicco, A., Cusano, A., Campopiano, S., Cutolo, A. & Giordano, M. Thinned fiber Bragg gratings as refractive index sensors. *IEEE Sensors Journal* **5**, 1288–1295 (2005).
120. Snitzer, E. & Meltz, G. *Wide band multicore optical fiber* US Patent 4,300,816. Nov. 1981.
121. Kaiser, P. & Astle, H. W. Low-Loss Single-Material Fibers Made From Pure Fused Silica. *Bell System Technical Journal* **53**, 1021–1039 (1974).
122. Chillce, E., Cordeiro, C. M. d. B., Barbosa, L. & Cruz, C. B. Tellurite photonic crystal fiber made by a stack-and-draw technique. *Journal of Non-Crystalline Solids* **352**, 3423–3428 (2006).
123. Filipkowski, A. *et al.* Nanostructured gradient index microaxicons made by a modified stack and draw method. *Optics letters* **40**, 5200–5203 (2015).
124. Strutynski, C. *et al.* Stack-and-Draw Applied to the Engineering of Multi-Material Fibers with Non-Cylindrical Profiles. *Advanced Functional Materials*, 2011063 (2021).
125. Pniewski, J. *et al.* Diffractive optics development using a modified stack-and-draw technique. *Applied optics* **55**, 4939–4945 (2016).
126. Velmiskin, V. V., Egorova, O. N., Mishkin, V., Nishchev, K. & Semjonov, S. L. *Active material for fiber core made by powder-in-tube method: subsequent homogenization by means of stack-and-draw technique in Microstructured and Specialty Optical Fibres* **8426** (2012), 84260I.
127. Taghizadeh, M. R. *et al.* Nanostructured micro-optics based on a modified stack-and-draw fabrication technique. *Advanced Optical Technologies* **1**, 171–180 (2012).
128. Dunn, C. *et al.* Solid tellurite optical fiber based on stack-and-draw method for mid-infrared supercontinuum generation. *Fibers* **5**, 37 (2017).
129. Nguyen, H. T. *et al.* Optical characterization of single nanostructured gradient index vortex phase masks fabricated by the modified stack-and-draw technique. *Optics Communications* **463**, 125435 (2020).
130. Heyvaert, S., Ottevaere, H., Kujawa, I., Buczynski, R. & Thienpont, H. Stack-and-draw technique creates ultrasmall-diameter endoscopes. *Laser Focus World* **49**, 29–34 (2013).
131. Shengling, W. *et al.* *Stack-and-draw microstructured optical fiber with Ge<sub>28</sub>Sb<sub>12</sub>Se<sub>60</sub> chalcogenide glass in Photonic Networks and Devices* (2018), JTU5A–69.

132. Samir, A. & Batagelj, B. Stack-and-Draw Manufacture Process of a Seven-Core Optical Fiber for Fluorescence Measurements. en. *Fiber and Integrated Optics* **37**, 1–11. ISSN: 0146-8030, 1096-4681 (Jan. 2018).
133. Hasegawa, T. & Ohara, S. *Fabrication of bismuth-based photonic crystal fiber by stack and draw method* in *Optical Fiber Communication Conference (2009)*, OThK2.
134. Samir, A., Perpar, L. & Batagelj, B. *Fabrication of a single-mode seven-core optical fiber using the stack-and-draw procedure* in *2016 International Workshop on Fiber Optics in Access Network (FOAN) (2016)*, 1–4.
135. Wang, L., He, D., Chen, D. & Hu, L. Yb–Er doped composite fiber with silicate clad and phosphate core prepared by stack-and-draw method. *Optical and Quantum Electronics* **49**, 162 (2017).
136. Guang, Z., Qinling, Z., Lili, H., *et al.* A large core phosphate photonic crystal fiber made by a stack—and-draw technique. *Chinese Journal of Lasers*, 01 (2011).
137. Wang, L., He, D., Hu, L. & Chen, D. Heavily Yb-doped phosphate fiber with hexagonal inner cladding prepared by the stack-and-draw method. *Laser Physics* **25**, 035102 (2015).
138. Brilland, L. *et al.* Fabrication of complex structures of holey fibers in chalcogenide glass. *Optics Express* **14**, 1280–1285 (2006).
139. Nowosielski, J. *et al.* *Diffraction optics development with stack-and-draw technique* in *Micro-Optics 2012* **8428** (2012), 84281R.
140. Sasaki, Y., Hosaka, T., Takada, K. & Noda, J. 8 km-long polarisation-maintaining fibre with highly stable polarisation state. English. *Electronics Letters* **19**, 792–794(2). ISSN: 0013-5194 (19 Sept. 1983).
141. Noda, J., Okamoto, K. & Sasaki, Y. Polarization-maintaining fibers and their applications. *Journal of Lightwave Technology* **4**, 1071–1089 (1986).
142. Ishida, I *et al.* *Possibility of stack and draw process as fabrication technology for multi-core fiber* in *2013 Optical Fiber Communication Conference and Exposition and the National Fiber Optic Engineers Conference (OFC/NFOEC) (2013)*, 1–3.
143. Sakaguchi, J. *et al.* *109-Tb/s (7× 97× 172-Gb/s SDM/WDM/PDM) QPSK transmission through 16.8-km homogeneous multi-core fiber* in *2011 Optical Fiber Communication Conference and Exposition and the National Fiber Optic Engineers Conference (2011)*, 1–3.
144. Sakaguchi, J. *et al.* *Realizing a 36-core, 3-mode fiber with 108 spatial channels* in *2015 Optical Fiber Communications Conference and Exhibition (OFC) (2015)*, 1–3.

145. Kobayashi, T. *et al.* 1-Pb/s (32 SDM/46 WDM/768 Gb/s) C-band dense SDM transmission over 205.6-km of single-mode heterogeneous multi-core fiber using 96-Gbaud PDM-16QAM channels in *Optical Fiber Communication Conference* (2017), Th5B-1.
146. Puttnam, B. J. *et al.* 2.15 Pb/s transmission using a 22 core homogeneous single-mode multi-core fiber and wideband optical comb in *2015 European Conference on Optical Communication (ECOC)* (2015), 1-3.
147. Igarashi, K. *et al.* Super-Nyquist-WDM transmission over 7,326-km seven-core fiber with capacity-distance product of 1.03 Exabit/s· km. *Optics express* **22**, 1220-1228 (2014).
148. Igarashi, K. *et al.* 114 space-division-multiplexed transmission over 9.8-km weakly-coupled-6-mode uncoupled-19-core fibers in *Optical Fiber Communication Conference* (2015), Th5C-4.
149. Takara, H. *et al.* 1.01-Pb/s (12 SDM/222 WDM/456 Gb/s) crosstalk-managed transmission with 91.4-b/s/Hz aggregate spectral efficiency in *European Conference and Exhibition on Optical Communication* (2012), Th-3.
150. Ziolkowicz, A. *et al.* Hole-assisted multicore optical fiber for next generation telecom transmission systems. *Applied Physics Letters* **105**. ISSN: 00036951 (2014).
151. Matsui, T., Sagae, Y., Sakamoto, T. & Nakajima, K. Design and Applicability of Multi-Core Fibers With Standard Cladding Diameter. *Journal of Lightwave Technology* **38**, 6065-6070 (2020).
152. Zheng, W. *Automated Alignment and Splicing for Multicore Fibers* en. in *Optical Fiber Communication Conference/National Fiber Optic Engineers Conference 2013* (OSA, Anaheim, California, 2013), OM3I.4. ISBN: 978-1-55752-962-6.
153. Amma, Y., Takenaga, K., Matsuo, S. & Aikawa, K. Fusion splice techniques for multicore fibers. en. *Optical Fiber Technology* **35**, 72-79. ISSN: 10685200 (Feb. 2017).
154. B, A. J. *pat.* US 5317575 A (US) (1992).
155. Zheng, W. Automated fusion-splicing of polarization maintaining fibers. *Lightwave Technology, Journal of* **15**, 125-134 (Feb. 1997).
156. Zheng, W., Sugawara, H. & Malinsky, B. *Fourier Analysis Method for Asymmetric Polarization-Maintaining Fiber Alignment* en. in *National Fiber Optic Engineers Conference* (OSA, Los Angeles, California, 2012), JW2A.12. ISBN: 978-1-55752-935-0.

157. Zheng, W., Duke, D., Kubo, T. & Malinsky, B. Interrelation Profile Analysis Method for Alignment of Polarization-Maintaining Fiber. *Proceedings of Optical Fiber Communication, Collocated National Fiber Optic Engineers* (Mar. 2010).
158. Abe, Y., Shikama, K., Ono, H., Yanagi, S. & Takahashi, T. Fan-in/Fan-out Device Employing v-Groove Substrate for Multicore Fibre. *Electronics Letters* **51**, 1347–1348 (2015).
159. Cui, J. *et al.* Fan-out Device for Multicore Fiber Coupling Application Based on Capillary Bridge Self-Assembly Fabrication Method. *Optical Fiber Technology* **26**, 234–242 (2015).
160. Thomson, R. R. *et al.* Ultrafast Laser Inscription of a 121-Waveguide Fan-out for Astrophotonics. *Optics letters* **37**, 2331–2333 (2012).
161. Tottori, Y., Kobayashi, T. & Watanabe, M. Low Loss Optical Connection Module for Seven-Core Multicore Fiber and Seven Single-Mode Fibers. *IEEE Photonics Technology Letters* **24**, 1926–1928 (2012).
162. Idrisov, R., Baghdasaryan, T., Rothhardt, M., Geernaert, T. & Bartelt, H. Experimental Approach for Complex Optical Fiber Angular Orientation and Twist Measurement. *Advanced Photonics Research* **n/a**, 2100161.
163. Idrisov, R., Floris, I., Rothhardt, M. & Bartelt, H. Characterization and Calibration of Shape Sensors Based on Multicore Optical Fibre. en. *Opt. Fiber Technol.* **61**, 102319. ISSN: 10685200 (Jan. 2021).
164. Tan, F. *et al.* Torsion sensor based on inter-core mode coupling in seven-core fiber. *Opt. Express* **26**, 19835–19844 (Aug. 2018).
165. Khan, F., Barrera, D., Sales, S. & Misra, S. Curvature, twist and pose measurements using fiber Bragg gratings in multi-core fiber: A comparative study between helical and straight core fibers. *Sensors and Actuators A: Physical* **317**, 112442. ISSN: 0924-4247 (2021).
166. Zhang, H. *et al.* Directional torsion and temperature discrimination based on a multicore fiber with a helical structure. *Opt. Express* **26**, 544–551 (Jan. 2018).
167. Budinski, V. & Donlagic, D. Fiber-Optic Sensors for Measurements of Torsion, Twist and Rotation: A Review. *Sensors* **17**. ISSN: 1424-8220 (2017).
168. Zafeiropoulou, A., Masoudi, A., Cooper, L. & Brambilla, G. Flat multi-core fibre for twist elimination in distributed curvature sensing. *Optical Fiber Technology* **66**, 102663. ISSN: 1068-5200 (2021).
169. Egorova, O. N. *et al.* Multicore fiber with rectangular cross-section. *Opt. Lett.* **39**, 2168–2170 (Apr. 2014).

170. Herman, G. *Fundamentals of Computerized Tomography: Image Reconstruction from Projections* ISBN: 9781846287237 (Springer London, 2009).
171. Arkhipov, S. V. *et al.* Birefringent optical fibers axial positioning technique for fiber Bragg gratings writing. en. *Opt Quant Electron* **48**, 541. ISSN: 1572-817X (Nov. 2016).
172. Hitzenberger, C., Goetzinger, E., Sticker, M., Pircher, M. & Fercher, A. Measurement and imaging of birefringence and optic axis orientation by phase resolved polarization sensitive optical coherence tomography. en. *Opt. Express* **9**, 780. ISSN: 1094-4087 (Dec. 2001).
173. Iwaguchi, T., Funatomi, T., Aoto, T., Kubo, H. & Mukaigawa, Y. Optical tomography based on shortest-path model for diffuse surface object. en. *IPSJ T Comput Vis Appl* **10**, 15. ISSN: 1882-6695 (Dec. 2018).
174. Azevedo, S., Schneberk, D., Fitch, J. & Martz, H. Calculation of the rotational centers in computed tomography sinograms. *IEEE Trans. Nucl. Sci.* **37**, 1525–1540. ISSN: 00189499 (Aug. 1990).
175. Wahba, H. H. & Kreis, T. Characterization of graded index optical fibers by digital holographic interferometry. EN. *Appl. Opt., AO* **48**. Publisher: Optical Society of America, 1573–1582. ISSN: 2155-3165 (Mar. 2009).
176. Wahba, H. Reconstruction of 3D refractive index profiles of PM PANDA optical fiber using digital holographic method. en. *Optical Fiber Technology* **20**, 520–526. ISSN: 10685200 (Oct. 2014).
177. Prisiazhniuk, A. V., Sokolenko, B. V., Poletaev, D. A. & Shostka, N. V. Digital holographic testing of the optical fiber at welding area. en. *J. Phys.: Conf. Ser.* **1400**. Publisher: IOP Publishing, 066042. ISSN: 1742-6596 (Nov. 2019).
178. Colomb, T. *et al.* Polarization microscopy by use of digital holography: application to optical-fiber birefringence measurements. EN. *Appl. Opt., AO* **44**. Publisher: Optical Society of America, 4461–4469. ISSN: 2155-3165 (July 2005).
179. Wolf, E. Three-dimensional structure determination of semi-transparent objects from holographic data. en. *Optics Communications* **1**, 153–156. ISSN: 00304018 (Sept. 1969).
180. Zhang, H. *et al.* Directional torsion and temperature discrimination based on a multicore fiber with a helical structure. *Optics express* **26**. Publisher: Optical Society of America, 544–551 (2018).

181. Westbrook, P. S. *et al.* Integrated optical fiber shape sensor modules based on twisted multicore fiber grating arrays in *Optical Fibers and Sensors for Medical Diagnostics and Treatment Applications XIV* **8938** (International Society for Optics and Photonics, 2014), 89380H.
182. Westbrook, P. S. *et al.* Continuous Multicore Optical Fiber Grating Arrays for Distributed Sensing Applications. *J. Lightwave Technol.* **35**, 1248–1252. ISSN: 0733-8724, 1558-2213 (Mar. 2017).
183. Lindley, E. *et al.* Core-to-core uniformity improvement in multi-core fiber Bragg gratings, 91515F. ISSN: 1996756X (2014).
184. Lindley, E. *et al.* Demonstration of uniform multicore fiber Bragg gratings. *Optics Express* **22**, 31575–31581 (2014).
185. Jiang, Y. *et al.* Strain and high-temperature discrimination using a Type II fiber Bragg grating and a miniature fiber Fabry–Perot interferometer. *Applied optics* **55**, 6341–6345 (2016).
186. Chojetzki, C. *et al.* High-Reflectivity Draw-Tower Fiber Bragg Gratings—Arrays and Single Gratings of Type II. *Optical Engineering* **44**, 060503 (2005).
187. Grobncic, D., Mihailov, S. J., Walker, R. B. & Smelser, C. W. *Self-packaged Type II femtosecond IR laser induced fiber Bragg grating for temperature applications up to 1000 C in 21st International Conference on Optical Fiber Sensors* **7753** (2011), 77530J.
188. Grobncic, D., Hnatovsky, C. & Mihailov, S. J. Thermally stable type II FBGs written through polyimide coatings of silica-based optical fiber. *IEEE Photonics Technology Letters* **29**, 1780–1783 (2017).
189. Archambault, J. L., Reekie, L & Russell, P. S. J. 100% reflectivity Bragg reflectors produced in optical fibres by single excimer laser pulses. *Electronics Letters* **29**, 453–455 (1993).
190. Tosi, D. Review and Analysis of Peak Tracking Techniques for Fiber Bragg Grating Sensors. *Sensors* **17**, 2368 (2017).
191. Askins, C. G. *et al.* *Inscription of Fiber Bragg Gratings in Multicore Fiber in Bragg Gratings, Photosensitivity, and Poling in Glass Waveguides* (Optical Society of America, 2007), JWA39.
192. Atkins, R. M. Measurement of the ultraviolet absorption spectrum of optical fibers. *Opt. Lett.* **17**, 469–471 (Apr. 1992).



193. Williams, D. L., Davey, S. T., Kashyap, R., Armitage, J. R. & Ainslie, B. J. Ultraviolet absorption studies on photosensitive germanosilicate preforms and fibers. en. *Applied Physics Letters* **59**, 762–764. ISSN: 0003-6951, 1077-3118 (Aug. 1991).
194. Meltz, G. & Morey, W. W. Bragg grating formation and germanosilicate fiber photosensitivity in *International Workshop on Photoinduced Self-Organization Effects in Optical Fiber* (ed Ouellette, F.) **1516** (SPIE, 1991), 185–199.
195. Henken, K., Dankelman, J., Van Den Dobbelsteen, J., Cheng, L. & Van Der Heiden, M. Error Analysis of FBG-Based Shape Sensors for Medical Needle Tracking. *IEEE/ASME Transactions on Mechatronics* **19**, 1523–1531. ISSN: 1083-4435, 1941-014X (Oct. 2014).
196. Henken, K., Van Gerwen, D., Dankelman, J. & Van Den Dobbelsteen, J. Accuracy of Needle Position Measurements Using Fiber Bragg Gratings. *Minimally Invasive Therapy & Allied Technologies* **21**, 408–414. ISSN: 1364-5706, 1365-2931 (Nov. 2012).
197. K. Mandal, K., Parent, F., Martel, S., Kashyap, R. & Kadoury, S. Calibration of a Needle Tracking Device with Fiber Bragg Grating Sensors in. SPIE Medical Imaging (eds Webster, R. J. & Yaniv, Z. R.) (Orlando, Florida, United States, Mar. 18, 2015), 94150X.
198. Gribaev, A. I. *et al.* Laboratory Setup for Fiber Bragg Gratings Inscription Based on Talbot Interferometer. en. *Optical and Quantum Electronics* **48**, 540. ISSN: 0306-8919, 1572-817X (Dec. 2016).
199. Amanzadeh, M., Aminossadati, S. M., Kizil, M. S. & Rakić, A. D. Recent Developments in Fibre Optic Shape Sensing. en. *Measurement* **128**, 119–137. ISSN: 02632241 (Nov. 2018).
200. Floris, I., Calderón, P. A., Sales, S. & Adam, J. M. Effects of Core Position Uncertainty on Optical Shape Sensor Accuracy. en. *Measurement* **139**, 21–33. ISSN: 02632241 (June 2019).
201. Zheng, D., Madrigal, J., Chen, H., Barrera, D. & Sales, S. Multicore Fiber-Bragg-Grating-Based Directional Curvature Sensor Interrogated by a Broadband Source with a Sinusoidal Spectrum. en. *Opt. Lett.* **42**, 3710. ISSN: 0146-9592, 1539-4794 (Sept. 2017).
202. Liu, Z. *et al.* Strongly Coupled Multicore Fiber with FBGs for Multipoint and Multiparameter Sensing. en. *Optical Fiber Technology* **58**, 102315. ISSN: 10685200 (Sept. 2020).

203. Donko, A. *et al.* Point-by-Point Femtosecond Laser Micro-Processing of Independent Core-Specific Fiber Bragg Gratings in a Multi-Core Fiber. *Optics express* **26**, 2039–2044 (2018).
204. Amorebieta, J. *et al.* Compact Omnidirectional Multicore Fiber-based Vector Bending Sensor. en. *Sci Rep* **11**, 12. ISSN: 2045-2322 (Mar. 2021).
205. Gasulla, I., Barrera, D., Hervás, J. & Sales, S. Spatial Division Multiplexed Microwave Signal Processing by Selective Grating Inscription in Homogeneous Multicore Fibers. en. *Sci Rep* **7**, 41727. ISSN: 2045-2322 (Mar. 2017).
206. Wolf, A., Dostovalov, A., Bronnikov, K. & Babin, S. Arrays of Fiber Bragg Gratings Selectively Inscribed in Different Cores of 7-Core Spun Optical Fiber by IR Femtosecond Laser Pulses. en. *Optics Express* **27**, 13978. ISSN: 1094-4087 (May 2019).
207. Donko, A. *et al.* Femtosecond Inscription and Thermal Testing of Bragg Gratings in High Concentration (40 Mol%) Germanium-Doped Optical Fibre. en. *Opt. Express* **25**, 32879. ISSN: 1094-4087 (Dec. 2017).
208. Sakaguchi, S. & Todoroki, S.-i. Optical Properties of GeO<sub>2</sub> Glass and Optical Fibers. en. *Appl. Opt.* **36**, 6809. ISSN: 0003-6935, 1539-4522 (Sept. 1997).
209. Dianov, E. & Mashinsky, V. Germanium-Based Core Optical Fibers. en. *J. Lightwave Technol.* **23**, 3500–3508. ISSN: 0733-8724 (Nov. 2005).
210. Wang, C. C., Wang, M. H. & Wu, J. Heavily Germanium-Doped Silica Fiber With a Flat Normal Dispersion Profile. en. *IEEE Photonics J.* **7**, 1–10. ISSN: 1943-0655 (Apr. 2015).
211. Butov, O., Golant, K., Tomashuk, A., van Stralen, M. & Breuls, A. Refractive Index Dispersion of Doped Silica for Fiber Optics. en. *Optics Communications* **213**, 301–308. ISSN: 00304018 (Dec. 2002).
212. Wood, D. L. & Fleming, J. W. Computerized Refractive Index Measurements for Bulk Materials at UV, Visible, and IR Wavelengths. en. *Review of Scientific Instruments* **53**, 43–47. ISSN: 0034-6748, 1089-7623 (Jan. 1982).
213. Fleming, J. W. Dispersion in GeO<sub>2</sub>-SiO<sub>2</sub> Glasses. en. *Appl. Opt.* **23**, 4486. ISSN: 0003-6935, 1539-4522 (Dec. 1984).
214. Sunak, H. & Bastien, S. Refractive Index and Material Dispersion Interpolation of Doped Silica in the 0.6-1.8  $\mu$ m Wavelength Region. *IEEE Photonics Technology Letters* **1**, 142–145. ISSN: 1041-1135, 1941-0174 (June 1989).

215. Tokarev, A. V. *et al.* UV-Transparent Fluoropolymer Fiber Coating for the Inscription of Chirped Bragg Gratings Arrays. en. *Optics & Laser Technology* **89**, 173–178. ISSN: 00303992 (Mar. 2017).
216. Kim, J., Oh, K., Park, T., Kim, C. & Jeong, K. Suppression of Cladding-Mode Coupling Loss in Fiber Bragg Gratings by Independent Control of Refractive Index and Photosensitive Profiles in a Single-Mode Optical Fiber. en. *IEEE Photonics Technology Letters* **12**, 1504–1506. ISSN: 1041-1135, 1941-0174 (Nov. 2000).
217. Douay, M. *et al.* Densification Involved in the UV-Based Photosensitivity of Silica Glasses and Optical Fibers. en. *J. Lightwave Technol.* **15**, 1329–1342. ISSN: 07338724 (Aug./1997).
218. Dong, L., Pinkstone, J., Russell, P. S. J. & Payne, D. N. Ultraviolet Absorption in Modified Chemical Vapor Deposition Preforms. en. *J. Opt. Soc. Am. B* **11**, 2106. ISSN: 0740-3224, 1520-8540 (Oct. 1994).
219. Fokine, M. *Photosensitivity, Chemical Composition Gratings and Optical Fiber Based Components* English. PhD thesis (Royal Institute of Technology, Stockholm, 2002). ISBN: 9789172833975.
220. Bubnov, M. M. *et al.* Fabrication and Optical Properties of Fibers with an Al<sub>2</sub>O<sub>3</sub>-P<sub>2</sub>O<sub>5</sub>-SiO<sub>2</sub> Glass Core. en. *Inorg Mater* **45**, 444–449. ISSN: 0020-1685, 1608-3172 (Apr. 2009).
221. Unger, S., Schwuchow, A., Dellith, J. & Kirchhof, J. Optical Properties of Ytterbium/Aluminium Doped Silica Glasses. en. *Optical Materials Express* **10**, 907. ISSN: 2159-3930 (Apr. 2020).
222. Bubnov, M. M. *et al.* Optical Properties of Fibres with Aluminophosphosilicate Glass Cores. en. *Quantum Electron.* **39**, 857–862. ISSN: 1063-7818, 1468-4799 (Sept. 2009).



# Zusammenfassung

Ein auf Faser-Bragg-Gittern (FBGs) in Multicore-Fasern basierender Formsensor ist ein komplexes Gerät mit zahlreichen Faktoren, die für ein erfolgreiches Messsystem berücksichtigt werden müssen. In dieser Dissertation habe ich einige Aspekte von solchen faseroptischen Form- und Krümmungssensoren betrachtet.

Der erste Aspekt ist die Herstellung von Multicore-Fasern und FBGs. Es gibt bereit fortgeschrittene Methoden, die die Herstellung von Multicore-Fasern für die Formsensorik ermöglichen. Das Einschreiben von FBGs in solchen Multicore-Fasern unterscheidet sich erheblich von den herkömmlichen Verfahren zum Einschreiben in Einzelkernfasern. Ich habe dazu die Einschreibung von Gittern in Multicore-Fasern untersucht, einschließlich des Einschreibens während eines Faserziehprozesses. Dabei habe ich die Anisotropie der Fasern berücksichtigt und geeignete Beleuchtungsrichtungen für die FBG-Einschreibung untersucht. Es hat dabei herausgestellt, dass einige Beleuchtungswinkelbereiche die Ungleichmäßigkeit der Amplituden der Reflexionsspitzen in verschiedenen Kernen erhöhen. Der Fokussierungseffekt des Mantels kann zur Bildung von Typ II FBGs in bestimmten Kernen führen und sogar einen Kern zerstören. Daher müssen diese optischen Effekte der Faser beim Design von Mehrkernfaser und beim Einschreiben von FBGs solche Fasern berücksichtigt werden.

Der zweite Aspekt ist die Charakterisierung von optischen Fasern und die Kalibrierung von Formsensoren. Häufig weisen die bei der Formsensorik verwendeten Multicore-Fasern Unregelmäßigkeiten auf. Durch die Charakterisierung der Multicore-Faser lässt sich vermeiden, dass diese Unregelmäßigkeiten die Messqualität beeinträchtigen. Zu den Faktoren, die charakterisiert werden müssen, gehören: Kern-Mittelpunkt-Abstand und Dickenstabilität der Einzelkerne, Variation des photoelastischen Koeffizienten in verschiedenen Kernen und ein intrinsisches Twist. Für die Messung des intrinsischen Twists wurde eine Methode für komplexe optische Fasern entwickelt. Für eine genaue Bestimmung der Winkel-Orientierung von Multikernfasern wurde eine Technik entwickelt. Diese Methode ermöglicht eine automatische Bestimmung der Winkel-Orientierung. Solche automatischen Messverfahren sind hilfreich bei der Charakterisierung längerer Fasern und bei der genauen Bestimmung von Twist in komplexen Multikernfasern.

Der dritte Aspekt ist das Wellenlängen Multiplexing von FBGs in Multicore-Glasfasern. In dieser Dissertation werden zwei neuartige Multiplexing-Methoden vorgestellt. Die erste Methode zielt darauf ab, das Abfrageschema der Sensorfunktion zu vereinfachen und die Anwendbarkeit von Sensoren auf der Grundlage von Multicore-Fasern und FBGs zu erleichtern. Die vorgeschlagene Methode, die auf einem inversen Biegesensor-Konzept basiert, ermöglicht die Messung von Gitter-Reflektionen aus einer Multikernfaser ohne Verwendung eines Fanout-Geräts. Dies ist besonders vorteilhaft für einfache, kurze Sensoren, wie z. B. Schwingungssensoren und Neigungsmesser. Die zweite Methode ermöglicht die Erweiterung der Messlänge eines Fasersensorsystems. Dazu wird eine Sensorfaser aus einzelnen Abschnitten gleichartiger Fasern zusammengesetzt, wobei die einzelnen Teile gegeneinander verdreht sind. Die Multikernfaser selbst enthält sowohl nicht-photosensitive als auch photosensitive Kerne. In die photosensitiven Kerne können die Fasergitter als Sensorelemente, eingeschrieben werden, während in den nicht-photosensitiven Kernen nur ein Signaltransport stattfindet. In dem vorgestellten Design wird dabei beispielhaft eine zweifache Vergrößerung der Sensorlänge gezeigt.

Die Arbeit schließt ab mit einem Ausblick.

# Summary

A shape sensor based on fiber Bragg gratings (FBGs) in multicore fibers is a complex device with multiple factors which have to be accounted for a successful measurement system.

In this dissertation, I considered several aspects of such shape and curvature sensors.

The first aspect is the fabrication of multicore fibers and FBGs. There are advanced methods allowing for fabricating of multicore fibers for shape sensing. FBGs inscription in such multicore fibers has considerable differences compared to a conventional inscription in single core fibers. I studied the inscription of gratings in multicore fibers, including the inscription during the fiber drawing process. For that, I considered the anisotropy of the fibers and considered the illumination orientation for the FBG inscription. It was found that some illumination angle ranges increase the non-uniformity of the reflection peaks amplitudes in different cores. The focusing effect of the cladding might lead to the formation of type II FBGs in specific cores and even destroy a core. Hence, the optical effects of the fiber have to be considered while designing complex fibers and inscribing FBGs in such a multicore fiber.

The second aspect is the characterization of optical fibers and the calibration of shape sensors. Often, multicore fibers used in shape sensing have irregularities and characterization of the multicore fiber allows for correction of such irregularities in the measurement. Among the factors which have to be characterized are: core-to-center distance and thickness stability, photo-elastic coefficient variation in different cores, and intrinsic twist. For the intrinsic twist measurement, there was a method developed for use with multicore optical fibers. For a precise measurement of an angular orientation, a method based on associating the rotational scattering patterns with a random fiber orientation was developed. This method allows for an automatic recognition of a rotational position. Such automatic measurement can help to characterize long fiber pieces and to measure the exact twist of complex optical fibers.

The third aspect is multiplexing in multicore optical fibers with FBGs. In this dissertation, there are two novel multiplexing methods presented. The first method is directed to simplifying the interrogation scheme and increasing accessibility of

sensors based on multicore fibers and FBGs. The suggested method based on inverse bend sensing allows for interrogating the gratings across the fiber without use of a fanout device. This is especially beneficial for simple short sensors, such as vibration sensors and inclinometers. The second method allows for extending the sensing length through including non-photosensitive and photosensitive cores in a multicore fiber. When this fiber is prepared as described in Chapter 7, the fiber connects to a series composed of a few non-photosensitive cores delivering the light to a core with inscribed FBGs. With a few photosensitive cores and a corresponding number of non-photosensitive cores, this multiplexing principle was enabled for shape sensing. In the demonstrated design, there was a two-fold increase in a sensor length achieved.

Finally, the dissertation is concluded, and an outlook for future work is given.



# Curriculum vitae

Last name: Idrisov  
 First name: Ravil  
 Date of birth: 19.08.1992  
 Place of birth: Naberezhnye Chelny, Russia

|                   |  |
|-------------------|--|
| 09.1999 - 05.2010 | Gymnasium 19 (Naberezhnye Chelny)  |
| 09.2005 - 05.2010 | Boarding School 79 (Naberezhnye Chelny)  |
| 09.2010 - 08.2014 | ITMO University, B.Sc. in Telecommunications (Saint-Petersburg, Russia), thesis on "Spectral characteristics of draw-tower step-chirped fiber Bragg gratings"  |
| 09.2014 - 08.2016 | ITMO University, M.Sc. in Optical systems and communication networks (Saint-Petersburg, Russia), thesis on "Laboratory setup for fiber Bragg gratings inscription based on KrF excimer laser system" |
| 04.2017           | Accepted as a doctoral student at the Friedrich Schiller University of Jena, Faculty of Physics and Astronomy  |
| 04.2017 - 08.2020 | PhD studies within Marie Skłodowska-Curie Actions programme, Early Stage Researcher (Leibniz-IPHT, Jena, Germany)  |
| 04.2017 - 12.2021 | Doctoral Researcher (Leibniz-IPHT, Jena, Germany)  |

Jena, den 10.11.2021

Ravil Idrisov



# List of publications

## List of scientific publications as a first author:

1. Idrisov, R., Lorenz, A., Rothhardt, M., & Bartelt, H. (2022). Composed Multi-core Fiber Structure for Extended Sensor Multiplexing with Fiber Bragg Gratings. *Sensors*, 22(10), 3837.
2. Idrisov, R., Baghdasaryan, T., Rothhardt, M., Geernaert, T., & Bartelt, H. (2022). Experimental Approach for Complex Optical Fiber Angular Orientation and Twist Measurement. *Advanced Photonics Research*, 3(1), 2100161.
3. Idrisov, R., Floris, I., Rothhardt, M., & Bartelt, H. (2021). Characterization and calibration of shape sensors based on multicore optical fibre. *Optical Fiber Technology*, 61, 102319.
4. Idrisov, R. F., Varzhel, S. V., Kulikov, A. V., Meshkovskiy, I. K., Rothhardt, M., Becker, M., ... & Bartelt, H. (2016). Spectral characteristics of draw-tower step-chirped fiber Bragg gratings. *Optics & Laser Technology*, 80, 112-115.
5. Idrisov, R. F., Gribaev, A. I., Stam, A. M., Varzhel, S. V., Slozhenikina Yu, I., & Konnov, K. A. (2017). Recording superpositions of fiber Bragg gratings using the Talbot interferometer. *Opticheskii Zhurnal*, 84(10), 56-60.
6. Idrisov, R. F., Gribaev, A. I., Stam, A. M., Slozhenikina, Y. I., & Konnov, K. A. (2017). Inscription of superimposed fiber Bragg gratings using a Talbot interferometer. *Journal of Optical Technology*, 84(10), 694-697.

## Patents:

Idrisov, R., Rothardt, M., Becker, M., and Bartelt, H., "Multikernfaser mit Multikern-Faserkomponenten sowie Verfahren zu ihrer Herstellung," DE102019132569B3, Feb. 18, 2021 Accessed: Apr. 07, 2021. [Online].

## Conference proceedings:

1. Idrisov, R., Rothhardt, M., & Bartelt, H. (2019, October). In-plane wavelength multiplexing of fibre Bragg gratings in a multicore optical fibre. In Fourth International Conference on Applications of Optics and Photonics (Vol. 11207, p. 112072O). International Society for Optics and Photonics.
2. Idrisov, R., Becker, M., Rothhardt, M., Bierlich, J., & Bartelt, H. (2018, September). Optimisation of fibre Bragg gratings inscription in multicore fibres. In Optical Fiber Sensors (p. WF64). Optical Society of America.

**Co-authorship:**

1. Novikova Victoria, A., Varzhel Sergey, V., Andrey, A. D., Zalesskaya Yulia, K., & Idrisov Ravil, F. (2018). Spectral characteristics study of phase-shifted fiber Bragg gratings under pressure applied perpendicular to fiber axis. *Journal Scientific and Technical Of Information Technologies, Mechanics and Optics*, 117(5), 751-757.
2. Gribaev, A. I., Pavlishin, I. V., Stam, A. M., Idrisov, R. F., Varzhel, S. V., & Konnov, K. A. (2016). Laboratory setup for fiber Bragg gratings inscription based on Talbot interferometer. *Optical and Quantum Electronics*, 48(12), 1-7.
3. Stam, A. M., Idrisov, R. F., Gribaev, A. I., Varzhel, S. V., Konnov, K. A., & Slozhenikina Yu, I. (2017). Fiber Bragg gratings inscription using Talbot interferometer and KrF excimer laser system. *Journal of Instrument Engineering*, 60(5), 466-473.

# Ehrenwörtliche Erklärung

Ich, Ravil IDRISOV, erkläre hiermit ehrenwörtlich, dass ich die vorliegende Arbeit selbständig, ohne unzulässige Hilfe Dritter und ohne Benutzung anderer als der angegebenen Hilfsmittel und Literatur angefertigt habe. Die aus anderen Quellen direkt oder indirekt übernommenen Daten und Konzepte sind unter Angabe der Quelle gekennzeichnet. Bei der Auswahl und Auswertung folgenden Materials haben mir die nachstehend aufgeführten Personen in der jeweils beschriebenen Weise entgeltlich/unentgeltlich geholfen:

- Ray-Tracing-Simulationen für Multicore-Faserbeleuchtungen wurden von Dr. Martin Becker durchgeführt.

Weitere Personen waren an der inhaltlich-materiellen Erstellung der vorliegenden Arbeit nicht beteiligt. Insbesondere habe ich hierfür nicht die entgeltliche Hilfe von Vermittlungs- bzw. Beratungsdiensten (Promotionsberater oder andere Personen) in Anspruch genommen. Niemand hat von mir unmittelbar oder mittelbar geldwerte Leistungen für Arbeiten erhalten, die im Zusammenhang mit dem Inhalt der vorgelegten Dissertation stehen. Die Arbeit wurde bisher weder im In- noch im Ausland in gleicher oder ähnlicher Form einer anderen Prüfungsbehörde vorgelegt. Die geltende Promotionsordnung der Physikalisch-Astronomischen Fakultät ist mir bekannt. Ich versichere ehrenwörtlich, dass ich nach bestem Wissen die reine Wahrheit gesagt und nichts verschwiegen habe.

Jena, den 10.11.2021

Ravil Idrisov

---